

# Assembly of Multinary Colloidal Systems in a Centrifugal Field

Dissertation submitted for the doctoral degree of  
Natural Sciences  
(Dr. rer. nat)

Presented by

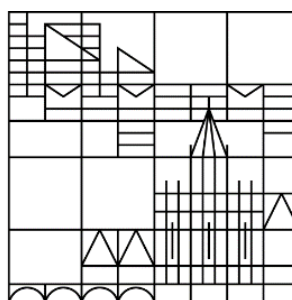
**Mengdi Chen**

at the

Faculty of Mathematics and Natural Sciences

Department of Chemistry

Universität  
Konstanz



Date of the oral exam: May 11, 2017

First referee: Prof. Dr. Sebastian Polarz

Second referee: Prof. Dr. Helmut Cölfen





# Acknowledgements

The present work was made in the period from April 2013 to September 2016 in the working groups of Prof. Dr. Sebastian Polarz and Prof. Dr. Helmut Cölfen at Department of Chemistry, University of Konstanz.

I would like to thank Prof. Polarz and Prof. Cölfen for introducing me to such an interesting research topic. I say interesting, I mean interesting. Science was brought to China in nineteenth century and named Mr. Sai by Chinese people. When working with such an “exotic” Mr. Sai, I could feel some old Chinese philosophy deep in my blood. With the great supervision and support from both Prof. Polarz and Prof. Cölfen, I finally found science my true love and set up my mind to continue scientific research as my life’s work. China scholarship council should be highly acknowledged for the financial support. Also I would like to thank Prof. Hejun Li from Northwestern Polytechnical University who has supported me to be involved in this scholarship program.

Life in Konstanz cannot be so great without my two wonderful working groups. Special thanks to Dr. Michael Krumm, Dr. Julia Gehring, Dr. Marius Schmid, Dr. Carlos Lizdara, Dr. Stefan Dilger for helping me to start my work; Melanie Gerigk for nice girls’ talks which comforted me so much in our no-window office; Martin Wessig and Alexander Klaiber for IT support; Martin Luka, Tom Kollek, Andreas Schachtschneider, Yvonne Binder, Stefanie Hermann, Markus Voggenreiter, Nele Klinkenberg, Adrian Donner, Dr. James Odendal, Bastian Trepka, Sebastian Sutter for the fruitful discussion; Kay Hagedorn for the nice project cooperation; Dirk Haffke and Rose Rosenberg for solving all AUC problems; Benedikt Häusele for keeping an organized lab, AF4 analysis and tough translation work; Dr. Shengtong Sun, Dr. Bingqiang Lu, Yu-Chieh Huang, Dr. Maria Helminger, Dr. Tuan Anh Pham, Holger Reiner, Masoud Farhadi Khouzani, Jennifer Knaus, Johanna Scheck, Cornelia Schneider, Peck-Yin Sow for the nice time we have shared.

Through the cooperation with AG Maret, I got to know two nice partners from Physics department. I would like to thank Prof. Georg Maret, Lukas Schertel, as well as Dr. Geoffroy Aubry for the great cooperation.

I have also received a lot of support from people outside the working groups. I am thankful for the support from Matthias Hagner in Nanolab, the assistance from welcome center, the help from students like Danja Fischli, Julian Steinbrecher, Wenhan Zhang.

I am grateful for my family and friends. Love from my mother and my husband have gone across the distance to cheer me up. I thank the oversea phone talks with my best friends Yujie, Long, Li and wish our friendships last another ten years and forever.



# Table of contents

<b>1. INTRODUCTION</b> .....	<b>1</b>
<b>2. THEORETICAL BACKGROUND</b> .....	<b>5</b>
<b>2.1 STAND OF THE KNOWLEDGE</b> .....	<b>5</b>
<b>2.1.1 Colloids</b> .....	<b>5</b>
<b>2.1.2 Colloidal forces</b> .....	<b>6</b>
<b>2.1.3 Centrifugal field-directed colloidal assembly</b> .....	<b>10</b>
<b>2.1.4 General analytical ultracentrifugation</b> .....	<b>11</b>
<b>2.1.5 Porous materials</b> .....	<b>18</b>
<b>2.2 RELEVANT SYNTHESIS AND ANALYTICAL TECHNIQUES</b> .....	<b>19</b>
<b>2.2.1 Dynamic light scattering</b> .....	<b>19</b>
<b>2.2.2 Analytical ultracentrifugation --- particle size distributions</b> .....	<b>22</b>
<b>2.2.3 Scanning electron microscopy (SEM)</b> .....	<b>23</b>
<b>3. SCOPE</b> .....	<b>25</b>
<b>4. RESULTS AND DISCUSSION</b> .....	<b>27</b>
<b>4.1 ASSEMBLY OF MONODISPERSE COLLOIDAL SYSTEM IN THE PRESENCE OF EXTRA ELECTROLYTES</b> .....	<b>27</b>
<b>4.1.1 Conventional methods to characterize the colloidal stability</b> .....	<b>28</b>
<b>4.1.2 Determining size of colloidal particles to detect the nanoparticle aggregation</b> .....	<b>31</b>
<b>4.1.3 Free-standing photonic glasses prepared via co-assembly method</b> .....	<b>41</b>
<b>4.2 ASSEMBLY OF BINARY COLLOIDAL SYSTEM BETWEEN CHAOS AND ORDER</b> .....	<b>44</b>
<b>4.2.1 Characterization of binary colloidal system in analytical ultracentrifugation (AUC): Concentration dependency of sedimentation behavior</b> .....	<b>46</b>
<b>4.2.2 Gaining control over binary colloidal system in preparative centrifuge</b> .....	<b>48</b>
<b>4.2.3 The emergence of ordered binary structures</b> .....	<b>51</b>
<b>4.2.4 The mechanism leading to various structures</b> .....	<b>57</b>
<b>4.3 FUNCTIONAL POROUS CARBON MONOLITHS: FROM MULTINARY COLLOIDAL ASSEMBLY TO A DEFINED GRADIENT POROSITY</b> .....	<b>63</b>
<b>4.3.1 Approaching gradient porous carbon materials via the conventional templating route</b> .....	<b>64</b>
<b>4.3.2 Developing new synthesis route for crack-free gradient porous carbon materials</b> .....	<b>67</b>
<b>4.3.3 The role of the pore size directionality in a battery application</b> .....	<b>76</b>

<b>5. SUMMARY AND OUTLOOK / ZUSAMMENFASSUNG UND AUSBLICK.....</b>	<b>82</b>
<b>6. EXPERIMENTAL PART .....</b>	<b>87</b>
<b>7. ABBREVIATION .....</b>	<b>94</b>
<b>8. REFERENCES .....</b>	<b>96</b>



# 1. Introduction

Colloidal systems are ubiquitously found in both natural environment and industrial process, e.g. blood, toothpaste and paint. The colloidal systems consisting of particles uniform in size and shape from *ca.* 10 nm to 1000 nm have been considered and used as a model system to explore the atomic world since the work of Albert Einstein<sup>2</sup> and Jean Baptiste Perrin.<sup>3</sup> Over the years, colloidal systems have been of tremendous interest in relation to a wide range of scientific questions,<sup>4</sup> including phase transitions,<sup>5</sup> fundamental problems of kinetics of crystallization,<sup>6-7</sup> and the physics of nucleation and growth.<sup>8</sup>

In recent two decades along with the popularization of nanotechnology, the colloidal systems have also become a good platform for the constructions of complex three dimensional objects at scales from the molecular to the macroscopic via the assembly route.<sup>9</sup> Contrary to intuition, to arbitrarily obtain high degrees of disorder structures from monodisperse building blocks is not an easy task. When the solid phase in a colloidal suspension is built up of uniform spherical nanoparticles, e.g. polymeric latex spheres, the random media known as photonic glasses can be formed under proper conditions. The random structures can strongly affect light transport and exhibit interesting physical phenomena like random lasing and light localization.<sup>10-</sup>  
<sup>11</sup> Colloidal crystals with thermodynamically preferred face-centered-cubic lattice serve as the other extreme system compared to colloidal glasses. The optical properties of such regular and periodic arrays have been studied in detail, when people were looking for promising crystal structures displaying complete photonic band gaps. As an extension of the colloidal crystals, nanoporous materials can be prepared via the templating concept.<sup>12</sup> The so called inverse opal structures as a replica of colloidal crystals have attracted a lot of attention due to their potential applications not only in photonic devices, but also in different functional materials including sensors, batteries, supercapacitors, fuel cells, etc.<sup>13</sup>

To form organized structures from colloidal systems via the assembly route, key factors should be taken into account from two aspects. One important aspect is about the colloidal building block itself. At thermodynamic equilibrium, the colloidal building blocks are brought into a structure which corresponds to the minimum of an appropriate thermodynamic potential. The whole colloidal system tends to the minimum of the Gibbs or Helmholtz free energy. Therefore, to assure that formation of ordered colloidal arrays in a system takes place under a thermodynamically favorable condition, the colloidal monodispersity has to be emphasized. Monodisperse in this context refers to the uniformity of size, shape and interaction between

colloidal particles. After several years of intense research, there are now many available synthetic methods to prepare nanoscopic spheres,<sup>14</sup> rods,<sup>15</sup> ellipsoids,<sup>16</sup> plates,<sup>17</sup> core/shell particles<sup>18</sup> with very good monodispersity. And the composition of the particles also ranges from polymers<sup>19</sup> to oxides<sup>20</sup>, semiconductors<sup>21</sup> and metals<sup>22</sup>.

Besides the properties of every single particle, the length scale and magnitudes of the interparticle forces act as another crucial aspect in the formation of assembled structures. The length scale of the attractive force interactions relative to the particle size determines the competition between the formation of equilibrium structures and dynamical arrest. It is desirable to use interactions that are of long range compared to the size of the assembling particles to build ordered structures. Large particles such as micrometer-scale colloids via short-range attractions (e.g. Van der Waals forces) are more susceptible to glassy state formation. Therefore, the crystallization of sub micrometer or micrometer colloids are mostly realized by using long-range interactions like the electrostatic and depletion forces. Electrostatic forces can be either attractive or repulsive. The magnitudes and length scale are able to be tuned in a controlled way by selecting solvent with different dielectric constants, or changing the size and valence of the colloids.

Other than mono component colloidal systems, the assembly of multinary (multicomponent distinct in size and/or composition) colloidal systems into superstructures became possible<sup>23</sup> owing to the flexible tuning of the particles' properties and interactions. In particular, binary systems have attracted rapidly growing interest as they raise the possibility of new properties that could arise from combining the properties of individual components. Similar to mono component colloidal systems, both the random mixtures and ordered arrays assembled from the binary colloidal systems can bring exciting phenomena and properties. For example, in a random mixed system designed from small and large quantum dots, electronic energy transfer from the small to the large dots is observed as luminescence quenching of the small dots and luminescence enhancement of the large dots.<sup>24</sup> Regarding the ordered binary arrays, many theoretical studies have been focused on predicting the probability of formation of various ordered binary structures and comparison of their stability.<sup>25-27</sup> However, it is difficult to explain the formation of many experimentally observed structures which have the packing fraction density below 0.74 (cubic close-packed or hexagonal close-packed) in terms of only entropy driven crystallization. Some models have been proposed by emphasizing the importance of Coulomb, van der Waals, charge-dipole, and dipole-dipole interactions for assembly of complex binary superstructures.<sup>28</sup> More contributions to further understand the diversity of ordered binary arrays are in great demand.

Despite the enormous progress made in tuning the sizes, shapes, compositions, or surface chemistry of colloidal nanoparticles over the last two decades, efficient and robust ways of assembling mono, binary or even multinary nanocomponents nowadays remain the bottleneck to deliver truly revolutionary solutions for medical diagnostics, drug delivery, sensors, electronic devices, and other new materials with unique properties.<sup>29</sup> Thus, the external forces that act to bring particles together play an important role in colloidal assembly. Different external driving forces, like gravitational force, capillary force, electromagnetic forces can be used to direct colloidal particles assembly process. When the applied field can be precisely designed and controlled, it exists as a physical template and guides the assembly toward structures characterized by new energy minima.<sup>30</sup> The involvement of external forces would lead to a further enrichment of phenomena under equilibrium and also under non-equilibrium situations. For example, highly ordered lamellar and cylindrical domains of diblock copolymers have been achieved under an applied electric field.<sup>31</sup> With the static magnetic field, magnetic nanoparticles assembled into well-ordered chains via dipole-dipole interactions.<sup>32</sup>

Sedimentation of colloidal particles in a gravitational field combined with drying of suspension from above is an easy and straightforward way to obtain artificial nanostructures based on colloidal crystals. In addition, the sedimentation process can be speeded up by applying centrifugal field. As previously mentioned, the monodispersity is a crucial factor in colloidal assembly. With centrifugation, isolated and purified building blocks can be obtained. However, the use of centrifugation method is very limited in colloidal assembly, compared to the use of electric field or magnetic field. On one hand, the fundamental study of colloidal systems requires precise control over the parameters which could influence the colloidal assembly process. On the other hand, it is very important to integrate the nanomaterials into devices for most applications. Both of the above two points are very difficult to address in the centrifugal field.

Analytical ultracentrifugation (AUC) was invented by Svedberg almost one century ago. AUC uses centrifugal force to fractionate particles with different molar mass, particle size, structure or density without any stationary phase requirement. Analytical properties of AUC come from its optical detectors. Interaction between particles and light which passes through the AUC cell is the basic principle of optical detection. Svedberg won the Nobel Prize in 1926 for his work on disperse systems including the work with AUC. The first important contribution made by AUC was showing that macromolecules really exist. Since then AUC has become an important method to determine the molecular weight, hydrodynamic radius and thermodynamic properties of a protein or other macromolecule.<sup>1</sup>

As mentioned above, some factors limit the use of a centrifugal field in one component colloidal assembly although it is straightforward and practical, not to mention binary or even multinary colloidal systems. Even for the simplest multinary colloidal systems composed of spherical nanoparticles with different sizes, there are many parameters which could influence the assembled structures like the ratio of the sphere diameters, the number ratio, and the centrifugation speed, etc., it is very important to perform the studies with support from an analytical method. For such studies, AUC is very well suited, since it combines an extremely high resolution up to Angstrom resolved particle size distributions<sup>33</sup> with high statistical accuracy because every particle is detected. In addition, AUC is able to resolve extremely broad particle size distributions over the entire colloidal range.<sup>34-35</sup> Also AUC can cope with highly concentrated systems as needed for colloidal crystal formation.<sup>36-37</sup> Therefore, if the sedimentation behaviour of colloidal systems can be characterized in AUC and transferred to a common preparative centrifuge, the effect of centrifugal field on colloidal assembly could then be systematically investigated. This is the primary concept on which the whole thesis is based.

## 2. Theoretical background

In this part, the basic knowledge behind this work, namely colloids, colloidal forces, the role of external forces in assembly, analytical centrifugation and porous materials will be introduced. Secondly, the most relevant analytical techniques which have been used in this work will be elaborated. Although it is not possible to cover all of the above mentioned topics in detail, further information can be found in several books, review articles and papers cited in this chapter.

### 2.1 Stand of the knowledge

#### 2.1.1 Colloids

The word “colloid” which means “glue” in Greek was first used by Thomas Graham in 1861 for glue-like substances (arabic gum, gelatine) that could be separated from water by diffusing the mixture through a membrane.<sup>38</sup> Nowadays, the term “colloid” refers to a solution that has particles with size between 1 nm and 1000 nm, yet are still able to remain evenly distributed throughout the solution. This kind of solution is also known as colloidal dispersion because the substances remain dispersed and do not settle to the bottom of the container. The lower limit of the colloid size is primarily set to make sure that the dispersion medium can be treated as a homogeneous background. When the particles become too small, each molecule in the medium should be treated individually to well predict the behavior of the whole system. The upper limit of the colloid size is related to the Brownian motion which was first observed when the Scottish botanist Robert Brown studied the plant pollination and fertilization. Albert Einstein gave the theoretical explanation for the observed motion which was experimentally verified by Jean Baptiste Perrin. Colloidal particles with size up to a few micrometer experience Brownian motion, while larger objects move only according to the mechanics’ laws and should be classified as granular matter.

In everyday life, milk, mayonnaise, fog, smoke and clay are all found to be colloidal systems. Due to the important role of colloidal particles in understanding the flow behavior, modelling the atomic world, as well as building 3D nanostructures, intensive research on the synthetic methods has been done and many synthetic nanoscopic colloidal particles are nowadays available. As this work being a pioneer work of investigating multinary colloidal systems in centrifugal field, relatively simple systems consisting of polystyrene latex spheres with different sizes were chosen to build up mono, binary and ternary colloidal systems.

### 2.1.2 Colloidal forces

Various interparticle forces like van der Waals, electrostatic, magnetic can be used in nanoscale assembly. Each type of interactions can be tuned by physical and chemical modification of the particle or solvent. To assemble nanoscopic components into larger structures and materials depends crucially on the understanding of the interparticle interactions. Bartosz A. Grzybowski and his coworkers<sup>29</sup> presented a nice review article about the use of nanoscale forces in nanoparticle assembly.

The interaction energy between colloidal particles is based on the interaction between their atomic or molecular constituents. There are three types of interaction, i.e. orientation interactions, induced dipolar interactions and dispersion interactions, which all scale with  $1/r^6$ . The sum of these different interactions is called the van der Waals interaction energy  $U_{vdW}$  (Equation 2 - 1).

$$U_{vdW} = -\frac{1}{r^6} (C_{orient} + C_{induced} + C_{dispersion}) \quad \text{Equation 2 - 1}$$

where  $C_{orient}$ ,  $C_{induced}$  and  $C_{dispersion}$  are parameters characterizing the interacting species and the surrounding medium.

Van der Waals forces do not arise from covalent bonds or ionic bonds. Instead, the electromagnetic fluctuations due to the incessant movements of positive and negative charges within all types of dipoles are the origins of Van der Waals force.<sup>29</sup> Van der Waals forces are all short-range forces so that only interactions between the nearest particles need to be considered.

The magnitude of van der Waals forces between the colloidal components varies from a few to hundreds times of  $kT$ . They can be tuned by using stabilizer or proper solvents. There are also theoretical approaches which could be used for designing the interparticle potentials. Despite of some shortcomings, the Hamaker integral approximation (Equation 2 - 2) has been widely used due to its simplicity for the case of two spherical particles.

$$U_{vdW}(r) = \frac{A}{3} \left[ \frac{a_1 a_2}{r^2 - (a_1 + a_2)^2} + \frac{a_1 a_2}{r^2 - (a_1 - a_2)^2} + \frac{1}{2} \ln \left( \frac{r^2 - (a_1 + a_2)^2}{r^2 - (a_1 - a_2)^2} \right) \right] \quad \text{Equation 2 - 2}$$

In Equation 2 - 2,  $a_1$  and  $a_2$  are the radii of the two particles,  $r$  is the distance between particle centers.  $A$  is the Hamaker constant with  $A = \frac{C_{vdW}\pi^2}{v_1 v_2}$  where  $v_i$  is the molar volume of material  $i$ ,  $C_{vdW} = C_{orient} + C_{induced} + C_{dispersion}$ .

While the van der Waals potential between colloidal particles consisting of the same material being attractive, the repulsive interactions including steric and electrostatic repulsion play an important role in preventing colloidal particle aggregation. The magnitude and length scale of electrostatic interactions can be influenced by the dispersing medium of the colloidal particles.

In an ionic solution, colloidal particle surfaces obtain net charge due to the adsorption of ions. The electrostatic potential decays exponentially at an increasing distance away from the charged bodies in solution (see Figure 2. 1). Debye length ( $\kappa^{-1}$ ) is the length scale characterizing this exponential decay. Within  $\kappa^{-1}$ , there are two parallel layers of charge surrounding the object which are known as electric double layers. The first layer (Stern layer) comprises ions adsorbed onto the object due to chemical interactions. The second layer (diffusing layer) composed of ions is attracted to the surface charge via the coulomb force electrically screens the first layer. When the electrical double layers of two colloids overlap, a repulsive interaction occurs.

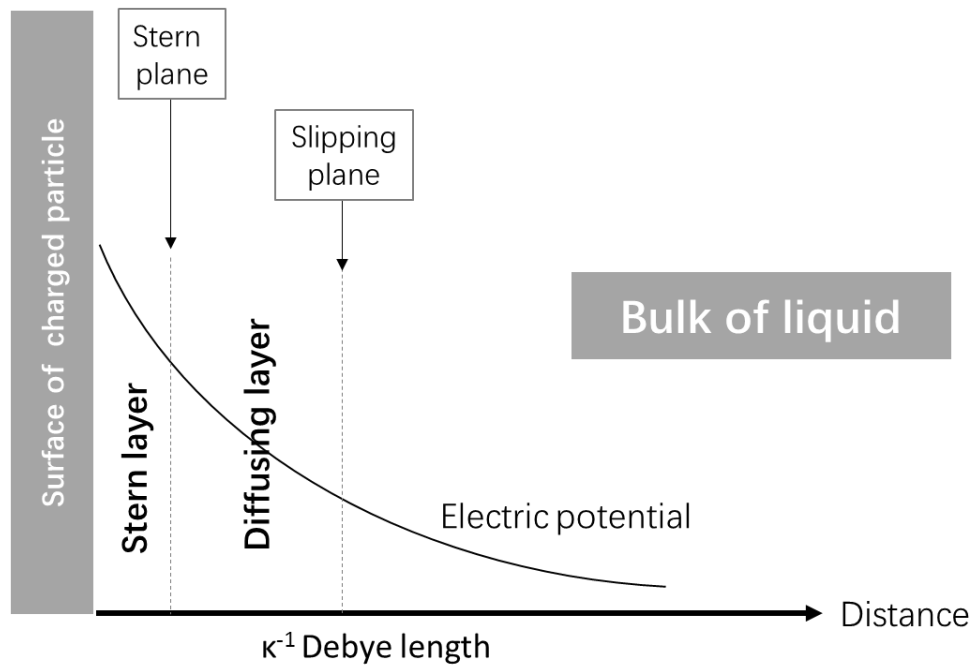


**Figure 2. 1 Illustration of the electric double layer model**

Poisson-Boltzmann theory is commonly used to resolve the electrostatic potential  $\varphi$  (Equation 2 - 3) in the presence of additional electrolyte.

$$\nabla^2 \varphi = \frac{2ec_s}{\epsilon_0 \epsilon} \sinh\left(\frac{e\varphi}{kT}\right) \quad \text{Equation 2 - 3}$$

where  $e$  is the elemental charge,  $c_s$  is the bulk salt concentration,  $\epsilon$  is the relative permittivity of the solution,  $\epsilon_0$  is the permittivity of vacuum,  $k$  is the Boltzmann constant,  $T$  is the temperature in Kelvin.

Furthermore, the electrostatic potential can be characterized by a single parameter  $\kappa^2$  in Equation 2 - 4. Here,  $\kappa^{-1} = (2e^2c_s/\epsilon_0\epsilon kT)^{-1/2}$ ,  $\psi = e\phi/kT$ .

$$\nabla^2\psi = \left(\frac{2e^2c_s}{\epsilon\epsilon_0kT}\right)\sinh\psi = \kappa^2\sinh\psi \quad \text{Equation 2 - 4}$$

The so called DLVO theory has been applied to approximate the colloidal stability. This theory is named after Derjaguin, Landau, Verwey, and Overbeek<sup>39</sup> and based on the assumption that the electrostatic and the van der Waals potential between the particles are additive. The basic features of DLVO theory are shown in Figure 2. 2. At very small distance, the van der Waals potential will always dominate, since  $W \propto -1/D^n$  ( $W$  and  $D$  represent the van der Waals potential and the distance between two charged surfaces respectively), whereas the electrostatic potential rises much more slowly when the distance is approaching 0. But if the repulsion is strong enough, at some distance the total interaction shows a very high barrier which makes the particles very difficult to come close to the van der Waals attraction region (the primary minimum). In certain concentrated electrolyte suspensions, a significant secondary minimum may occur. The colloidal particles would either stay at the secondary minimum or remain dispersed.

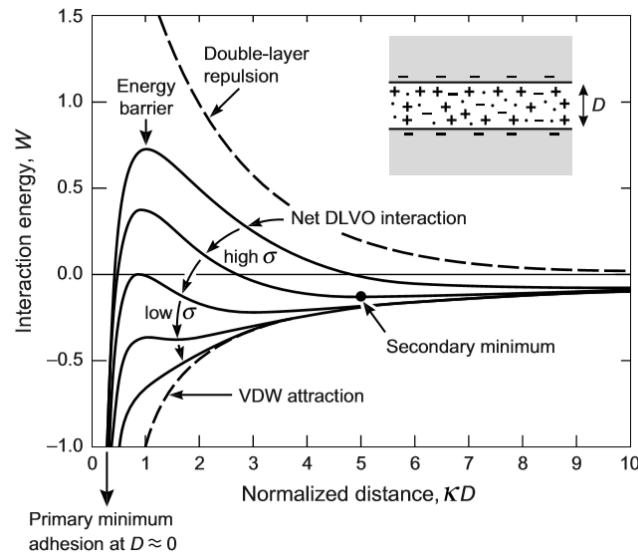


**Figure 2. 2<sup>40</sup>** Schematic energy versus distance profiles of the DLVO interaction.  $\sigma$  represents the surface charge density;  $D$  represents the distance between two surfaces.

While the DLVO theory can be used to predict the interactions in colloidal system, there are disparities between experimental results and the predictions. The limitation of the DLVO theory arises due to the neglect of nonlinear effects in the Poisson-Boltzmann Equation (Equation 2 - 4) and the neglect of the boundary conditions at the particles' surfaces.

This causes big impact on the electrostatic interaction energy at contact. Some efforts in expanding the capabilities of the DLVO theory went toward the basic part of the theory while doubting that only two types of interactions in terms of electrostatic and van der Waals between colloidal particles exist. Refinements like solvation forces<sup>41</sup> and hydrodynamic retardation<sup>42</sup> have been proposed as additional forces. Some other explanations<sup>43-45</sup> for the failure of the DLVO theory were proposed within the framework of the electrostatic and van der Waals forces and tried to modify the mean field Poisson-Boltzmann theory<sup>46-47</sup> which has been commonly used to resolve the electrostatic potential of charged colloidal particles in the presence of dissolved ions. Another limitation of the DLVO theory has been proposed to be related to the nature of colloidal particles. The heterogeneity of surface charge has been assumed by Kihira *et al.*<sup>48</sup> They showed that the discrepancies in the coagulation rates can be perfectly bridged if the discreteness of the surface charge is taken into consideration.

In addition, even without attractive potential, colloidal assembly is still possible due to the confinement effects which can be translated into effective interparticle potentials, known as the depletion forces.<sup>49</sup> Depletion interactions are caused by the addition of small, non-adsorbing species to a colloidal suspension. These additional species can be nanoparticles, polyelectrolytes, or polymers. They have a tendency to assemble near the surface of the colloids and promote attractive or repulsive colloidal interactions in dilute systems or provide a driving force for order in concentrated systems. Considering a colloidal system consisting of hard spheres with two different diameters, the smaller particles are excluded from the surface of the larger particles by a depletion zone with a thickness of  $T$ . The depletion zones overlap as the larger particles approach. A volume of solution between the larger particles known as the depletion volume is created. In the depletion volume, the concentration of the smaller particles is lower than that in the bulk solution. The difference in osmotic pressure between the bulk solution and this depletion volume leads to a net attractive force between the colloids.<sup>50</sup> This depletion interaction is illustrated in Figure 2. 3. The Walz and Sharma (WS) depletion model<sup>51</sup> is appropriate for binary mixtures of colloids and highly charged nanoparticles.

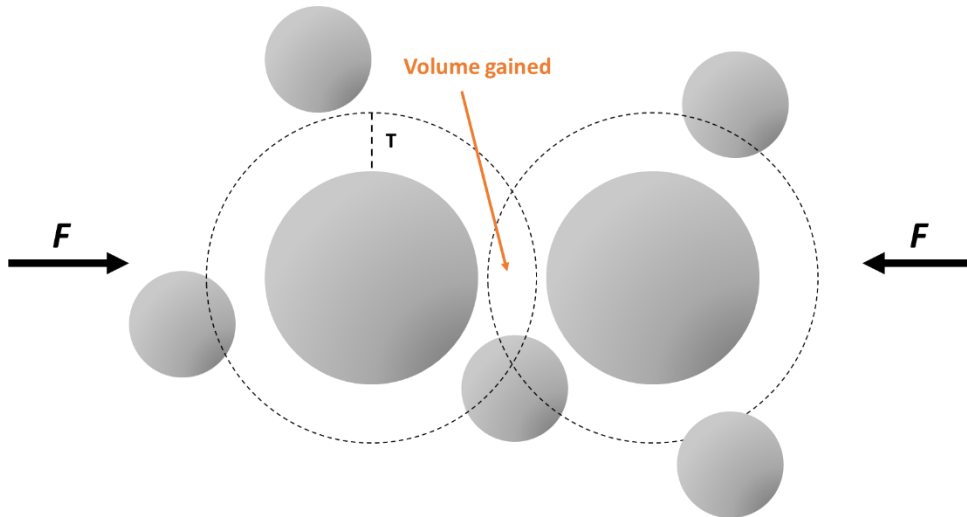


**Figure 2. 3 Depletion interaction.** As two larger particles approach, the depletion zones overlap and therefore the deletion volume is gained. The difference in osmotic pressure between the bulk solution and this depletion volume leads to a net attractive force (black arrows).

### 2.1.3 Centrifugal field-directed colloidal assembly

Besides colloid-colloid interactions, external fields (*e.g.*, gravitational, electric, magnetic) can also influence the assembled structures from colloidal systems. The volume fraction of colloids in a dispersion is an important parameter which can influence the thermodynamic state of the dispersion. As mentioned in the last part of 2.1.2, for binary hard-sphere systems, in which the colloids only interact via an excluded volume term, the volume fraction of colloids is even the only determining thermodynamic variable.<sup>52</sup> Therefore, in the colloidal assembly process, the volume fraction is an important parameter to control, preferably in situ.

Centrifugation is a good method to increase the volume fraction of colloids in a dispersion. When the density of the colloids is different from the density of the solvent, the local volume fraction of a colloidal dispersion is affected by the centrifugal field. If the colloids have a larger density than the density of the solvent, the colloids sink, while otherwise they float. By tuning the densities of colloids and the dispersion solvent, the speed of colloidal compaction can be flexibly controlled. For a system which consists of more than one component, more complexity can be brought by the centrifugal field. The centrifugal field does not only serve as a driving force to bring particles together, but can also be used advantageously for separating two species in a dispersion. In my master's work,<sup>53</sup> the centrifugal field has been demonstrated to hold a great potential for the assembly of binary colloidal systems. However, other than this work, the use of centrifugal field to trigger colloidal assembly is very restricted, mainly due to the lack of control over the colloid volume fraction in the compaction process. In this work, we

incorporated analytical ultracentrifugation to trace the sedimentation or floatation of colloidal particles in a quantitative level and further take the advantage of the centrifugal field in multinary colloidal assembly.

#### 2.1.4 General analytical ultracentrifugation

Analytical ultracentrifugation (AUC) is a powerful nanoparticle characterization tool which combines an extremely high resolution up to Angstrom resolved particle size distributions<sup>54</sup> with high statistical accuracy. It has been widely applied in biochemistry,<sup>55</sup> biophysics and pharmacy.<sup>56-57</sup> In physical and colloidal chemistry AUC has been less extensively employed compared to the field of biophysics even though AUC was initially developed by Svedberg and co-workers<sup>55-56, 58</sup> in the 1920s to study gold particle size distributions.

Nanoparticles can be dissolved in a solution or dispersed in a liquid, put in the AUC cell and be spun in a range of 1000-60000 rpm (rotations per minute) in equipment like the commercial Beckman Analytical Ultracentrifuge. Experiments are performed with controlled rotational speed and temperature.

When a solute particle is suspended in a solvent and subjected to a gravitational field, it faces three main forces, see Figure 2. 4:<sup>59</sup>

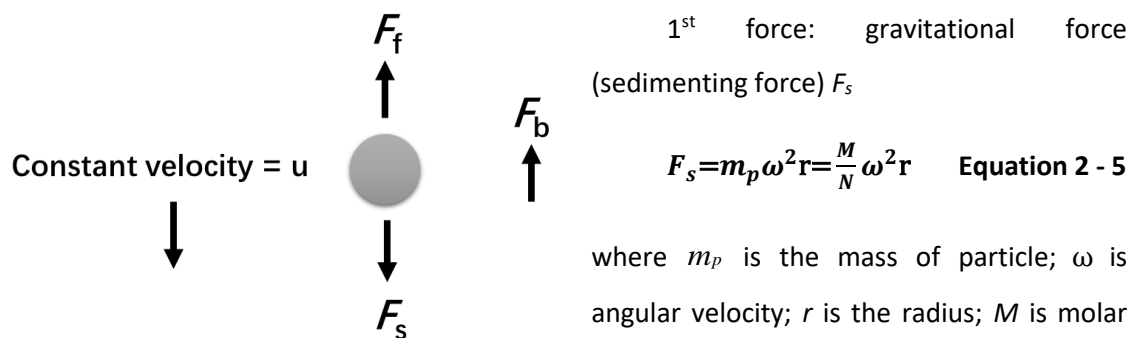


**Figure 2. 4 The forces acting on a particle suspended in a gravitational field**

2<sup>nd</sup> force: the buoyancy force  $F_b$

$$F_b = -m_s \omega^2 r = -m_p \bar{v} \rho_s \omega^2 r = -\frac{M}{N} \bar{v} \rho_s \omega^2 r \quad \text{Equation 2 - 6}$$

where  $m_s$  is the mass of displaced solvent;  $\bar{v} = (\rho_p)^{-1}$  is the partial specific volume of the solute.

3rd force: frictional force  $F_f$

$$F_f = -fu \quad \text{Equation 2 - 7}$$

where  $f$  is the frictional coefficient,  $u$  is the sedimentation velocity of the solute.

Within a very short time the three forces balance with each other:

$$F_f + F_s + F_b = 0 \quad \text{Equation 2 - 8}$$

Equation above can be rearranged to obtain the sedimentation coefficient in the forms of Equation 2 - 9:

$$s = \frac{M(1-\bar{v}\rho_s)}{Nf} = \frac{u}{\omega^2 r} \quad \text{Equation 2 - 9}$$

The diffusion coefficient of spherical particle can be resolved by the Stokes-Einstein equation (Equation 2 - 10):

$$D = \frac{k_b T}{6\pi\eta r} \quad \text{Equation 2 - 10}$$

where  $k_b$  is Boltzmann's constant,  $T$  is the absolute temperature,  $\eta$  is viscosity,  $r$  is the radius of the spherical particle.

Therefore, Equation 2 - 9 can also be written in the form of Equation 2 - 11, which is known as the Svedberg equation:

$$s = \frac{M(1-\bar{v}\rho_s)D}{RT} = \frac{u}{\omega^2 r} \quad \text{Equation 2 - 11}$$

The sedimentation coefficient has a unit of  $10^{-13}$  seconds. The Svedberg unit is defined as  $10^{-13}$  seconds, in honor of the Swedish scientist Svedberg.

The sedimentation coefficient derived from above assumes the solute particles in a centrifugal field to be hard spheres. Batchelor<sup>60</sup> made a calculation (Equation 2 - 12) of the friction coefficient at low volume fractions for Brownian hard spheres in a dilute dispersion.

$$\frac{f_0}{f} = \frac{U}{U_0} = 1 - 6.55\phi \quad \text{Equation 2 - 12}$$

where  $U$  is the average sedimentation velocity,  $\phi$  is the particle volume fraction with the subscript denoting the corresponding parameters at infinite dilution. It shows that the friction coefficient  $f$  increases linearly with the volume fraction  $\phi$ .

However, compared to hard spheres, a pronounced retardation of the average sedimentation velocity exists in a sufficiently concentrated colloidal dispersion. For example, the

long range repulsive forces between colloidal particles may prevent them to come as closely to each other as in the case with hard spheres. In contrast to Equation 2 - 12, the volume fraction dependence turns to be an exponential function (Equation 2 - 13) which has been found both experimentally and theoretically.<sup>61</sup>

$$\frac{f_0}{f} = 1 - p\phi^\alpha, 0 < \alpha < 1 \quad \text{Equation 2 - 13}$$

where  $p$  is a positive constant. Therefore the average sedimentation velocity may display a deep decrease even at very low volume fraction  $\phi$ .

An empirical Equation 2 - 14 can be used to approximate the relationship between the particle concentration and the sedimentation which is measured at the corresponding concentration.

$$s = \frac{s^0}{(1+k_s c)} \quad \text{Equation 2 - 14}$$

where  $s^0$  is the ideal sedimentation coefficient,  $c$  is the concentration at which  $s$  was determined,  $k_s$  is the concentration-dependence coefficient.

The analytical ultracentrifugation (AUC) distinguishes itself from the preparative centrifuges by the analytical properties, and these properties are due to its optical detector. A scheme of AUC can be found in Figure 2. 5. Light is emitted by a lamp, goes through the AUC cells and reaches the detector. The most commonly used optical detectors are UV/Vis absorption and interference optics, while Schlieren optics, turbidity detectors and Fluorescence detectors have also been developed. The direct collection of an AUC experiment is a set of concentration measurements at different radial positions and at a given time.

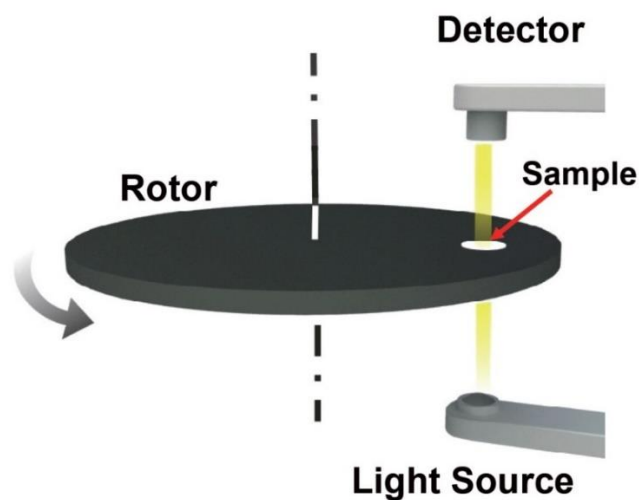


Figure 2. 5 Scheme of analytical ultracentrifugation.

Absorbance optics measure the UV/Vis absorbance between wavelengths of 200 nm and 800 nm. When a desired cell passes under the optics, the Xenon lamp is triggered to emit light. Light is reflected by a toroidal diffraction grating which makes the light monochromatic to the selected wavelength. After that a reflector reflects 8% of the parallel light it receives to the incident light detector. An image system is included for radial scanning. A slit below the sample allows choosing specific radial positions that the light passes through. The light intensity afterwards is detected by the photomultiplier tube. The absorbance can then be calculated with the Lambert-Beer Law:

$$A = \lg \frac{I_0}{I} = \varepsilon \cdot c \cdot a \quad \text{Equation 2 - 15}$$

where  $A$  is the absorption;  $I$  is the intensity that passes through sample sector;  $I_0$  is the intensity passing through reference sector;  $\varepsilon$  is the extinction coefficient;  $a$  is the thickness of the cell.

There are mainly two types of AUC experiments: sedimentation velocity and sedimentation equilibrium. The sedimentation velocity is the most important AUC experiment for nanoparticle characterization.<sup>56</sup> The sedimentation velocity data are used to define the distribution of the sedimentation coefficient which can then be converted to required information like molecular weight distribution or particle size distribution.<sup>62</sup>

#### Lamm equation

In sedimentation velocity experiments, sedimentation is dominant compared to diffusion. The particles in the solution are initially homogeneously distributed in the centrifuge cell. The centrifugal field causes the solutes to sediment rapidly towards the bottom of the cell. A boundary is formed between the solute depleted region and the uniform concentration of solute (the plateau), as shown in Figure 2. 6.

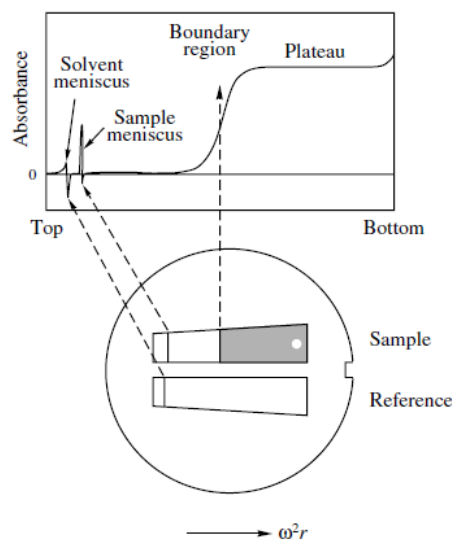


**Figure 2. 6<sup>1</sup> Double-sector centerpiece in an AUC cell.**

The movement of the boundary can be measured and used to determine the sedimentation coefficient instead of resolving the velocity of each individual particle. Reading the boundary displacement with time is the simplest analytical method to derive a

sedimentation coefficient from experimental data. However, in this way the diffusional broadening which can contain rich information is neglected.

Thus, in general it is necessary to concern about the possible dependence of  $D$  (diffusion coefficient) as well as  $s$  (sedimentation coefficient) on  $c$  (concentration).<sup>63</sup> The Lamm equation

$$\frac{dc}{dt} = D \left( \frac{\partial^2 c}{\partial r^2} + \frac{1}{r} \frac{\partial c}{\partial r} \right) - \omega^2 s \left( r \frac{\partial c}{\partial r} + 2c \right) \quad \text{Equation 2 - 16}$$

is a general equation to fit the AUC data. It describes the local concentration  $c$ , variations of the samples with time  $t$  in the centrifugal field  $\omega^2 t$  due to diffusion and sedimentation. There is no possible analytical solution to Lamm equation. Among several approximate analytical solutions, the Faxén-type (1929) approximate solution is the simplest, which can be written as Equation 2 - 17

$$c(r, t) = \left( \frac{c_0 e^{-2s\omega^2 t}}{2} \right) \left[ 1 - \Phi \left( \frac{r_m (\omega^2 s t + \log(r_m) - \log(r))}{2\sqrt{Dt}} \right) \right] \quad \text{Equation 2 - 17}$$

with  $\Phi$  denoting the error function.

Some frequently used strategies for determining sedimentation coefficient distributions are outlined in the following part.

#### The van Holde-Weischet

$G(s)$  is the integral sedimentation coefficient distribution introduced by van Holde and Weischet (vHW)<sup>64</sup> in 1978. It is a graphical extrapolation method for deconvoluting diffusion in sedimentation boundaries. This approach is based on the idea that diffusion and sedimentation proceed with the a square-root of time and linear with time, respectively. The sedimentation boundaries are divided into fractions (horizontal slices) reflecting the radii  $R_i$  of certain intervals of the fractional plateau concentration. Then a transformation of radius into apparent sedimentation coefficients  $s^*$  can be made with:

$$s^* = \frac{\ln(r_{bnd}/r_m)}{\omega^2 t} \quad \text{Equation 2 - 18}$$

where  $s$  is sedimentation coefficient,  $r_{bnd}$  is the radius point of measurement point,  $r_m$  is the radius of meniscus,  $\omega^2 t$  is the run time integral.

The  $s_i^*$  values of different scans are extrapolated to infinite time according to Equation 2 - 19.

$$s_i^*(t) = s - \frac{2\sqrt{D}}{\omega^2 r_m} \Phi^{-1} \left( 1 - \frac{2t}{N} \right) \times \frac{1}{\sqrt{t}} \quad \text{Equation 2 - 19}$$

G(s) is a good approach to extract qualitative information from the sedimentation process, as the graphical extrapolation allows to compare the sedimentation velocity of different parts of the boundary. But for small proteins, a drawback of this method is the requirement of the selection of the subset of experimental scans for the analysis. It is not always possible to have scans which exhibit clear solution and solvent plateaus permitting the boundary division.

#### Apparent sedimentation coefficient distribution $g^*(s)$

The time derivative (dc/dt) method is another strategy to analyze experimental sedimentation coefficient distributions. The distribution from the dc/dt approach has been termed  $g(s^*)$  and reads in the form of Equation 2 - 20.

$$g(s^*)_t = \left\{ \frac{\partial \left[ \frac{c(r,t)}{c_0} \right]}{\partial t} \right\} \left[ \frac{\omega^2 t^2}{\ln \left( \frac{r_m}{r} \right)} \right] \left( \frac{r}{r_m} \right)^2 \quad \text{Equation 2 - 20}$$

with  $c_0$  denoting the initial loading concentration.

This dc/dt based method is very important as the time invariant noise can be subtracted, such as window scratches, dirt and refractive index heterogeneities in the windows. Unlike the vHW method, the dc/dt method hypothesizes non-diffusing particles. Therefore, when the diffusional boundary broadening can be negligible in the case of sufficiently large and dense colloids sedimenting at high rotor speeds,  $g(s^*)$  equals the true distribution  $g(s)$ . If diffusion is not negligible, the  $g(s^*)$  should be considered as the apparent sedimentation coefficient. There are basically two approaches to calculate the apparent sedimentation coefficient distribution. One way is through extrapolating of  $g(s^*)$  curves calculated for different times to infinite time. The other way is based on a direct least-squares fit of the data with an integral equation for the distribution (termed ls- $g^*(s)$ ). This can be realized by directly fitting Equation 2 - 21 to the experimental data. The ls- $g^*(s)$  distribution is implemented in SEDFIT.

$$a(r, t) \cong \int g^*(s) U(s, r, t) ds \quad \text{Equation 2 - 21}$$

The  $g^*(s)$  and the integral G(s) distribution by van Holde-Weischet are conceptual connected via extrapolation of  $g^*(s)$  to infinite time. If the  $g^*(s)$  is extended from an apparent distribution of non-diffusing particles to the distribution of diffusing particles, we will come across the c(s) distribution.

Sedimentation coefficient distribution  $c(s)$ 

The  $c(s)$  distribution takes into account the diffusion of sedimenting species. This is achieved by an extension of Equation 2 - 21, in which the full solution of the Lamm equation is considered for each sedimenting species:

$$a(r, t) \cong \int c(s) \chi_1(s, D(s), r, t) ds \quad \text{Equation 2 - 22}$$

where  $\chi_1(s, D(s), r, t)$  is the normalized Lamm equation. By using Equation 2 - 22, sharp features of sedimentation coefficients can be found. The  $c(s)$  method can use the whole data set of sedimentation velocity profiles, which is a distinct advantage over the  $g^*(s)$  and  $v_{HW}$  methods. Also the  $c(s)$  can be transformed into a molar mass distribution  $c(M)$  by applying the Svedberg equation (Equation 2 - 11) for each pair of  $s$  and  $D$ .

More detailed discussion about the sedimentation velocity experiment and the evaluation methods can be found in several review papers and books.<sup>1, 65-66</sup> In the following part, the sedimentation equilibrium (SE) will be briefly introduced.

Compared to sedimentation velocity experiment, in sedimentation equilibrium experiments, a small amount of sample is centrifuged at a velocity which is lower than that of a sedimentation velocity experiment. The diffusion and the sedimentation processes oppose each other. They reach an equilibrium after an appropriate centrifuge time which is proportional to the square of the solution column height. Sedimentation equilibrium is established when the concentration distribution of the solute stays invariant with time. At equilibrium, the concentration of the solute remains low at the top part of the centrifuge cell and increases exponentially toward the bottom, see Figure 2. 7.

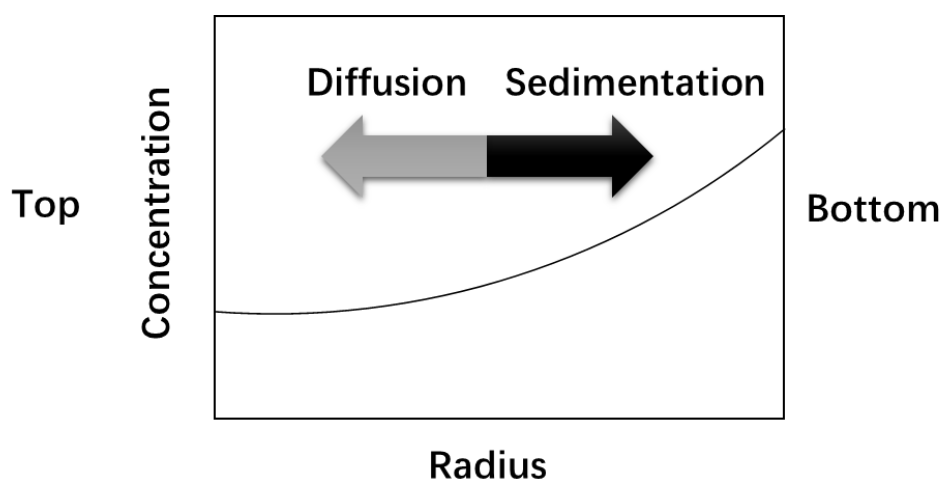


**Figure 2. 7** Scheme of the concentration distribution of sedimentation equilibrium

The total potential of solute is the same everywhere in the centrifuge cell at equilibrium. The sedimentation tendency at the bottom of the cell is much greater as the sedimentation flow is proportional to  $\omega^2 r$  ( $r$  increases towards the cell bottom). Diffusion also shows a greater balancing tendency in the opposite direction because of the gradient of chemical potential.

For a single, ideal, nonassociating species (i.e. no repulsive interactions due to volume exclusion or charge interactions), the concentration distribution at equilibrium can be described as follows

$$a(r, t) = c(r_0) \varepsilon d \exp[M(1 - \bar{v}\rho_s)] \frac{\omega^2}{2RT} (r^2 - r_0^2) \quad \text{Equation 2 - 23}$$

where  $c(r_0)$  is the concentration at a reference radius,  $\varepsilon$  is the molar extinction coefficient,  $d$  is the optical path length. Different oligomeric states should be populated at different concentration ranges which makes the sedimentation equilibrium a powerful tool for determining the molecular weights of macromolecules with Equation 2 - 24.

$$M = \frac{2RT}{(1 - \bar{v}\rho_s)\omega^2} \times \frac{d(\ln c)}{dr^2} \quad \text{Equation 2 - 24}$$

### 2.1.5 Porous materials

International Union of Pure and Applied Chemistry (IUPAC) classifies porous materials into three categories microporous with pores of less than 2 nm in diameter, mesoporous having pores between 2 and 50 nm, and macroporous with pores greater than 50 nm.<sup>67</sup> The presence of pores (holes) in a material can render itself many useful properties that the corresponding bulk material would not have. Porous materials in the nanoscale possess a high surface to volume ratio, a high surface area and large porosity. The synthesis of uniform nanoporous materials in general remained a challenge until the templating strategy was proposed by Knox *et al.*<sup>68</sup> Since then, many uniform porous materials with pore size differing from micro, meso to macro scale have been successfully synthesized by using various template<sup>12</sup> and explored in functional applications such as catalysis, chromatography, separation, and sensing.

Specifically, for three-dimensionally ordered macroporous materials (3DOM), the concept for the preparation is strongly connected to the assembled colloidal structures: a close-packed colloidal crystal template is firstly prepared; then the template is infiltrated with liquid or gas phase precursors; by removing the template via either thermal processing, solvent exaction, or chemical etching, 3DOM materials are obtained. Thus, the microstructure of the 3DOM

materials inherits the structure of the colloidal template and is normally comprised of solid walls with tens of nm in thickness in between close-packed spherical voids.

The important role of colloidal templates in developing the 3DOM functional materials is very evident in photonic crystals which are among the most important classes of 3DOM materials. Photonic crystals are a kind of 3DOM materials derived from ordered arrays of monodisperse spheres. A typical feature of such kind of materials is the versatility for changing the characteristic reflection peaks in their optical spectra (the “stop bands”). The optical reflection peaks are similar to diffraction peaks in X-ray powder patterns. But the magnitudes fall into the sub micrometer range which is comparable to the wavelength of visible light instead of the angstrom range. One practical way to change the stop band positions is to change the lattice constant (the spacing between spheres). If the variation of the lattice constant can be changed reversibly by applying external stimuli, photonic crystals with tunable color would be realized.

As shown in the photonic crystals example, the 3DOM materials obtained via the templating strategy are highly dependent on the colloidal template. A colloidal template with a novel structure might probably bring brand new properties to the final porous structures. This is the motivation of this thesis to go one step further to the porous materials, beyond the study of colloidal assembly.

## 2.2 Relevant synthesis and analytical techniques

Several standard analytical methods like Infrared Spectroscopy, Raman spectroscopy, powder X-ray diffraction, etc. were used (see experimental part) in this work. The most relevant analytical techniques for the characterization of nanoparticle size distributions and the nanostructures used in this work, like dynamic light scattering, analytical ultracentrifugation, scanning electron microscopy, will be briefly explained in this section.

### 2.2.1 Dynamic light scattering

Light scattering is a consequence of the interaction of light with the electric field of a small particle or molecule. When light impinges on matter, an oscillating dipole in the electron cloud is induced. As the dipole changes, energy is radiated in all directions. This radiated energy is called “scattered light”. The size, shape and molecular interactions in the scattering material determine the frequency shifts, the angular distribution, the polarization, and the intensity of the scattered light. Therefore, with the aid of electrodynamics and theory of time dependent

statistical mechanics, it is possible to get information about the structure and molecular dynamics of the scattering medium through the light scattering characteristics of the system.

Rayleigh theory is applicable for small particles and molecules with diameters less than 1/10 of the incident laser wavelength ( $\lambda$ ). For the commonly used He-Ne laser ( $\lambda = 633$  nm), the applicable size equates to particles smaller than 60 nm. Such small particles produce isotropic scattering which is equal in all directions. The intensity of the scattered light  $I$  is proportional to  $d^6$  (Equation 2 - 25).

$$I \propto d^6 \qquad \text{Equation 2 - 25}$$

Mie theory describes how spherical particles of all sizes scatter light. When the size of particles is larger than 1/10 of the incident laser wavelength ( $\lambda$ ), the scattering is no longer isotropic but changes to a distortion in the forward scattering direction. If the size of the particles becomes comparable or larger than the laser wavelength ( $\lambda$ ), the scattering becomes a complex function with maxima and minima with respect to the angle. Mie theory explains the maxima and minima in the plot of intensity.

Brownian motion is the random movement of particles due to collisions caused by bombardment by the solvent molecules that surround the particles. The factors that influence the speed of the Brownian motion include particle size, solvent viscosity and temperature. The speed of the Brownian motion is inversely proportional to the particle size and proportional to the temperature. The smaller the particle is, the more rapid the Brownian motion becomes. The higher the temperature the more rapid the Brownian motion. The translational diffusion coefficient ( $D$ ) which defines the velocity of the Brownian motion can be converted into the particle size using the Stokes Einstein equation (Equation 2 - 26).

$$d_H = \frac{kT}{3\pi\eta D} \qquad \text{Equation 2 - 26}$$

where  $d_H$  is the hydrodynamic diameter,  $k$  is the Boltzmann's constant,  $T$  is the absolute temperature,  $\eta$  is the viscosity of the solvent and  $D$  is the diffusion coefficient.

Here, the hydrodynamic diameter ( $d_H$ ) is the diameter of a hard sphere that diffuses at the same speed as the particle being measured. Therefore, a sum of the size of the particle core, the surface structures of the particle, and the ions in the medium decide the hydrodynamic diameter ( $d_H$ ).

In a light scattering experiment, light is emitted by a laser and passes through polarizer to define the polarization of the incident beam and then impinges on the scattering medium. Before the scattered light finally enters a detector, it passes through an analyzer which selects a given polarization. A scheme of the dynamic light scattering instrument is shown in Figure 2.8. A time dependent fluctuation in the scattering intensity due to the fact that the small molecules in solutions are undergoing Brownian motion can be observed. Therefore, the distance between the scattering sites in the solution is constantly changing with time. This scattered light then undergoes interference by the surrounding particles, and within this intensity fluctuation, information is contained about the time scale of movement of the scattering sites.

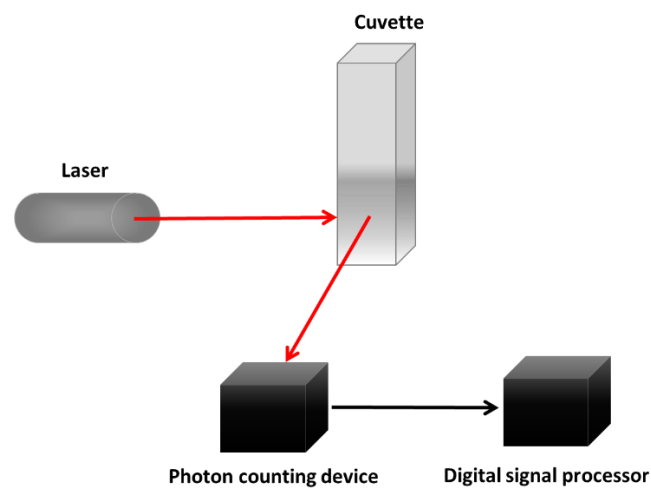


**Figure 2. 8 Scheme of a dynamic light scattering instrument**

Correlation is a technique for monitoring the time dependence of light intensity fluctuation. The dynamic information of the particles is derived from an autocorrelation function  $G(\tau)$  (Equation 2 - 27) of the intensity trace recorded during the dynamic light scattering experiment:

$$G(\tau) = \frac{\langle I(t)I(t+\tau) \rangle}{\langle I(t) \rangle^2} \quad \text{Equation 2 - 27}$$

where  $\tau$  is the correlator delay time,  $t$  is the time and  $I$  is the intensity, the angular brackets denote the expected value operator.

At short time delays, the correlation is high because the particles do not have a chance to move far away from the initial state. Compared to the initial signal, the new one obtained after a very short time interval is thus essentially unchanged. As the time delays become longer, the correlation decays exponentially. There is no correlation between the scattered intensity of the

initial and final states. By using the cumulant analysis, the correlation function can be modelled with an exponential expression shown in Equation 2 - 28 and Equation 2 - 29:

$$\mathbf{G}(\tau) = \mathbf{B} + \mathbf{A}\Sigma\exp(-2q^2\mathbf{D}\tau) \quad \text{Equation 2 - 28}$$

$$\mathbf{q} = (4\pi n/\lambda_0)\sin(\theta/2) \quad \text{Equation 2 - 29}$$

where B is the baseline at infinite time, A is the intercept, q is the scattering vector, n is the dispersant refractive index,  $\lambda_0$  is the laser wavelength,  $\theta$  is the detection angle, D is the diffusion coefficient. This exponential decay is related to the motion of the particles, specifically to the diffusion coefficient. To fit the decay (i.e., the autocorrelation function), numerical methods are needed. If the sample is monodisperse, the decay is simply a single exponential.

### 2.2.2 Analytical ultracentrifugation --- particle size distributions

The accessibility to high resolution particle sizes and particle size distributions establishes the important role of analytical ultracentrifugation in the modern analysis of colloids. The definition of the sedimentation coefficient and the method to obtain the sedimentation coefficient have been introduced in 2.1.4. The particle size can be conveniently converted from the sedimentation coefficient.

Equation 2 - 9 can be written into another form:

$$s = \frac{V(\rho_p - \rho_s)}{f} \quad \text{Equation 2 - 30}$$

where s is the sedimentation coefficient, V is the particle volume,  $\rho_p$  and  $\rho_s$  are the density of particle and solvent respectively, f is the frictional coefficient.

Assume the validity of Stokes' law, e.g., the colloidal particles are all perfectly spherical and the bare particle radius equals the hydrodynamic radius, the frictional coefficient f can be derived as follows:

$$f = 3\pi\eta_s d_p \quad \text{Equation 2 - 31}$$

where  $d_p$  is the diameter of particle,  $\eta_s$  is the viscosity of the medium. If Equation 2 - 31 is substituted into Equation 2 - 30, the following Equation 2 - 32 which gives the particle size from the sedimentation coefficient can be derived:

$$d_p = \sqrt{\frac{18\eta_s s}{(\rho_p - \rho_s)}} \quad \text{Equation 2 - 32}$$

Therefore, from the above equation, it can be concluded that the density of the sedimenting particle is crucial in the conversion of sedimentation coefficient to the particle size. For most colloids, the density is usually known precisely from the chemistry when preparing the particles. However, it is necessary to combine the results with the analysis from density insensitive methods like dynamic light scattering and flow-field-flow fractionation, in the cases of composite, core-shell and very small (<5 nm) particles.

Compared to the electron microscopy which determines the particle size distribution from counting at least a thousand particles, analytical ultracentrifugation is a rapid technique to obtain reliable statistics. In addition, the measurement depends on the fractionation of particles on the base of sizes and densities. The in situ character eliminates the drying effects which often arise with electron microscopy.

### 2.2.3 Scanning electron microscopy (SEM)

The scanning electron microscope (SEM) uses a focused beam of high energy electrons to generate a variety of signals at the surface of solid specimens. The signals contain information about the sample's surface topography and composition.

Accelerated electrons in an SEM carry significant amounts of kinetic energy, and this energy is dissipated as a variety of signals produced by electron-sample interactions when the incident electrons are decelerated in the solid sample. The types of signals include secondary electrons (SE), back-scattered electrons (BSE), characteristic X-rays, light (cathode luminescence) (CL), specimen current and transmitted electrons.<sup>69</sup> SE are most valuable for showing morphology and topography on samples. Discrimination of phases based on mean atomic number can be achieved by using BSE. CL can be used to generate compositional maps based on differences in trace element "activators" (typically transition metal and Rare Earth elements).

Essential components of a SEM include electron gun, electron lenses, scanning system, liner tube, specimen chamber, Everhart-Thornley electron detector and vacuum system, see Figure 2. 9.

In a typical SEM, the electron gun, which is at the top of the electron column, provides a source of electrons. Electrons are emitted from either tungsten which has the highest melting point and lowest vapour pressure of all metals, or lanthanum hexaboride (LaB6) cathodes or via field emission and accelerated down the evacuated column. A vacuum is necessary because electrons can only travel a very short distance in air. The electron beam is demagnified by two

or three electron lenses to a small spot about 5-50 nm in diameter, which typically has an energy ranging from 0.2 keV to 40 keV. The lens closest to the gun is called the condenser lens while the lens closest to the specimen is called the final lens. The final lens is used to move the smallest cross section of the beam up and down until it meets the surface of the specimen. This corresponds to a focused image. The beam passes through pairs of scanning coils or pairs of deflector plates in the electron column, typically in the final lens, which deflect the beam in the x and y axes so that it scans in a raster fashion over a rectangular area of the sample surface. The electrons lose energy when interacting with the sample by random scattering and absorption within less than 100 nm to around 5 μm into the sample surface. The energy exchange between the electron beam and the sample results in the reflection of high-energy electrons by elastic scattering, emission of secondary electrons by inelastic scattering and the emission of electromagnetic radiation, each of which can be detected by specific detectors. The images are created from the specimen current distribution.

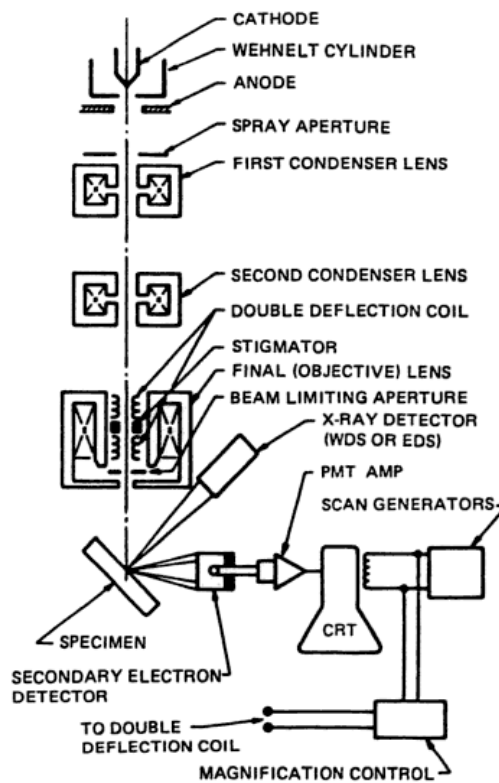


Figure 2. 9.<sup>70</sup> Schematic diagram of the parts of the electron column.

### 3. Scope

Colloidal systems are not only closely related to many fundamental scientific questions, but a good platform for the constructions of functional nanomaterials. While a centrifugal field in principle is a powerful method to study the colloidal systems as it can be used as a compaction driving force, fractionation tool and analysis platform, it has been very seldom explored mostly due to the lack of control. The aim of this work is to obtain fundamental understanding of colloidal assembly in a centrifugal field through the analytical support of analytical ultracentrifugation (AUC), and furthermore develop innovative functional materials in the centrifugal field.

The exploration starts with a colloidal system containing monodisperse polystyrene latex spheres. Although the monodisperse system has been very intensively studied over the past few years, some exciting aspects remain open. There are a lot of research works on the light localization phenomena which has been only observed experimentally in 1D and 2D materials. One of the biggest obstacles in the study of three dimensional light localization lies in the materials with photonic glass structure. To preserve the photonic glass nanostructure to a macroscopic scale which is comparable to the laser spot size is a big challenge. In the current work, AUC is involved to identify the different species generated by adding electrolytes to the electrostatic stabilized latex dispersions and correlate to different disordered colloidal assembly structures. Furthermore, the controlled disorder is scaled up by preparative centrifuge to a macroscopic free-standing monolith which is ideal for further optical investigations. The established method in principle can be implemented to other colloidal particles to build up various materials with photonic glasses nanostructure.

As a centrifugal field assisted with the analytical power from AUC demonstrates its great potential in directing monodisperse colloidal assembly, one more component is added to create a binary system which consists of polystyrene latex spheres with two different sizes. Binary colloidal systems are good model systems to study the ionic crystal which is composed of two spheres (atoms). Compared to monodisperse systems, binary or multinary colloidal systems are much more complex. For example, segregation of granular matter is an extensive research topic for a long time due to its important role in both scientific and industrial practice. There is not yet a satisfactory explanation for the puzzling Brazil nut effect, i.e. larger species in a jar of mixed nuts rising to the top upon shaking. Thus, new techniques have been called for manipulating and understanding binary colloidal assembly. The investigations in current work are pioneer explorations which adopt AUC analysis to gain control over sedimentation and separation

behavior of the binary systems. Through precisely tuning the centrifugal field, binary phases over a range of compositions emerge.

Apart from the insights into the formation of glasses and metastable solids, the structures assembled from binary colloidal systems build up a solid foundation for developing functional materials with structural gradient on the nanoscale, for example nanoporous materials as mentioned in the introduction part. Gradient materials like tendons in human body have been found to be clever designs of nature. Researchers are motivated to learn from nature and synthesize gradient materials for different uses. But this imitation of nature is just at the starting phase with difficulties like creating and preserving the gradient. In addition, the freestanding form of materials, which is required when testing the directional property of the gradient, is a big challenge. Therefore, in the last part of this thesis which deals with both binary and ternary colloidal systems, all the prior knowledge from the earlier parts of this thesis is applied aiming to fabricate a functional material with a defined gradient pore-structure. The resulting freestanding carbon materials with gradient porosity were tested as electrodes in the Li-O<sub>2</sub> cell. It was proven that not only the gradient structure influences the performance of the cell, but also the direction of the gradient is of great importance.

Results from this thesis have been published:

[1] Chen, M.; Cölfen, H.; Polarz, S., Centrifugal Field-Induced Colloidal Assembly: From Chaos to Order. *ACS nano* 2015, 9 (7), 6944-6950.

[2] Chen, M.; Hagedorn, K.; Cölfen, H.; Polarz, S., Functional Gradient Inverse Opal Carbon Monoliths with Directional and Multinary Porosity. *Advanced Materials* 2017, 29 (2), 1603356-n/a.

## 4. Results and discussion

### 4.1 Assembly of monodisperse colloidal system in the presence of additional electrolytes

In a colloidal dispersion, if the solid phase is built up of uniform spherical nanoparticles, for example polymeric latex spheres, regular and periodic arrays which are known as colloidal crystals can be formed under suitable conditions. Colloidal crystals have been intensively investigated over the past two decades and play an important role in photonic crystal design.<sup>71</sup>

While photonic crystals take advantage of the periodicity in the dielectric constant and thus can be used in the precise manipulation of ballistic photons, the random media as the other extreme system known as photonic glasses can also strongly affect light transport and exhibit interesting physical phenomena like random lasing and light localization.<sup>10-11</sup> For photonic glasses, the monodispersity of the particles is of great importance, as with polydisperse particles the individual electro-magnetic response of each particle gives rise to an averaged-out optical response.<sup>72</sup>

Contrary to intuition, arbitrarily obtaining high degrees of disorder from monodisperse building blocks is not an easy task. Few methods like rapid sedimentation or modified vertical deposition have been proven to be not successful.<sup>73</sup> Resonant behavior of the scattering strength in monodisperse random media was reported<sup>74</sup> by which a new scattering regime might be reached in higher refractive index materials. Garcia *et al*<sup>75</sup> have done the pioneer work and developed two promising routes to fabricate random materials from monodisperse colloidal particles by either chemically selectively etching one of the two kinds of spheres in a binary colloidal crystals, or introducing electrolytes to the monodisperse latex spheres dispersion to encourage colloidal aggregation.

Although the coagulation route is easy to handle and the coagulation of a charged colloidal dispersion has always been a core aspect of colloidal science,<sup>76</sup> it was exclusively conducted in an empirical way. Figure 4.1 - 1 shows the colloidal packing obtained from drying a monodisperse polystyrene colloidal dispersion under gravity. It can be easily found that the degree of disorder in the colloidal packing increases as the amount of CaCl<sub>2</sub> increases. When there is no additional salt present in the polystyrene dispersion, an ordered *fcc* arrangement was observed in Figure 4.1 - 1a. In the presence of electrolyte, the stability of a colloidal dispersion in which the colloidal particles are electrically charged decreases, due to the charge screening by the electrolyte. The degree of order is getting lower and thus more voids are

introduced when the concentration of  $\text{CaCl}_2$  increased from 5.3mM (Figure 4.1 - 1b) to 10.7mM (Figure 4.1 - 1c).

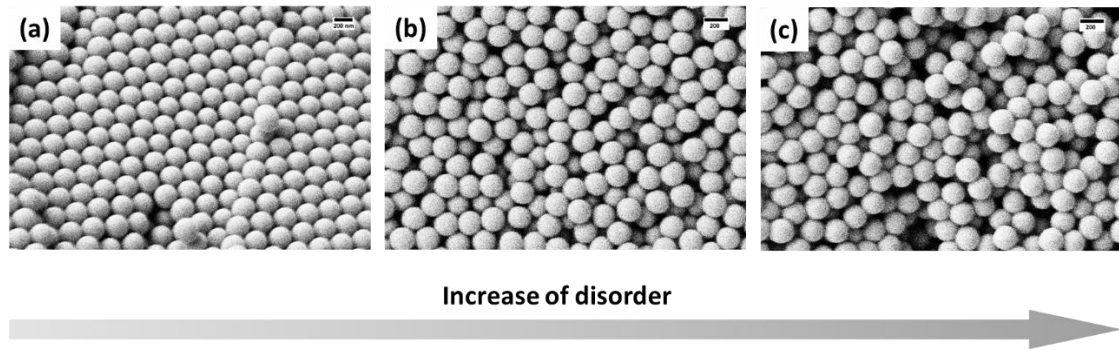


**Figure 4.1 - 1. SEM images of colloidal packing obtained by drying colloidal dispersion with different electrolyte concentration (a) no  $\text{CaCl}_2$ ; (b) 5.3 mM  $\text{CaCl}_2$ ; (c) 10.7 mM  $\text{CaCl}_2$  under gravity. Scale bar = 200 nm.**

Therefore, a tool which can precisely correlate the amount of electrolyte to the corresponding glassy colloidal packing is highly in demand.

In this part of work,  $\text{CaCl}_2$  was mainly chosen as the electrolyte to trigger the coagulation of the colloidal dispersions. As a comparison between divalent and monovalent, the effect of adding  $\text{NaCl}$  to the colloidal dispersion was also investigated. Firstly, the conventional methods like Zeta potential measurements and interaction potential calculation based on Derjaguin-Landau-Verwey-Overbeek (DLVO) theory were used to characterize the stability of the colloidal particles. Then different techniques for determining the particle size like dynamic light scattering (DLS), analytical ultracentrifugation (AUC) and Flow Field-Flow Fractionation (AF4) were applied to detect the colloidal particle aggregation in the presence of extra electrolytes. After a thorough understanding as well as a good control of the disorder formation from the above investigations, a co-assembly method was developed in the centrifugal field to well preserve the glassy colloidal packing in a macroscopic free-standing monolith. Finally, photon time of flight measurements were conducted with the obtained photonic glasses as a proof of principle demonstrating the feasibility for further optical investigation.

#### 4.1.1 Conventional methods to characterize the colloidal stability

Colloidal dispersions are all thermodynamically unstable. Colloidal stability means stability against agglomeration which can be counteracted by strong electrostatic repulsion.

The ionic environment in the vicinity of a charged colloid is visualized by the double layer model. The positive ions (often called counter-ions) in solution are attracted by the negative colloid and form a firmly attached layer around the surface of the colloid, which is known as the Stern layer. More positive ions which are still attracted by the negative colloid are however repelled by the Stern layer and other positive ions which are also approaching the negative colloid. This results in a dynamic equilibrium and the formation of a diffuse layer. The Stern layer and the diffuse layer are called the double layer. The thickness of double layer depends on the type and concentration of ions in solutions (see also 2.1.2 Colloidal forces).

An electro kinetic potential is created between the surface of the colloid and any point in the mass of the suspending liquid, due to the formation of the double layer. This potential is known as the surface potential and has a potential difference in the order of millivolts. In an electric field, charged particles will move with a velocity determined by the dielectric constant, viscosity of the suspending liquid, and also the electrical potential at the boundary between the moving particles and the liquid (slipping plane). The electrical potential at the slipping plane is known as the zeta( $\xi$ ) potential which can be quantified by electrophoresis.

Zeta ( $\xi$ ) potential measurement can help to represent the electrostatic repulsion and therefore control colloidal stability. When the magnitude of the zeta potential is small, attractive forces may exceed the repulsion between adjacent particles and the particles may aggregate and flocculate.

The zeta potential measurements of the polystyrene colloidal dispersions at different concentrations of  $\text{CaCl}_2$  are shown in Figure 4.1 - 2a. It can be seen that up to a concentration of  $\text{CaCl}_2$  of 10.7 mM, the zeta potential remains greater than -40 mV which indicates that the colloidal dispersions have a relative good stability.<sup>77-78</sup> However, Figure 4.1 - 1 shows that the colloidal packing already started to lose its order at a much lower electrolyte concentration. Simply the substantial large electrostatic repulsion of colloidal particles is not able to assure ordered colloidal packing. One should also take other interactions into account.

Different from the zeta potential measurement, the DLVO theory which also considers the van der Waals interactions besides the electrostatic repulsions has been commonly used to predict the stability of colloidal systems. The particle stability is favored when the total free energy  $\Delta G > 0$  at contact. A plot of inter particle distance vs corresponding energy is known as the DLVO plot and is used to correlate with the stability of the particle dispersion. In Figure 4.1 - 2b, it can be found that there is still a high energy barrier at the  $\text{CaCl}_2$  concentration of 7.9 mM and 10.7 mM.

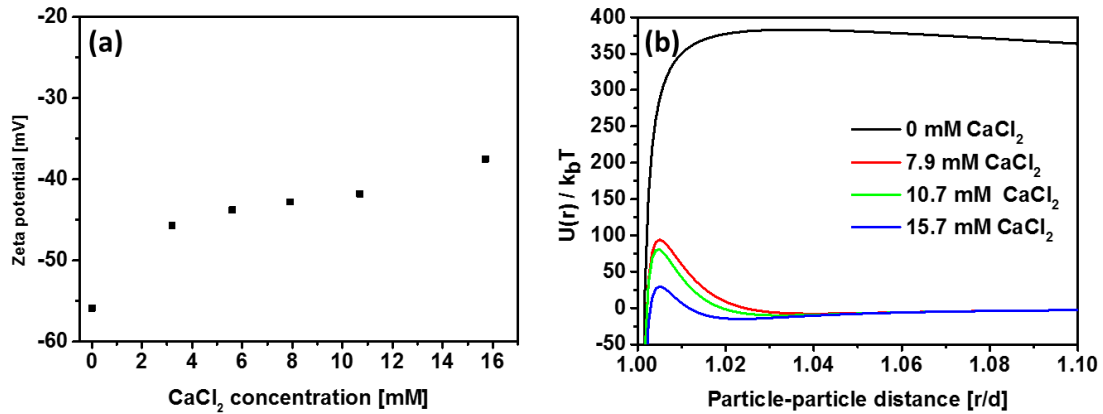


**Figure 4.1 - 2. Conventional methods to characterize the stability of nanoparticles. (a) Zeta potential of polystyrene colloidal dispersions with different concentrations of CaCl<sub>2</sub>; (b) DLVO plot: total interaction potential vs interparticle distance at different concentrations of electrolyte.**

The DLVO approach failed in a similar way as the zeta potential measurement by indicating a better stability of the colloidal dispersion than what has been found in the corresponding colloidal packing (Figure 4.1 - 1). A lot of scientific work over the past decades have been done to explain the disparity between experimental results and predications from DLVO theory and improve the DLVO theory for more accurate prediction of the colloidal stability. Some efforts in expanding the capabilities of the DLVO theory went toward the basic part of the theory while doubting that only two types of interactions in terms of electrostatic and van der Waals between colloidal particles exist. Refinements like solvation forces<sup>41</sup> and hydrodynamic retardation<sup>42</sup> have been proposed as additional forces. Some other explanations<sup>43-45</sup> for the failure of the DLVO theory lied within the framework of the electrostatic and van der Waals forces and tried to modify the mean field Poisson-Boltzmann theory<sup>46-47</sup> which has been commonly used to resolve the electrostatic potential of charged colloidal particles in the presence of dissolved ions. Another limitation of the DLVO theory has been proposed to be related to the nature of colloidal particles. The heterogeneity of surface charge has been provoked by Kihira *et al.*<sup>48</sup> They showed that the discrepancies in the coagulation rates can be perfectly bridged if the discreteness of the surface charge is taken into consideration. But the necessary heterogeneity was very large.

While the interactions between colloidal particles can influence the colloidal packing, particle size distribution is also an important factor in determining the assembled structures. Therefore, in the next section several well-established methods will be used to determine the

size distribution of nanoparticles and find out the relationship between the ionic strength and the colloidal packing structure.

#### 4.1.2 Determining size of colloidal particles to detect the nanoparticle aggregation

Dynamic light scattering (DLS) is one of the most widespread methods for sizing nanoparticles. DLS was adopted here trying to correlate the amount of electrolyte in the colloidal dispersion with the resulting colloidal packing. The results from DLS measurements are shown in Figure 4.1 - 3. There is a small fluctuation in particle sizes when small amounts of  $\text{CaCl}_2$  were present. The average size increases at 10.7 mM indicating aggregation although Figure 4.1 - 1 shows disorder already at lower electrolyte concentrations. Size distributions from DLS alone are nontrivial to obtain without prior knowledge of whether aggregation is occurring.<sup>79</sup>

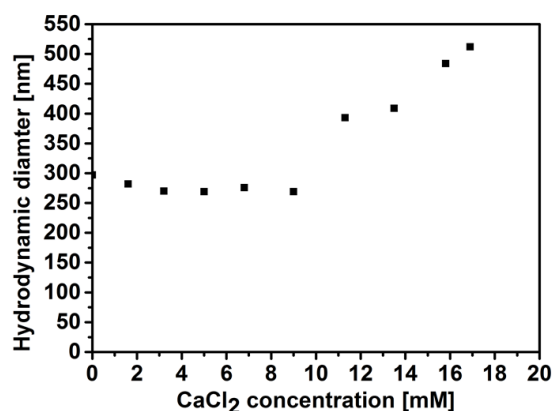


**Figure 4.1 - 3. The hydrodynamic diameter of the polystyrene colloidal particles measured by dynamic light scattering at different electrolyte concentrations.**

In contrast, analytical Ultracentrifugation (AUC) is very well suited to detect low levels of aggregation, since it is able to provide an extremely high resolution up to Angstrom resolved particle size distributions, as illustrated in the theoretical part. Figure 4.1 - 4a shows the  $g^*(s)$  analysis from interference data.<sup>80</sup> Distinct peaks were observed next to the primary one when  $\text{CaCl}_2$  was added to the colloidal dispersions. But when the electrolyte was changed to monovalent  $\text{NaCl}$ , only a broadening effect was observed in the sedimentation coefficient distribution (Figure 4.1 - 4c). These distinct peaks which showed up in Figure 4.1 - 4a might belong to different oligomers of the colloidal particles.

It is relatively straightforward to convert a sedimentation coefficient distribution into a particle size distribution (Figure 4.1 - 4b and d). The detailed derivation can be found in the theoretical part 2.2.2. The relationship between sedimentation coefficient and particle size is presented in Equation 2 - 32. In brief, it is necessary to know the density of the sedimenting particle and the density of the solvent in order to obtain the particle distribution from the sedimentation coefficient distribution.

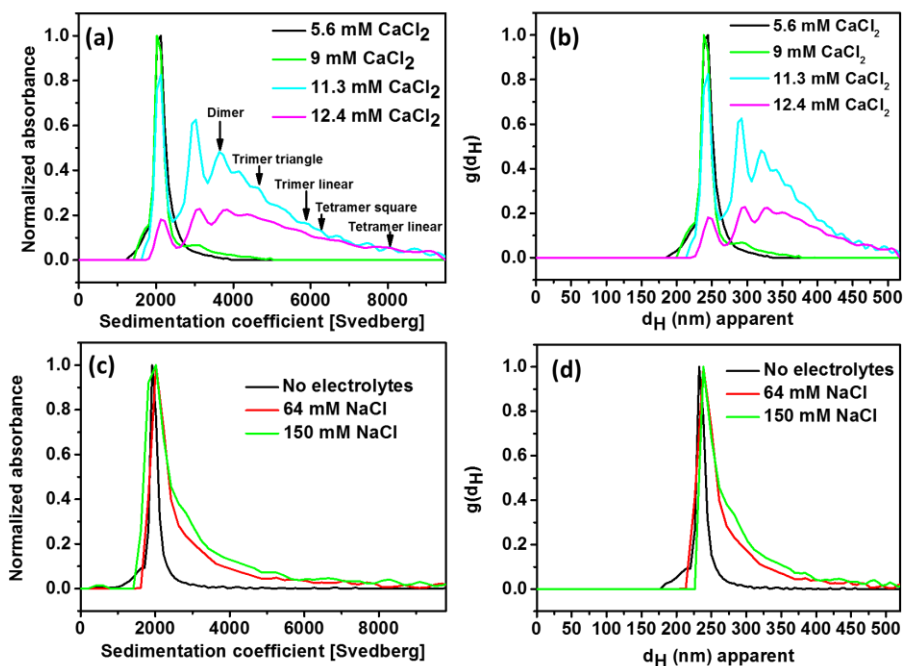


**Figure 4.1 - 4. (a)** The sedimentation coefficients of the polystyrene colloidal particles measured by analytical ultracentrifugation (AUC) with different  $\text{CaCl}_2$  concentrations; **(b)** Particle size distribution converted from sedimentation coefficient distribution in (a); **(c)** The sedimentation coefficients of the polystyrene colloidal particles measured by analytical ultracentrifugation (AUC) with different NaCl concentrations; **(d)** Particle size distribution converted from sedimentation coefficient distribution in (c).

It should be noted that dilution dynamics were found when the additional electrolyte is changed to NaCl. If the sample was measured in AUC directly after mixing NaCl and the PS dispersion, one can by chance observe multi-steps in the sedimentation curves (as shown in Figure 4.1 - 5). But it was not reproducible. And the multi-step would not show up if equilibrium time was allowed. The screening effect of the electric double layer caused by adding NaCl as electrolyte is probably reversible, when the mixture was diluted to the concentration which is suitable for AUC measurements.

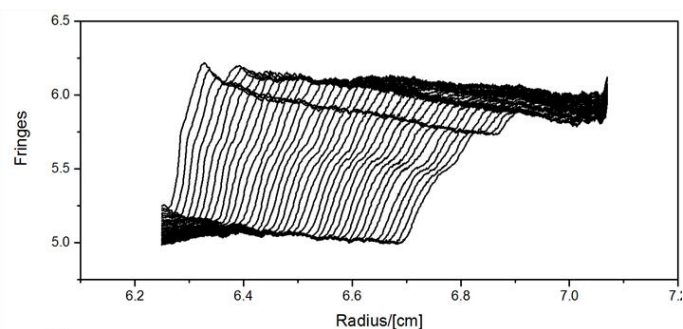


**Figure 4.1 - 5. Multi-steps in the sedimentation curves can be observed by chance if the sample was measured in AUC directly after mixing NaCl and the PS dispersion.**

What has also been carried out is the turbidity measurement in an analytical ultracentrifugation which is equipped with turbidity optics. This kind of AUC is rather simple but not commercially available. In brief, a turbidity measurement is comparable to an absorption measurement. One fixed radial position is selected at the middle of the analytical cell. Turbidity data is obtained by a light transmittance  $I = f(t)$  function.<sup>81</sup> In industry, turbidity measurements are very often performed as dispersions mostly have a broad particle size distribution. Here in our case, the particle size distribution is of central interest as the scale of repulsion force has been excluded to be responsible for the unordered colloidal packing. Figure 4.1 - 6 shows the turbidity measurements for the PS colloidal dispersions with different amount of  $\text{CaCl}_2$ . Multi-steps can be found which indicates that there is more than one particle species in the dispersions. There is no quantitative evaluation possible as no Mie correction is available. But the turbidity measurements at least give us a qualitative results showing consistent findings with Figure 4.1 - 4.

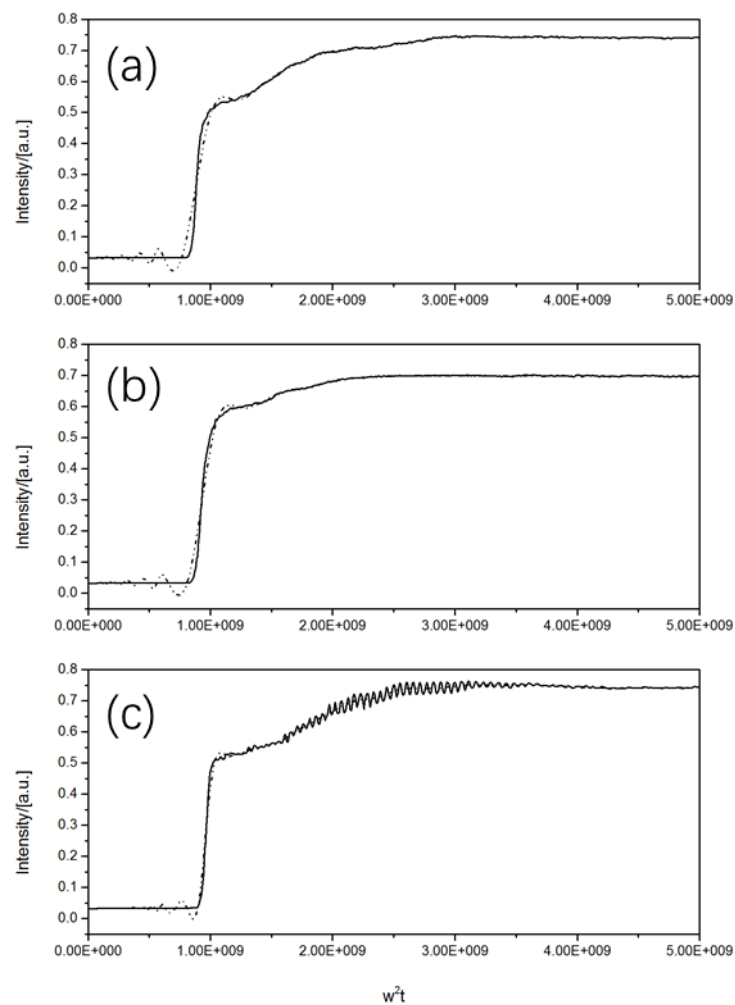


**Figure 4.1 - 6. Turbidity measurements for the PS colloidal dispersions with different amount of  $\text{CaCl}_2$ : (a) 9 mM; (b) 11.3 mM; (c) 12.4 mM.**

By combining the hydrodynamic properties of oligomer structures,<sup>82</sup> particle size distribution (Equation 2 - 32) and the Stokes-Einstein equation (Equation 2 - 26), the sedimentation coefficients of the oligomers are calculated from the sedimentation coefficient of the monomer (2088 Svedberg) and are shown in Table 4.1- 1.

**Table 4.1- 1. Sedimentation coefficient and hydrodynamic diameter of different polystyrene particle oligomers calculated from the sedimentation coefficient of the monomer.**

	Dimer	Trimer (triangle)	Trimer (linear)	Tetramer (square)	Tetramer (tetrahedron)	Tetramer (linear)
Sedimentation coefficient / [Svedberg]	3712	4793	5800	6207	5611	8028
Hydrodynamic diameter / [nm]	323	367	404	418	397	475

In Figure 4.1 - 1a, at a  $\text{CaCl}_2$  concentration of 9 mM, one species with the sedimentation coefficient of 3030 Svedberg was observed, which cannot be assigned to any of the oligomers in Table 4.1- 1. The species at 3030 Svedberg is more pronounced and a lot more distinct peaks including dimer, trimer triangle, trimer linear, tetramer square, tetramer linear were observed when the concentration of  $\text{CaCl}_2$  was increased to 11.3 mM (Figure 4.1 - 4a blue curve). With a concentration of 12.4 mM, a weakening of the primary peak occurred, while the other oligomer species cannot be very well distinguished. For easier comparison with other results, the sedimentation coefficients in Figure 4.1 - 4a and Table 4.1- 1 were also converted to particle size (Figure 4.1 - 4b) via Equation 2 - 32. By combining the DLS and AUC analysis, it can be deduced that the polystyrene colloidal system experienced a transformation to a broad aggregate distribution when the concentration of  $\text{CaCl}_2$  exceeded a certain threshold around 11 mM.

Unlike AUC, Flow Field-Flow Fractionation (AF4) chromatographic separation technique that is used to fractionate samples due to their diffusion coefficients, which is independent from the density of samples. The volume of a dimer is two times that of a monomer. Therefore, the hydrodynamic radius of a dimer is about 1.26 times that of the monomer radius.

From AF4 investigations (Figure 4.1 - 7), both the monomer and the dimer can be identified. There is no other species between monomer and dimer. This means that the 3030 Svedberg species observed in AUC must be a monomer species with a higher density or a dimer with a lower density. Since the lattices are charge stabilized with sulfonate surface groups, binding of  $\text{Ca}^{2+}$  will occur, which not only leads to the observed oligomerization but also to a density increase. This is the most likely explanation for the 3030 Svedberg species. Since it is relatively defined, this species is suspected to result from charge reversal by complete  $\text{Ca}^{2+}$  binding. If this species is assumed to be a monomer and back calculated using Equation 2 - 32, a density of 1.081 g/ml can be found. Its higher density (polystyrene 1.054 g/ml) supports this view as well as the fact that this species only becomes visible at higher  $\text{Ca}^{2+}$  concentrations starting at 9 mM.

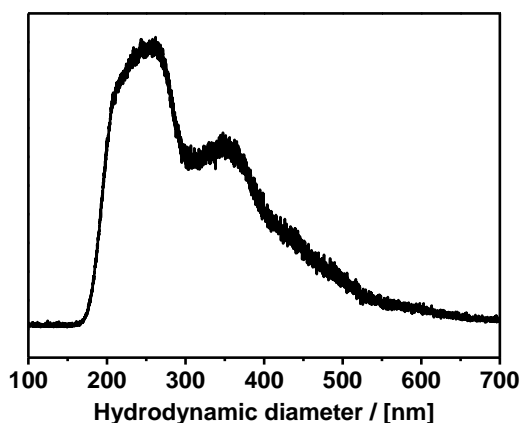


**Figure 4.1 - 7. Flow Field-Flow Fractionation (AF4) investigation of the sample with 11.3 mM  $\text{CaCl}_2$ .**

In addition, transmission electron microscopy (TEM) was adopted. Figure 4.1 - 8 is the TEM image acquired from drying polystyrene colloidal dispersion with 5.6 mM  $\text{CaCl}_2$ . Initially the aim of doing TEM characterization was to see if distorted shapes or oligomers can be found. The particles which have been observed with TEM did not show any distorted shapes. But most particles were touching each other at the edges due to the drying effect. Therefore, TEM is not a clever way to characterize oligomers from dispersions. Liquid TEM or Cryo TEM would do much better job.

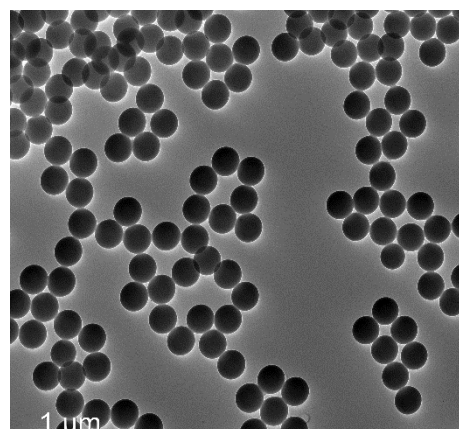


**Figure 4.1 - 8. TEM image acquired from drying polystyrene colloidal dispersion with 5.6 mM  $\text{CaCl}_2$ .**

In order to approach a macroscopic material with glassy nanostructure, which could be suitable for further optical investigation (e.g. characterization of its resonant behavior<sup>74</sup>), the centrifugal force<sup>83</sup> was applied here as it is easy and efficient to trigger colloidal assembly. The sediment at the bottom of the centrifuge tube was dried and investigated via SEM.

One can easily see from Figure 4.1 - 9 that the colloidal packing exhibits a two-layer structure when the amount of  $\text{CaCl}_2$  is relatively far below the threshold (about 11 mM obtained from DLS measurement shown in Figure 4.1 - 3). At the top part, some crystalline domains were still present while a random structure was observed at the bottom. This two layer structure could be better recognized at lower magnification (Figure 4.1 - 9b).

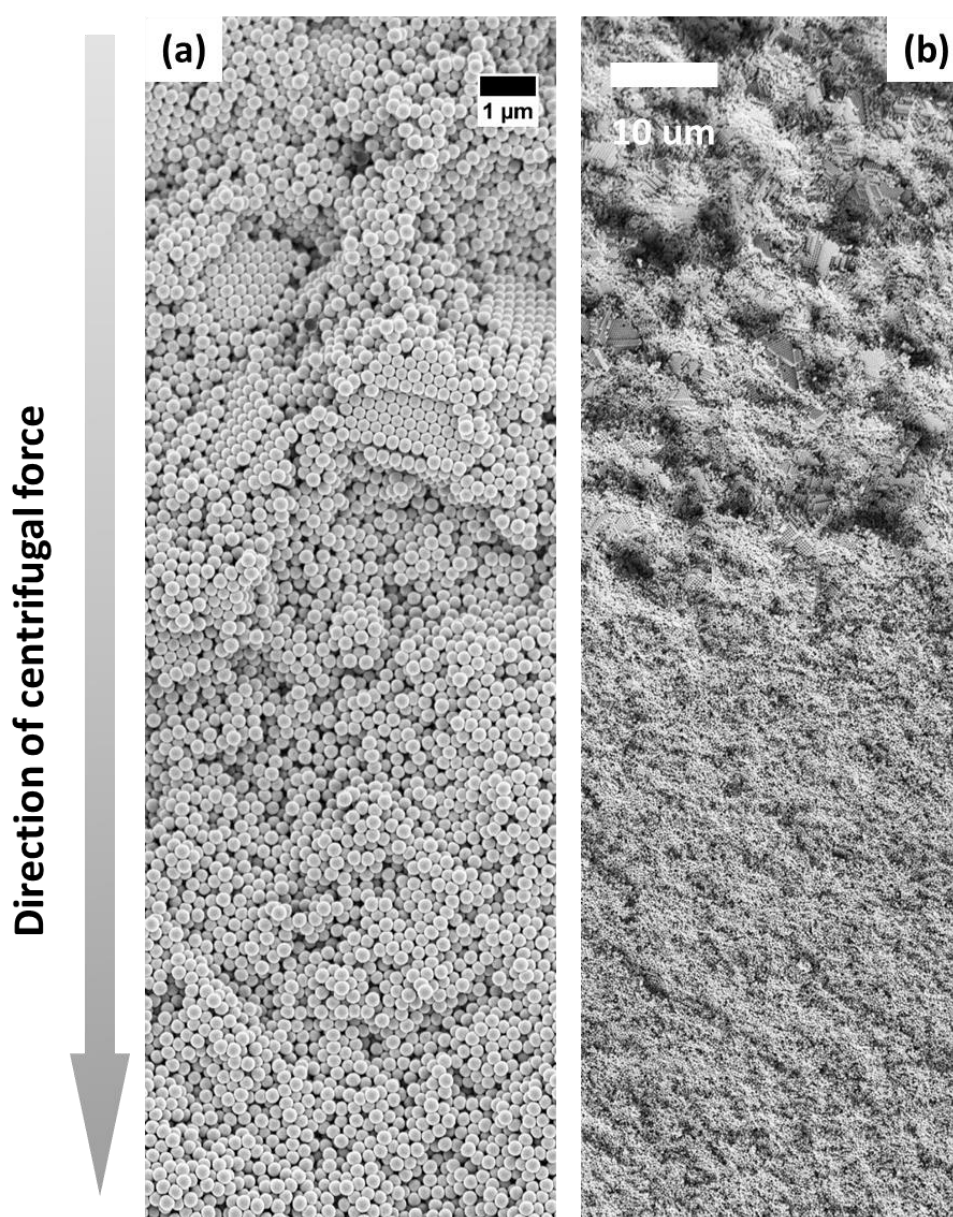
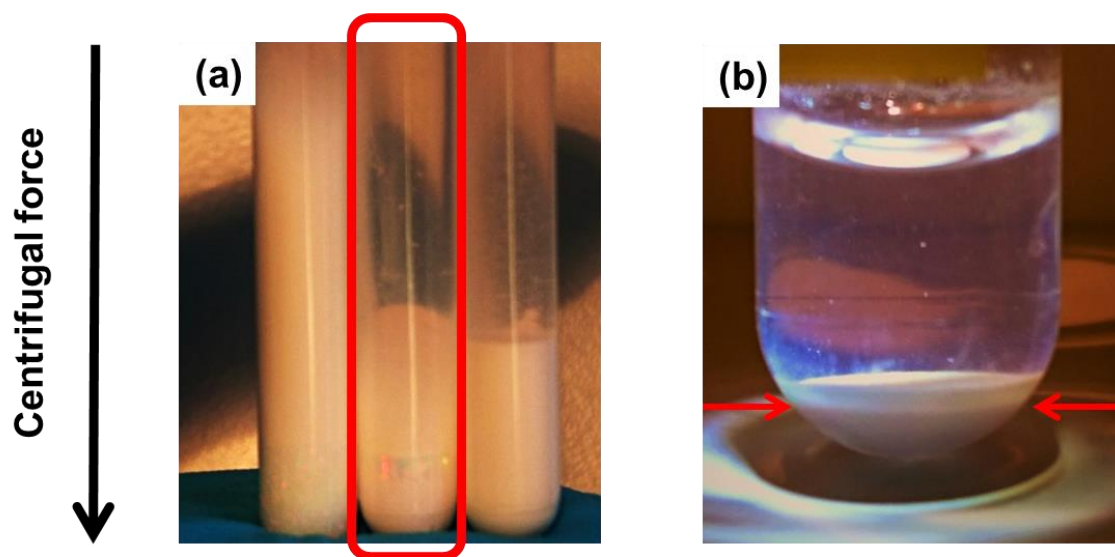


Figure 4.1 - 9. SEM images in high (a) and low (b) magnification of colloidal glassy nanostructure prepared in centrifugal field in presence of 5.3 mM  $\text{CaCl}_2$ .

Reflecting the AUC analysis in Figure 4.1 - 4a, at the chosen  $\text{Ca}^{2+}$  concentration of 5.3 mM, the observed structure was build up by monomer nanoparticles, and dense monomer nanoparticles (the heavier unknown species binding with  $\text{Ca}^{2+}$ ) which however already have a tendency to aggregate. This becomes especially evident at the higher particle concentrations near the bottom of the centrifuge tube, where the particles are forced into the primary minimum in the DLVO curve before they are able to form an ordered structure which they would do in absence of salt. Nevertheless, at the lower particle concentrations at the top of the tube, still ordered domains can be formed (Figure 4.1 - 9).

Indeed, the two layer structure in Figure 4.1 - 9 can already be observed with naked eyes when checking the centrifuge tube right after centrifugation. The tube in the middle of Figure 4.1 - 10(a) as well as Figure 4.1 - 10(b) were prepared in presence of 5.3 mM  $\text{CaCl}_2$ . It can be seen that two layers appeared independently from the type of the centrifuge tube. Crystalline color could even be observed in upper part of the middle tube in Figure 4.1 - 10(a), which corresponds very well to the SEM characterization.



**Figure 4.1 - 10. Photograph of the centrifuge tubes with colloidal polystyrene particle sediment. (a) 600 ul centrifuge tubes with the middle tube having 5.3 mM  $\text{CaCl}_2$  (b) 5 ml centrifuge tube with 5.3 mM  $\text{CaCl}_2$ .**

To take the advantage of the macroscopic heterogeneity to understand the polystyrene colloidal dispersions, the centrifuge tube was taken out of the centrifugal field and put in liquid nitrogen which froze the sample immediately. The boundary of the two layers was still possible to be recognized after the sample was frozen. Then the centrifuge tube was quickly cut along this boundary before the sample was melting. The upper part and the bottom part were

redispersed in MiliQ water respectively, and followed by zeta potential and DLS measurements. The motivation to perform zeta potential and DLS measurements was to find out whether the previous results (Figure 4.1 - 2a and Figure 4.1 - 3) are averaged values.

After the measurements, it turned out that there was no significant difference between the two batches of samples (upper and lower parts separated by freezing in liquid nitrogen). Therefore, from the unchanged zeta potential, it can be concluded that the unordered packing appeared at the bottom part of the sample not due to the decreased repulsion forces; from the unchanged DLS results, it became much clearer that it is the binding of  $\text{Ca}^{2+}$  ions which causes the unordered packing at the bottom layer, instead of the increasing particle size polydispersity.

Furthermore, if the amount of  $\text{CaCl}_2$  is slightly increased, more of the dense monomer nanoparticles should be formed. Thus, more glassy domains were observed in Figure 4.1 - 11. The SEM images of colloidal packing prepared at 7.2 mM (Figure 4.1 - 11a) and 10.1 mM (Figure 4.1 - 11b)  $\text{CaCl}_2$  which confirmed this transition. It can be found that the glassy domains occupied most of the sample at 7.2 mM  $\text{CaCl}_2$  while still some tiny crystalline parts were present at the top of the sample. But when the concentration of  $\text{CaCl}_2$  was increased to 10.1 mM, crystalline domains can be hardly observed.

When the amount of  $\text{CaCl}_2$  exceeded the threshold, not only the two-layer structure disappeared and but the whole structure shown in Figure 4.1 - 12 exhibited a random packing with a lot of empty voids. This might be caused by the different oligomers formed in presence of high  $\text{CaCl}_2$  concentration. Therefore, it can be concluded that a random close-packed colloidal packing could be achieved by adding  $\text{CaCl}_2$  to a concentration near but not exceeding the threshold concentration.

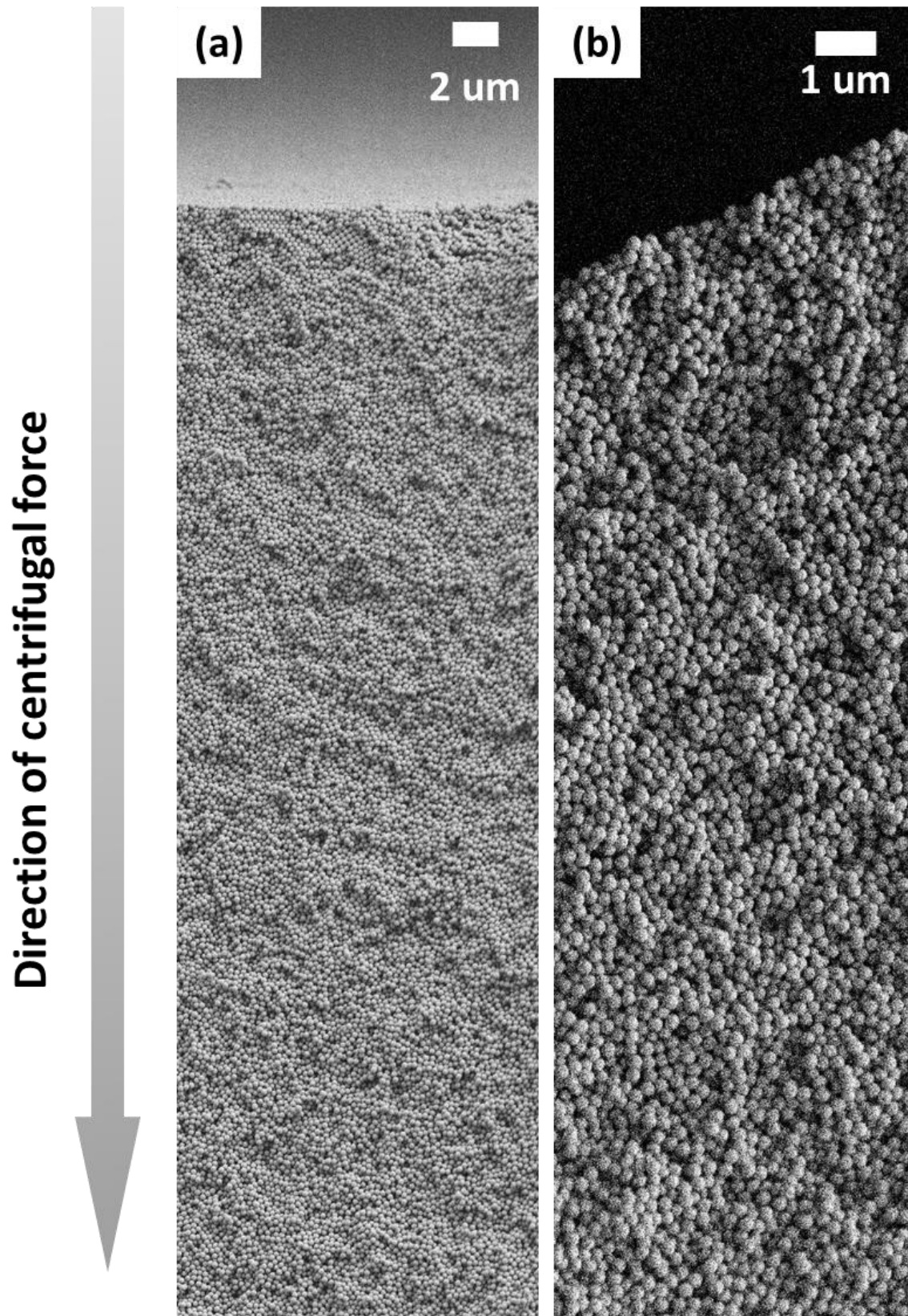
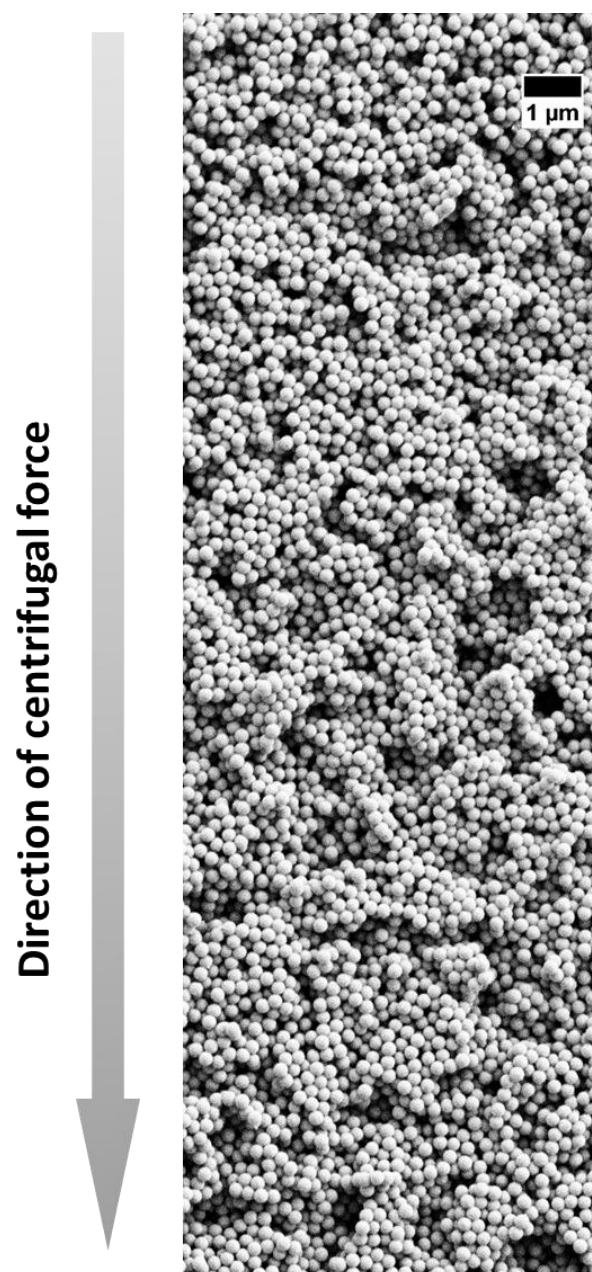


Figure 4.1 - 11. SEM images of colloidal glassy nanostructure prepared in centrifugal field in presence of (a) 7.2mM and (b) 10.1 mM  $\text{CaCl}_2$ .



**Figure 4.1 - 12. SEM images of colloidal glassy nanostructure prepared in centrifugal field in presence of 13.2 mM  $\text{CaCl}_2$ .**

The next very natural goal is to find out a way to quantitatively describe the structural order and disorder within different samples. But this is not an easy task as it seems to be. While the filling fraction or the volume fraction of spheres is a common parameter to describe different crystalline packing structures, the filling fraction of spheres is very difficult to obtain for unordered packing structures. The theoretical value for the volume fraction of a random close packing is approximate 0.64.<sup>84</sup> For specific experimental samples, the volume fraction can be obtained by measuring the total mass and volume of the samples.<sup>73</sup> A prerequisite for this method is that the sample should have a very well defined macroscopic shape. Still large error

bars cannot be avoided due to the volume estimations. In the case of Figure 4.1 - 9, Figure 4.1 - 11 and Figure 4.1 - 12, the macroscopic samples are very fragile and easily broken into undefined shapes. Therefore, it is nearly impossible to obtain the filling fraction of the three different samples.

#### 4.1.3 Free-standing photonic glasses prepared via co-assembly method

Exceeding the threshold leads to holes (Figure 4.1 - 12) and thus to lower filling fraction. This might affect the light transport (weaker scattering) and lead to optical shortcuts in the macroscopic sample. The quality of the macroscopic samples can be characterized in photon time of flight experiments. A very short laser pulse (250 fs) is sent on the sample and a time resolved photodetector measures in transmission how long the photons did travel through the sample. If no holes are present, the photons transport through the sample follows a diffusion law. The time of flight distribution of a purely diffusive sample is known theoretically and fits the experiments very well.<sup>85</sup> If holes are present in the sample, the photons entering these holes are much faster (they are not scattered until they exit the hole) and the overall transport through the sample is affected: the time of flight distribution does not follow a diffusion law anymore, some photons leave the sample earlier than expected. This is why holes in such samples are called optical shortcuts. To perform such measurements, as well as to carry out all other optical measurements, free standing materials with a proper size (1 mm to 1 cm) are needed. However, the colloidal assembly structures are in general quite fragile. Free standing macroscopic materials are highly in demand to perform the time of flight measurements.



**Figure 4.1 - 13.** Image of centrifuge tube (Ultra-Clear™ 5\*41 mm) and polyacrylamide hydrogel prepared inside the centrifuge tube.

In order to preserve the very fragile colloidal assembly structures, a co-assembly method was introduced. A hydrophilic monomer, in the present case acrylamide, was added into the colloidal dispersion. The co-assembled structures were polymerized after centrifugation by addition of ammonium persulfate as the initiator. The polystyrene colloidal spheres were trapped in the hydrogel. The robust hydrogel (see Figure 4.1 - 13) can be easily taken out of the centrifuge tube and cut into the desired shape. The images of the monolithic samples can be found in Figure 4.1 - 14a. The samples are in centimeter scale, therefore big enough to perform optical measurements. In Figure 4.1 - 14b and Figure 4.1 - 14c, it can be seen that the amount of polyacrylamide between the polystyrene spheres differs. The high concentration of  $\text{CaCl}_2$  caused the formation of different oligomers and created big volume fractions of voids (Figure 4.1 - 14). Therefore, more acrylamide monomers accumulated in between the polystyrene spheres and formed a thicker network after the polymerization.

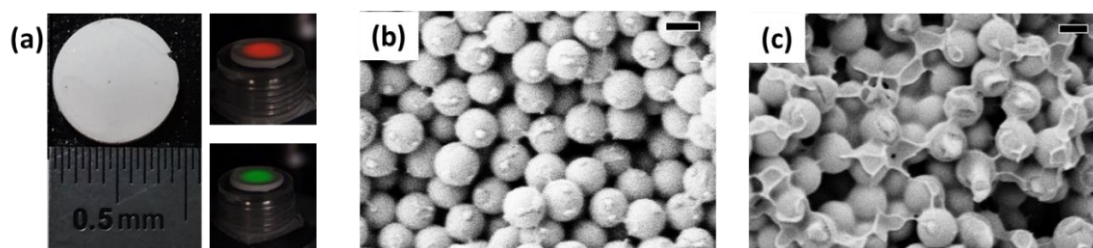


**Figure 4.1 - 14. Polystyrene colloidal structures trapped by polyacrylamide hydrogel. (a) Images of the monolithic samples; (b) glassy structure prepared by adding low amount of  $\text{CaCl}_2$  (5.3 mM); (c) glassy structure prepared by adding high amount of  $\text{CaCl}_2$  (16 mM). Scale bar = 200 nm.**

The amount of monomer influences the light transport behavior of such samples. High amounts of monomers, and thus dense networks “connect” the particles optically and lower the scattering strength. The time of flight measurements measure whether there are some big holes in the samples, i.e. if they are or not homogeneous. The signature of a big hole in the sample is a peak early in the time of flight measurements: photons traveling through this hole come faster out of the sample. In Figure 4.1 - 14, the photon time of flight distribution in a purely diffusive sample (e.g. the one of Figure 4.1 - 14b) is shown in black. It can be easily distinguished from the sample of Figure 4.1 - 14c which has optical shortcuts (the first peak from left-hand side of the red curve). They emerge as the early peak seen in the red curve. The blue curve shows the time of flight of photons through a sample with at least one big optical shortcut (for example a crack in the sample): almost all photons went through it and exit the sample very fast. The slope of the intermediate time in the time of flight tells us something about the absorption of the light in the sample. It is irrelevant to determine whether there is a shortcut or not. The absorption is

different from samples to samples, therefore is the slope difference between the black and the red curve.

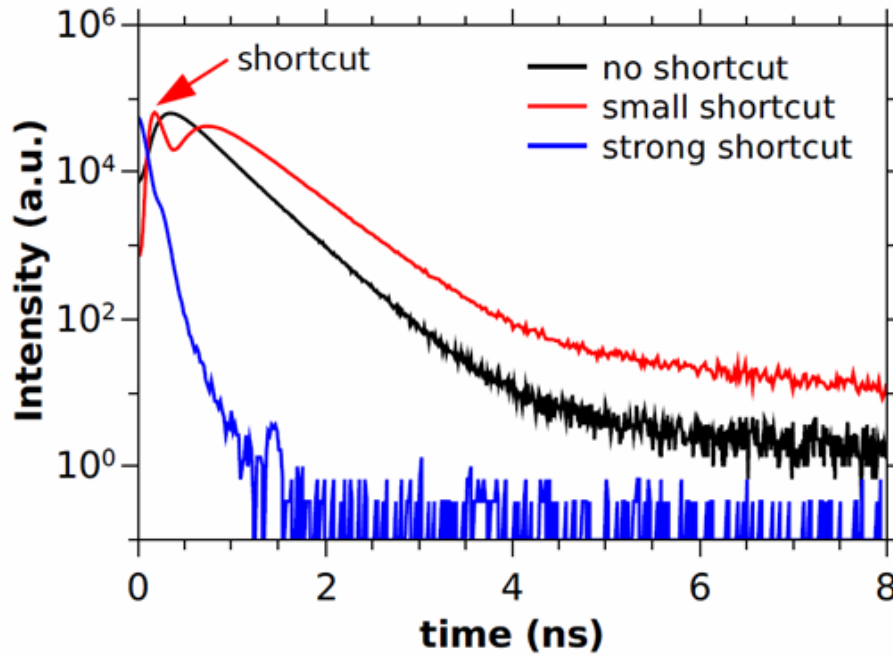


Figure 4.1 - 15. Photon time of flight measurements distinguishing samples with some big optical shortcuts (blue curve: the photons go out of the sample very early), some smaller optical shortcuts (small early peak in the red curve) and without any optical shortcut (black curve: all the photons behave diffusively).<sup>85</sup>

## 4.2 Assembly of binary colloidal system between chaos and order

Section 4.1 has very well demonstrated the great power of analytical ultracentrifugation (AUC) in differentiating monomer from oligomer colloidal particles, as well as the convenience of centrifugal field as a compaction tool for materials fabrication. If multinary colloidal systems are intentionally created and put into centrifugal field, fractionation as the most significant feature of a centrifugal field would play a central role in the colloidal assembly.

A binary colloidal system is a good model system to study the ionic crystal which is also composed of two spheres (atoms). The complexity of a binary colloidal system is not only increased by a large number of possible variations of colloidal particles themselves like ratio of two particle sizes<sup>86</sup> and degree of charging,<sup>87</sup> but also the adopted driving force for colloidal compaction. Over the past few years, several methods like layer-by-layer growth,<sup>88</sup> vertical lifting<sup>86, 89</sup> and contact printing<sup>90</sup> have been developed to fabricate ordered binary colloidal structures. Binary structures of the NaCl, CsCl, NiAs, Cu<sub>3</sub>Au, MgZn<sub>2</sub> type and others could be fabricated from nearly spherical building units.<sup>28, 91-93</sup> However, new techniques have been called for manipulating binary colloidal assembly.

In addition, segregation of granular matter has been a subject of extensive research for a long time from both theoretical<sup>94-96</sup> and experimental<sup>96-98</sup> aspects, due to the puzzling Brazil nut effect<sup>99-100</sup> meaning that larger species in a jar of mixed nuts rise to the top. As granular matter in nanoscale, charged binary colloidal suspension has also been predicted to have an analog of “Brazil nut” problem upon sedimenting, namely colloidal Brazil nut effect.<sup>101</sup>

Initially, we came to a naive idea to make use of the analytical power of AUC in the assembly of multinary colloidal systems: firstly, using AUC to obtain the characteristics of the multinary systems, e.g. sedimentation coefficient, diffusion coefficient, then simulating the concentration distribution in the preparative centrifuge tube, correlating the concentration distribution of the solute particles with the assembled nanostructures prepared on a preparative scale, eventually predicting the possible nanostructures.

As introduced in the theoretical background part 2.1.4, when the sedimentation equilibrium is reached, the concentration distribution of the solute will stay invariant with time. For different solute particles, at equilibrium we would obtain different concentration distribution profiles from AUC measurement. If the different solute particles are of the same materials, larger species will selectively distribute towards the cell bottom, while the smaller

ones will dominate the distribution at the top of the cell. The concentration distributions can simply be added (Figure 4.2 - 1) when the different solute particles are non-interacting species,.

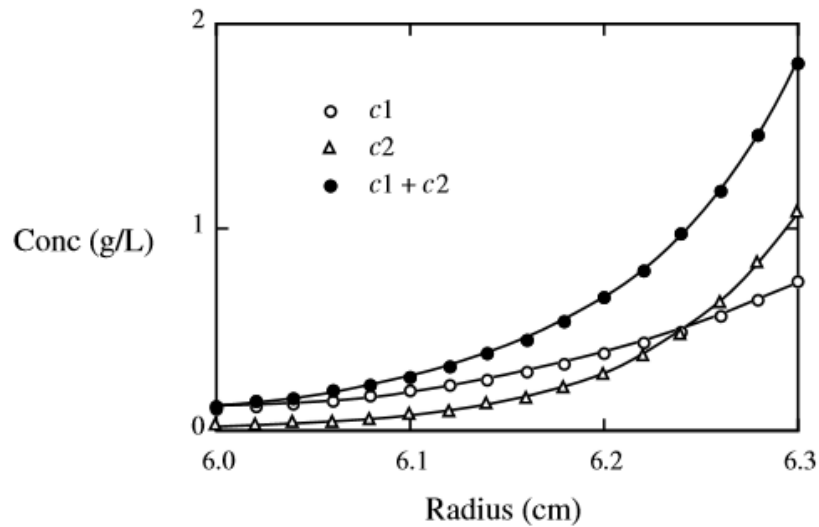


**Figure 4.2 - 1.** Sedimentation equilibrium distribution of two different solutes. Species c1 has a smaller molecular weight than c2.

The software of Sedfit is mostly used for the analysis of analytical ultracentrifugation data, written at the National Institutes of Health and distributed without charge for research use. Sedfit also has a tool to generate sedimentation profiles. This 'Generate' tool allows to simulate the sedimentation process and generate data files formatted like Beckman Optima XL-A. Therefore, when all the parameters of a preparative centrifugal field are given to Sedfit, e.g. rotor radius, the position of the top and bottom of the centrifuge tube, centrifuge speed, temperature, the evolution of concentration distribution as well as the equilibrium concentration distribution of solute particles can be obtained.

However, in practice, the above strategy met unexpected difficulty. The equilibrium can be achieved for solute particles with limited molecular weight, density, size. Although the machine Optima XL-A enables low centrifuge speed down to 1000 rpm, this speed is still too fast for the polystyrene colloidal particles (with diameter in the range of a few hundred nanometer) we would investigate.

Nevertheless, the absolute latex concentration is believed to have a significant impact on the structure of binary colloidal assembly obtained after centrifugation. My master thesis is a pioneer work to study the effect of centrifugal force on the binary colloidal systems composed of polystyrene latex spheres with different sizes. Binary domains with long range order could not be found with high latex concentration. When the latex concentration decreased, ordered

binary structures of NaCl and AlB<sub>2</sub> types were found during the investigation. However, there is a lack of overall control over the binary structures obtained by centrifugal force. The mechanism of the formation of ordered structures or unordered structures remains unclear.

In the current section, an overall control of binary colloidal systems (negatively charged polystyrene latex spheres: PS1 with diameter of  $d_{PS1} = 150$  nm, PS2 with diameter of  $d_{PS2} = 300$  nm) in the preparative centrifuge is achieved with the characterization of the binary colloidal systems in AUC. The mechanism how the centrifugal force leads to various binary structures is explored. At the end of this chapter, the centrifugal field is also applied to a binary system consisting of polystyrene and silica particles, to show that the applicability of the centrifugal field is not limited to polystyrene particles of two sizes, but also colloidal particles with different compositions.

#### 4.2.1 Characterization of binary colloidal system in analytical ultracentrifugation (AUC): Concentration dependency of sedimentation behavior

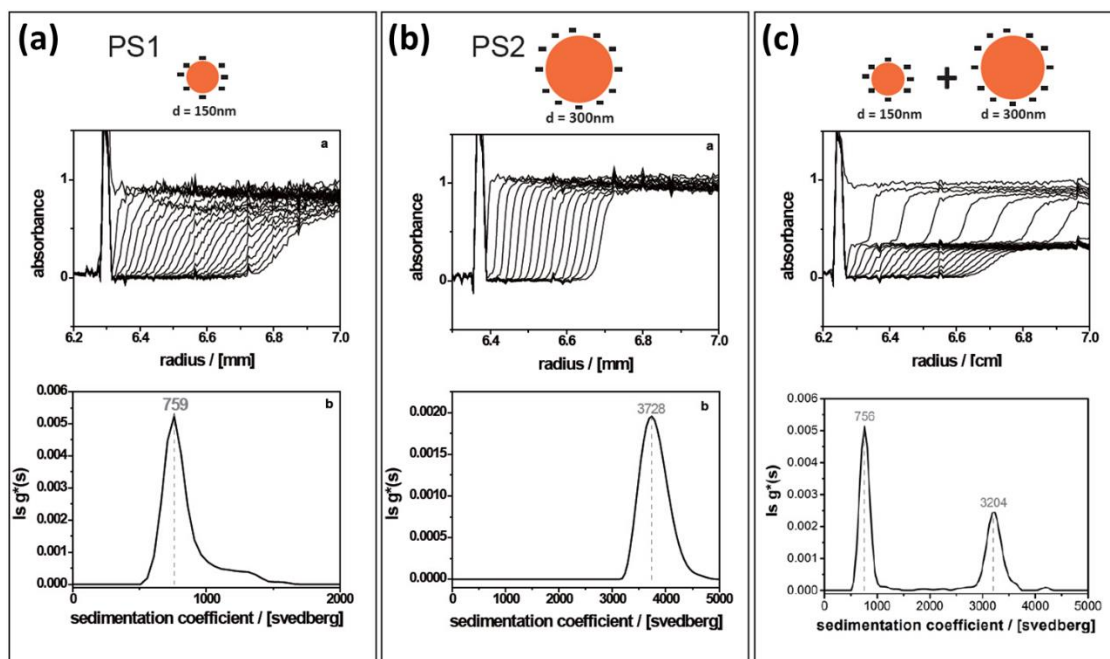


**Figure 4.2 - 2.** AUC measurements were performed for dispersions consisting of PS1, PS2, and mixture of PS1, PS2 at low particle concentrations. First row: sedimentation curves; second row: sedimentation coefficient; (a) monodisperse system at low volume fraction:  $d_{PS1} = 150$  nm, volume fraction =  $3.6 \times 10^{-5}$ ; (b) monodisperse system at low volume fraction:  $d_{PS2} = 300$  nm, volume fraction =  $2.4 \times 10^{-5}$ ; (c) binary system at low volume fraction:  $d_{PS1} = 150$  nm, volume fraction =  $3.6 \times 10^{-5}$ ;  $d_{PS2} = 300$  nm, volume fraction =  $2.4 \times 10^{-5}$ . The difference in absorbance between the more concentrated smaller particles and the larger particles is caused by Mie scattering.<sup>102</sup>

AUC measurements were performed for dispersions consisting of PS1, PS2, and mixture of PS1, PS2 at different particle concentrations. For low volume fractions (in the range of  $10^{-5}$ ), the sedimentation coefficient of polystyrene particles can be calculated directly from the AUC raw data using the  $ls-g^*(s)$  model with the software Sedfit.<sup>103</sup> Figure 4.2 - 2 shows an example AUC measurement at low particle concentration. The first and second rows are the sedimentation curves as raw data from the measurements and the sedimentation coefficients calculated from the AUC raw data.

For high volume fractions ( $>10^{-2}$ ), Lamm equation modelling (Equation 2 - 16 in section 2.1.4) does not work anymore due to the large non-ideality effects. The sedimentation coefficient of the polystyrene particles is calculated manually according to Equation 2 - 18 from the sedimentation curves. A plot of the logarithm of the radial position and the sedimenting boundary as a function of the run time integral yields a straight line with slope  $s$ . Figure 4.2 - 3 gives an example of extracting the sedimentation coefficient from a monodisperse system  $d_{PS1} = 150$  nm at high volume fraction 0.027.

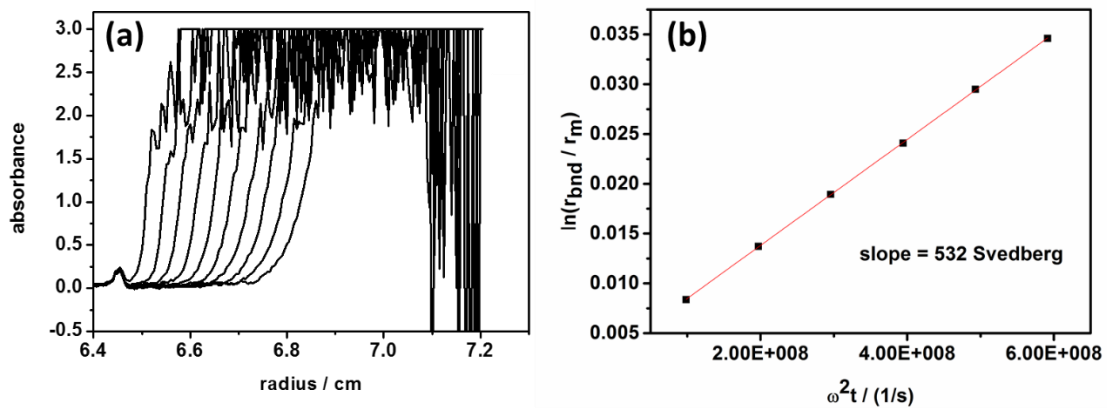


**Figure 4.2 - 3. (a) Sedimentation curves without upper plateau due to high particle concentration and (b) sedimentation coefficient of a monodisperse system at high volume fraction.  $d_{PS1} = 150$  nm, volume fraction = 0.027.**

By doing a series of AUC measurements at different particle concentrations, the total volume fraction  $\Phi$  dependency of the sedimentation coefficients can be plotted in Figure 4.2 - 4. Only the sedimentation front of the smaller and thus slower sedimenting particles can be observed for the investigated concentrated binary mixture. This should be due to the very high concentration of particles. Therefore, calculated sedimentation coefficients fit into the concentration dependence of the sedimentation coefficients of smaller particles. It can be

concluded that apart from the expected nonideality, there are no special features present in the binary systems consisting of two different sizes.<sup>104</sup>

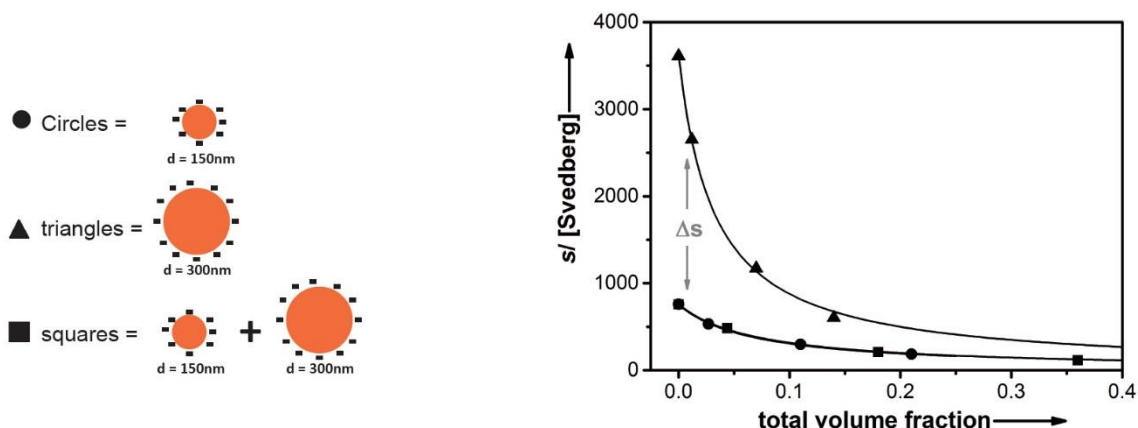


**Figure 4.2 - 4.**  $\Phi$  dependency of the sedimentation coefficients. Circles  $\cong$  monodisperse  $d_{PS1}$ , squares  $\cong$   $d_{PS1}$  in binary system  $d_{PS1} + d_{PS2}$ , triangles  $\cong$  monodisperse  $d_{PS2}$ , solid lines  $\cong$  theoretical data.

#### 4.2.2 Gaining control over a binary colloidal system in the preparative centrifuge

Although AUC is able to record the whole sedimentation process with its optical detection system, it is unfortunately limited to highly diluted sample. It is almost not possible to collect the assembled structure from a AUC cell after centrifugation and perform further microscopy investigations. Applying the sedimentation knowledge of a binary colloidal system gained from AUC to preparative centrifugation would be a clever way to solve the challenge which lies in the

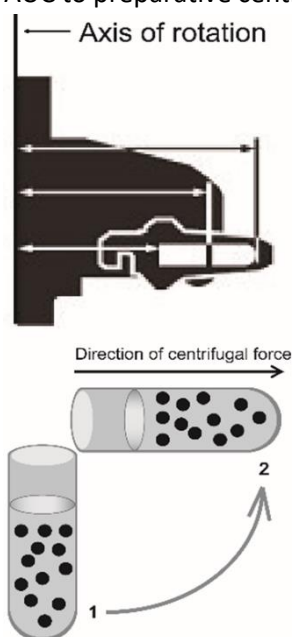


**Figure 4.2 - 5.** Scheme of a swing out rotor.

lots of variable parameters, including centrifugation force ( $F$ ), centrifugation time ( $t$ ), column length ( $L$ ), total volume fraction of particles ( $\Phi$ ) and number ratio of two particles ( $N = N_{PS1} / N_{PS2}$ ).

Here the preparative centrifuge experiments were all carried out under vacuum to assure a constant temperature. Also a swing out rotor (Figure 4.2 - 5) was used to provide a centrifugal force which is parallel to the sedimentation direction. As shown in the sedimentation curves of Figure 4.2 - 2c, there is a distance between the two sedimentation boundaries in the binary colloidal systems. This distance ( $\Delta r$ ) can be derived from Equation 2 - 18 as follows:

$$\Delta r = r_m (\exp(s_2 \omega^2 t) - \exp(s_1 \omega^2 t)) \quad \text{Equation 4.2- 1}$$

where  $r_m$  is the radius of the meniscus,  $\omega$  is the angular velocity,  $t$  is the centrifugation time,  $s_1$  and  $s_2$  are the sedimentation coefficient of PS1, PS2 respectively. From Equation 4.2- 1, it can be found that the distance between the two sedimentation boundaries  $\Delta r$  is a sum of several variables in the centrifugation process, i.e. centrifugation force ( $F$ ), centrifugation time ( $t$ ), column length ( $L$ ), total volume fraction of particles ( $\Phi$ ). The ratio  $\Delta r / L$  is one of the most important factors that determines the final separation. A subtle interplay of  $\Delta r / L$  which corresponds to  $\Delta s$  involves the variation of  $\Phi$  for a given  $N$  (not quantitatively considered in Equation 4.2- 1). A large value of  $\Delta r / L$  is a requirement for strong ( $\Delta r / L = 0.702$ ) and medium ( $\Delta r / L = 0.667$ ) separation conditions. A relatively smaller value of  $\Delta r / L$  leads to weak separation ( $\Delta r / L = 0.128$ ). Besides the ratio  $\Delta r / L$ , centrifugal force and time also determines the final separation as can be seen from Equation 4.2- 1. A smaller centrifugal force is favorable for obtaining ordered structures as  $\Delta r$  is low and therefore weak separation conditions. The appropriate centrifugation time can be calculated from Equation 2 - 18 when  $r_{\text{bnd}}$  is set as the bottom position of the centrifuge tube. Too long centrifugation time will destroy the ordered binary pattern within the medium separation since  $\Delta r$  is increasing with time (Equation 4.2- 1). Specific parameters for different separation conditions can be found in the experimental part.

Therefore, with the data in Figure 4.2 - 4 combined with the empirically chosen number ratio of two particles ( $N = N_{PS1} / N_{PS2}$ ), the control of strong and weak separation should be possible. The different types of separation found in this work are shown in Figure 4.2 - 6.

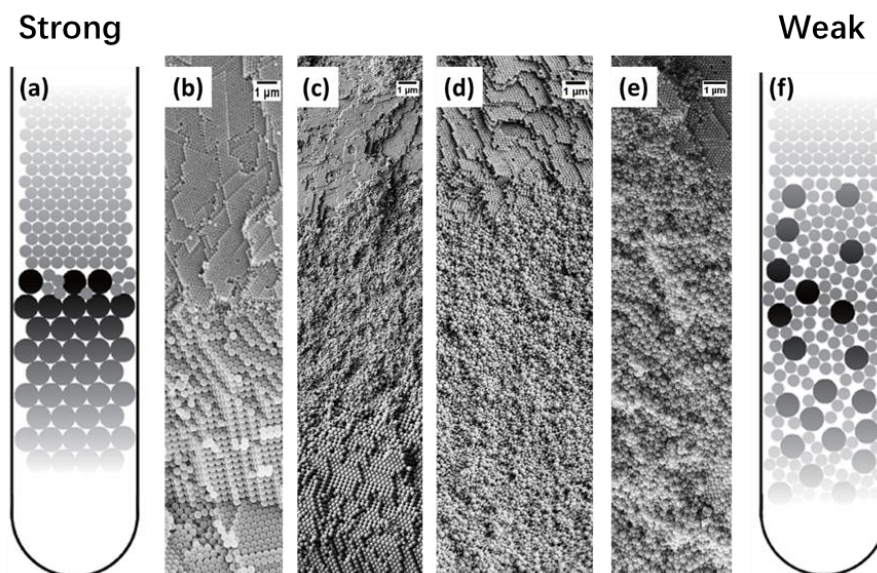


**Figure 4.2 - 6. Schemes and SEM images of different structures assembled from binary colloidal systems (PS1, PS2) via different centrifugation conditions. (a) and (b) are scheme and SEM of strong separation respectively; (c) is the SEM image of the transition part of a medium separation; (d) and (e) are SEM images of weak separation.**

When conditions for strong separation conditions are selected (Figure 4.2 - 6a,b). PS1 and PS2 formed separate domains individually, exhibiting close-packed face-centered cubic structures (see Figure 4.2 - 7). Different from the strong separation, a medium separation case with a transition zone composed of glassy binary was observed (Figure 4.2 - 6c). At the top and bottom of the centrifugation vial are densest packed zones of PS1 and PS2 respectively. When the separation is weak, only the top part of the centrifugation vial was characterized by a region consisting of purely smaller spheres PS1, which assemble into close packing (Figure 4.2 - 6d, e, f). The remaining bottom part of

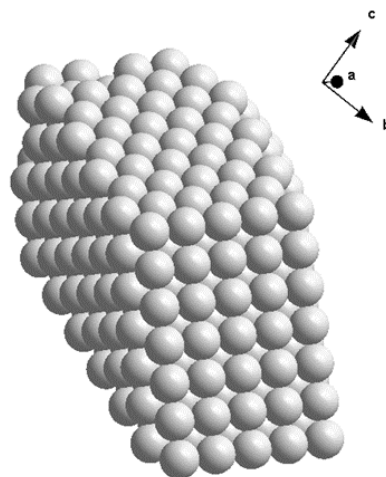


**Figure 4.2 - 7. Assignment of the close packing in Figure 4.2 - 6a,b to fcc.**

the sample is made of a mixture of PS1 and PS2. A shallow gradient regarding the relative concentration of PS1 and PS2 can be seen with a closer inspection of Figure 4.2 - 6d. Within the weak separation category, the presence of larger spheres in the matrix of the smaller spheres at the bottom part of the sample leads to a variety of binary structures. In Figure 4.2 - 6d, the incurrence of crystalline domains was prohibited which also fits to experimental and theoretical observations on binary colloidal systems made by others.<sup>105-106</sup> However, Figure 4.2 - 6e shows systems in which several binary zones possess periodic order. A summary of different PS1, PS2 concentration gradient is made in Figure 4.2 - 8.

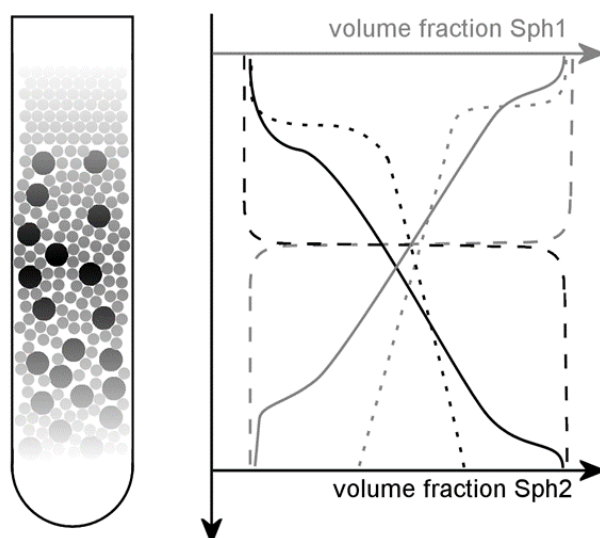


**Figure 4.2 - 8. Schematic representation of the different concentration gradients obtained due to different separation conditions. dotted lines  $\cong$  weak separation conditions; solid lines  $\cong$  medium separation conditions; dashed lines  $\cong$  strong separation conditions.**

### 4.2.3 The emergence of ordered binary structures

From the discussion in the last part, it is obvious that the centrifugal force  $F$  which directly influences the sedimentation rate, plays an important role in the sedimentation process. When sedimentation occurs very fast at high centrifugal force (e.g.  $F = 1.2 \times 10^4 g$ ;  $g =$  earth's gravitational acceleration  $9.81 \text{ m/s}^2$ ), the systems remain in the glassy state independently of  $\Delta s$  (see Figure 4.2 - 9a).

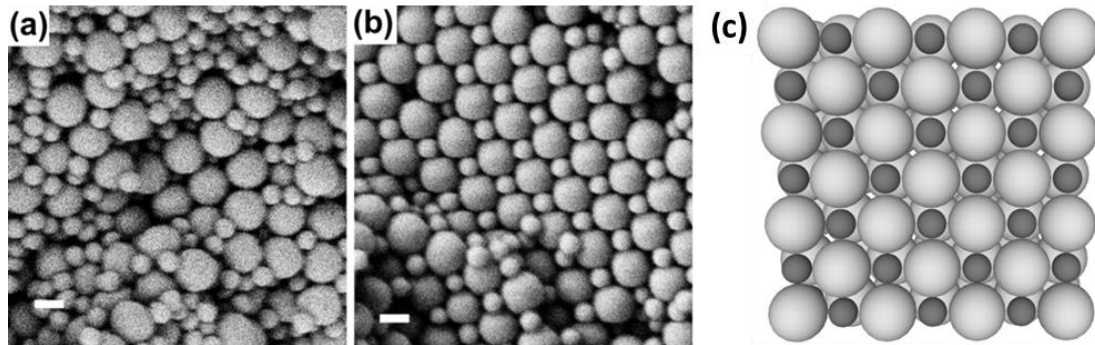


**Figure 4.2 - 9. (a) SEM micrographs of disordered binary structures obtained for large values of  $F$  and (b) ordered binary structures obtained for small values of  $F$ , Scalebars  $\cong 200 \text{ nm}$ ; (c) scheme of the NaCl structure.**

For small centrifugal force (e.g.  $F = 1.2 \times 10^2 g$ ) a significant fraction of the material exhibits the formation of a periodic (PS1)(PS2) structure shown in Figure 4.2 - 9b, consistent with the NaCl lattice (space group  $Fm\bar{3}m$ ) (see Figure 4.2 - 9c). However, to assign the crystal structures (3D information) from only one crystal plane [hkl] (2D information) is of great difficulty and often not precise, and whenever possible adjacent lattice planes should be taken into consideration. For example, NaCl and CsCl look almost identical with a square unit pattern when observed exclusively from the [100] perspective (see Figure 4.2 - 10a). However, from the side view, it can be easily distinguished that only in the NaCl structure the centers of small and large spheres are placed in-plane. For the CsCl structure, the small spheres are located below the top-layer. From closer inspection of the SEM images (Figure 4.2 - 9 and Figure 4.2 - 10b,c) it can be proven unequivocally that the rock salt structure is present here.

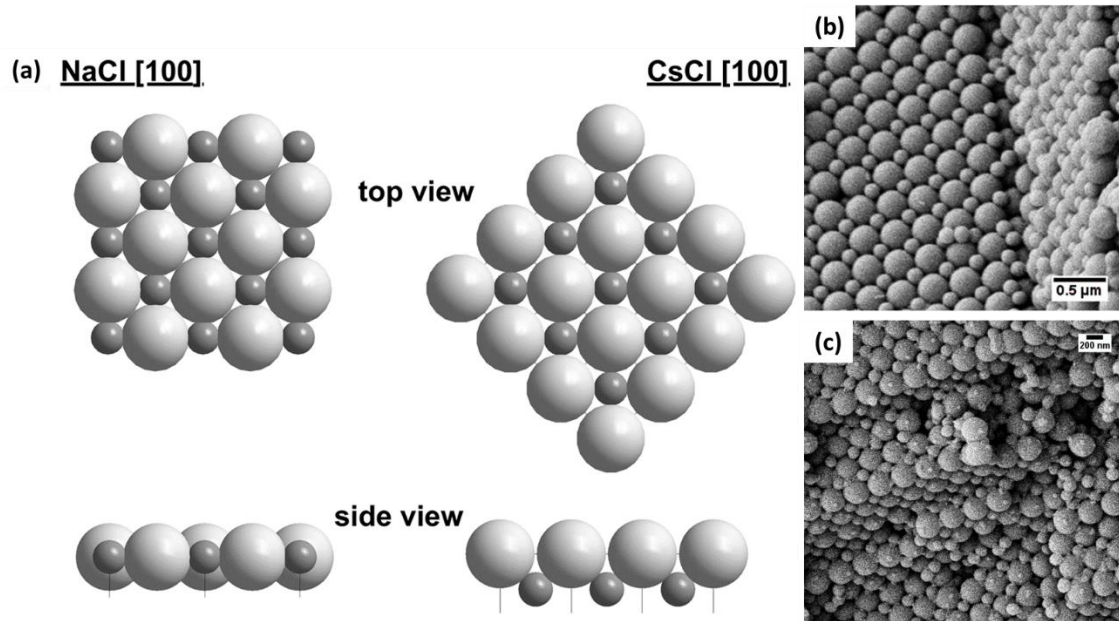


**Figure 4.2 - 10. (a) Comparison of NaCl and CsCl structure regarding a [100] perspective; (b,c) NaCl structure with tilted view.**

When comparing the packing parameter  $d_{PS1}/d_{PS2} = 0.5$  to the ideal value 0.414 for NaCl structure,<sup>107</sup> it turns out that the emergence of the NaCl lattice is not surprising. This value of  $d_{PS1}/d_{PS2}$  is very close to the thermodynamic optimum for this particular combination of particles. Therefore, the NaCl structure can also be obtained using only earth's gravitational field (1g) (see Figure 4.2 - 11).

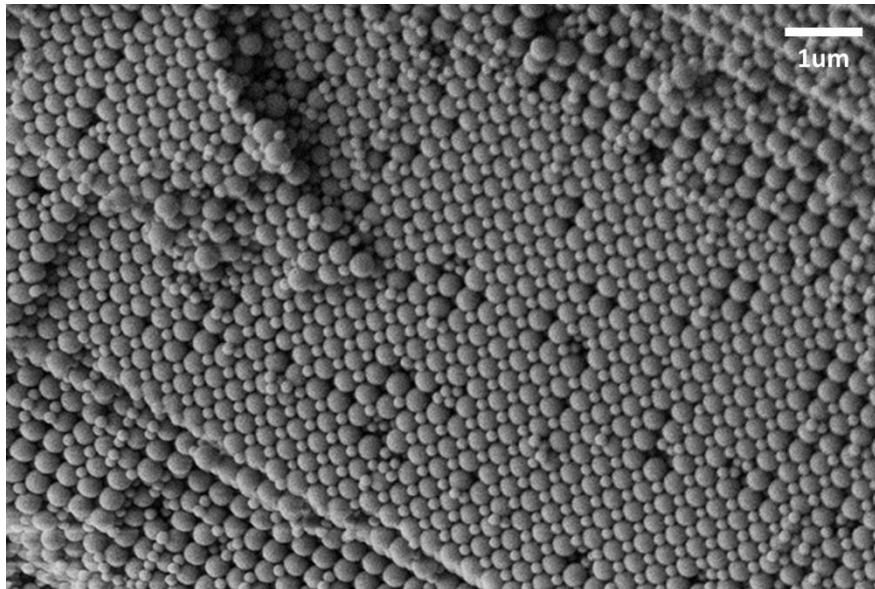


**Figure 4.2 - 11. Emergence of the structure with (PS1) (PS2) stoichiometry during sedimentation by standard gravitation (1g).**

What's more, complexity in ordered binary structures explodes when medium values of centrifugal force ( $F = 3.0 \times 10^3$  g) were applied to achieve medium separation conditions. Different periodic, thermodynamically less stable structures (Figure 4.2 - 12, Figure 4.2 - 13) have been observed.

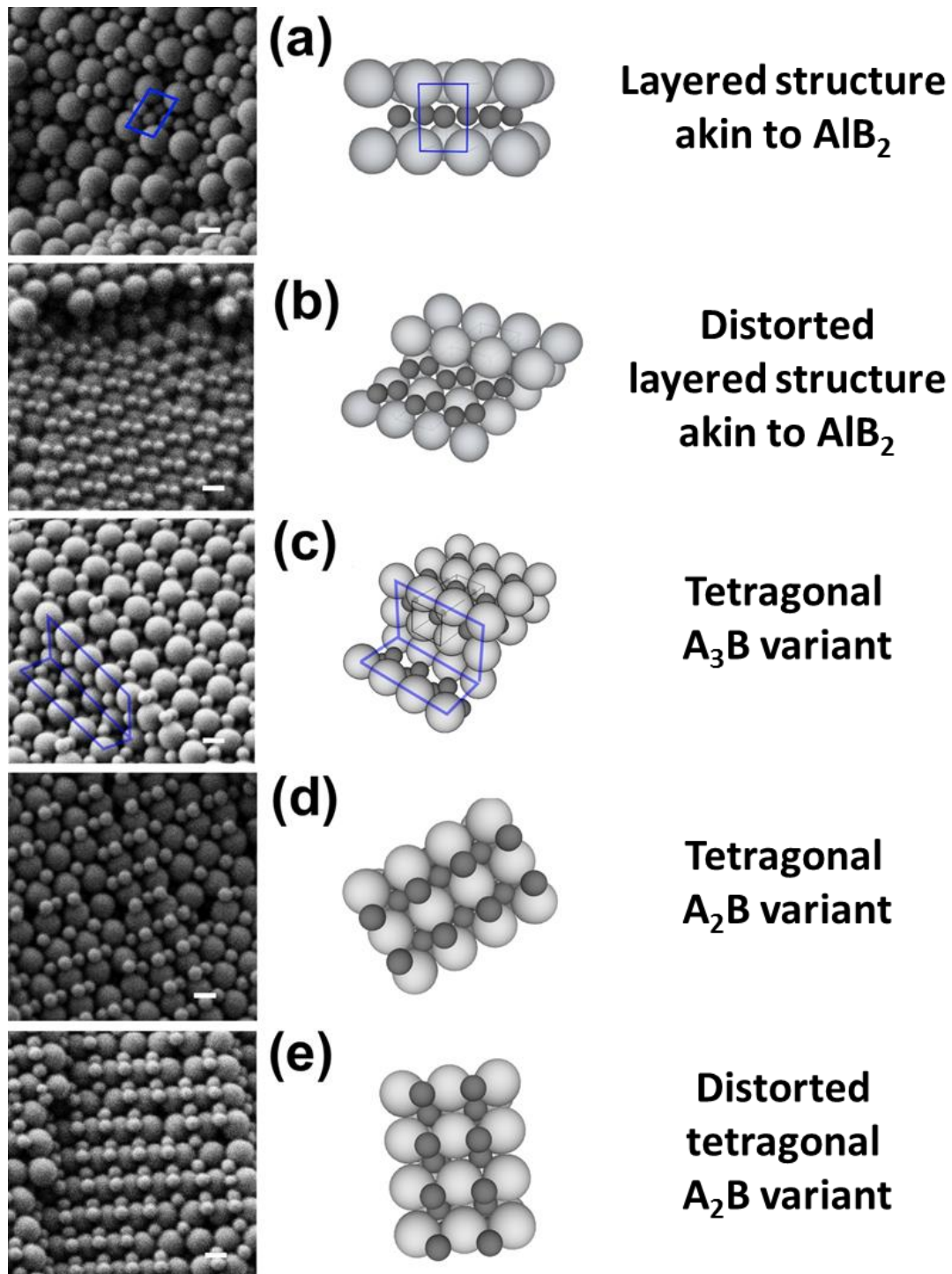
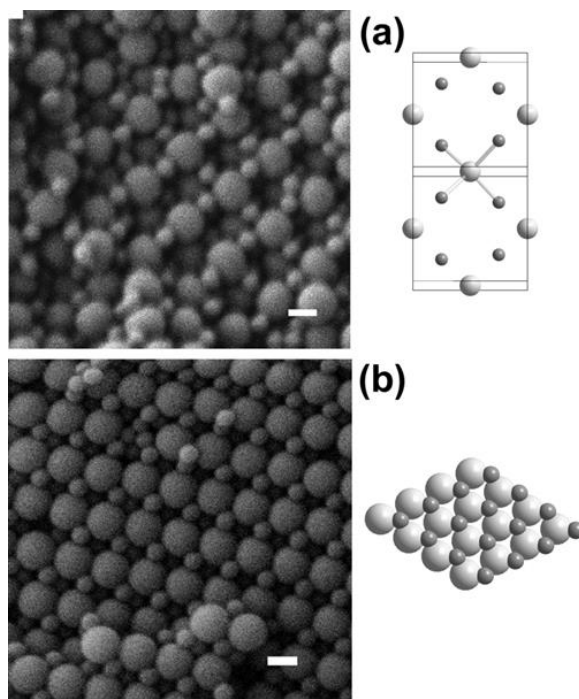


Figure 4.2 - 12. SEM images and schematic of the crystal lattice for different ordered binary phases obtained via centrifugation.



**Figure 4.2 - 13.**<sup>108</sup> SEM images of the non-dense structures. Atomic analogue: Sphalerite (a) and Wurtzite structure (b). Scalebars = 200 nm.

In a theoretical paper presented by Heras *et al* in 2013, a unique stacking diagram of all possible stacks under gravity were described<sup>109</sup>. Their results indicate that the ratio between the buoyant masses of each species is a key parameter which controls the stacking sequence of a mixture. Also the height of the sample should be carefully controlled which is described in our work in the form of  $\Delta r/L$ , where  $L$  is the height of the sample. However, all the binary structures presented above in our work can only be observed randomly in the whole piece of sample. It is not possible to establish a precise correlation between the preparative conditions and the resulted binary structures. Only some qualitative rules have been found regarding the number ratio  $N_{PS1}/N_{PS2}$  of PS1 and PS2. Slightly increasing the number ratio  $N_1/N_2$ , i.e. more smaller particles, tends to raise the chance to observe the non-dense structures shown in Figure 4.2 - 13. If the number ratio  $N_1/N_2$  is too low, ordered binary structures can be hardly found.

The structure shown in Figure 4.2 - 12a fits very well to a lattice with a densely packed layer of the larger particles PS2 as a basis. On top of this basis, a layer by regular filling of the voids of the PS2-layer was formed by the smaller spheres PS1. With an additional PS2-layer on top, the structure in Figure 4.2 - 12a is achieved. It indicates a 1:2 stoichiometry akin to aluminium diboride ( $AlB_2$ ; space group  $P6/mmm$ ), compared to structures related to atomic lattices. The structure in Figure 4.2 - 12b can be considered as a distorted aluminium diboride  $AlB_2$  structure with a movement of the PS1 spheres closer to each other in a pairwise fashion

(Figure 4.2 - 14). The distortion causes the structure shown in Figure 4.2 - 12b being slightly less symmetric, but still keeping the  $(PS1)_2(PS2)_1$  composition.

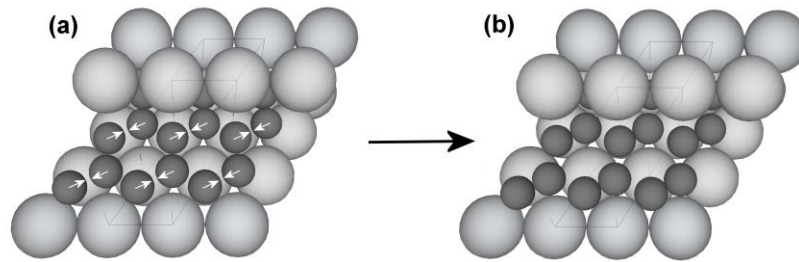


**Figure 4.2 - 14. Transformation of the regular  $AlB_2$  structure (a) into a distorted analogue (b). The white arrows indicate the direction of movement of the PS1 spheres.**

The structure shown in Figure 4.2 - 12c is no longer simply a distortion of the  $AlB_2$  structure. It changes to hexagonal in nature with a hash-shaped a,b unit cell basis. The edges help to identify the a,b and c directions and the isolated unit cell is shown in Figure 4.2 - 15 which corresponds to a  $(PS1)_3(PS2)_1$  stoichiometry. The (001) plane is composed of four PS2 particles arranged in a quadratic fashion ( $a = b = d_{PS2} = 300$  nm), with one PS1 sphere at the center. A tetragonal system is further confirmed by the c-extension = 430 nm.

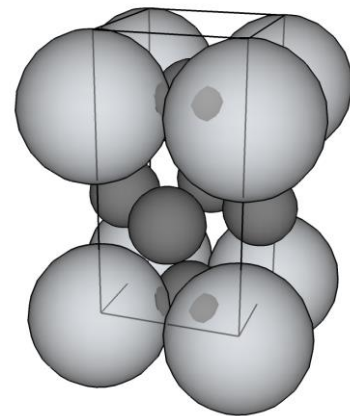


**Figure 4.2 - 15. Unit cell for the tetragonal  $(Sph1)_3(Sph2)_1$  phase.**

The ordered domains observed in Figure 4.2 - 12d are closely connected to the latter tetragonal structure. The transformation can be realized by removing two symmetry equivalent spheres from the PS1-layer (Figure 4.2 - 16). This transformation changes the stoichiometry from  $(PS1)_3(PS2)_1$  to  $(PS1)_2(PS2)_1$ .

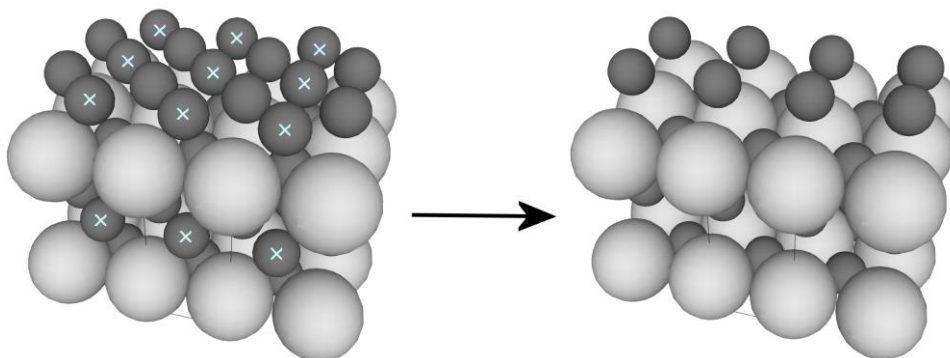


**Figure 4.2 - 16. Transformation of the tetragonal structure assigned for Figure 4.2 - 12c into the structure related to Figure 4.2 - 12d by partial elimination of PS1 spheres. The white cross indicates the PS1 spheres which are removed.**

Based on the structure in Figure 4.2 - 12c, the PS1 spheres are able to slightly change their position due to more space in the [002] layer. With the transformation shown in Figure 4.2 - 17, the structure shown in Figure 4.2 - 12e is obtained.

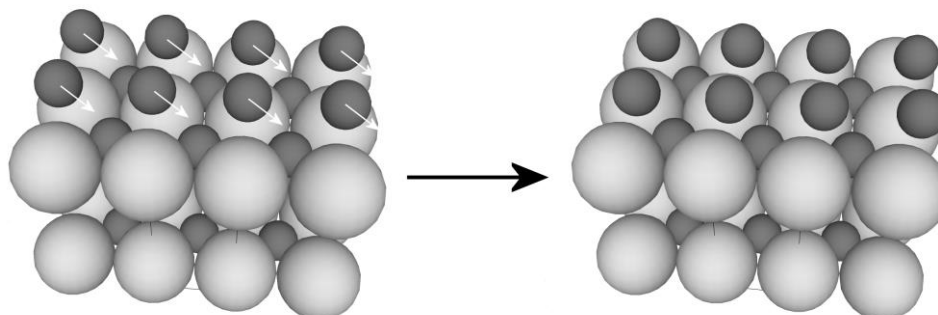


**Figure 4.2 - 17. Transformation of the structure assigned for Figure 4.2 - 12d into the structure related to Figure 4.2 - 12e. The white arrows indicate the direction of movement of the PS1 spheres.**

Besides the different ordered binary structures observed in Figure 4.2 - 12, even thermodynamically less stable structures emerged. A periodic structure characterized by the same stoichiometry as the NaCl structure (1:1) is shown in Figure 4.2 - 13a. The packing factor is much lower than that of NaCl. From the SEM image, a tetrahedral (4/4) coordination can be clearly identified. This non dense packed structure is in good agreement to the Sphalerite structure ( $F\bar{4}3m$ ). In addition to the Sphalerite structure, another pattern can also be found in Figure 4.2 - 13b, which fits to the hexagonal analogue Wurtzite ( $P6_3mc$ ). However, the ideal value of  $d_{PS1}/d_{PS2}$  for the Sphalerite or Wurtzite is 0.225, is much smaller compared to  $d_{PS1}/d_{PS2} = 0.5$ . Thus, the emergence of the shown structures with (4/4) coordination is very astonishing. This serves as one important motivation to investigate the mechanism of how centrifugal force leads the binary colloidal systems to various structures.

Although different binary structures have been observed, it should be noted that the prevalence of the structures is very different. Relatively large areas ( $>10 \mu\text{m}$ ) characterized with the denser NaCl and  $\text{AlB}_2$  structure have been found (see Figure 4.2 - 18). The emergence of the other phases is more seldom which is already expected. It is not possible with our methods to gain a precise quantification to assess the relevance of thermodynamic versus kinetic factors. At the moment, SEM is the only way to approach the structures and it only gives information about the surface. The structures are present side-by-side in 3D. It is not possible to know at which position a domain is seen, and how far the domain extends in 3D.

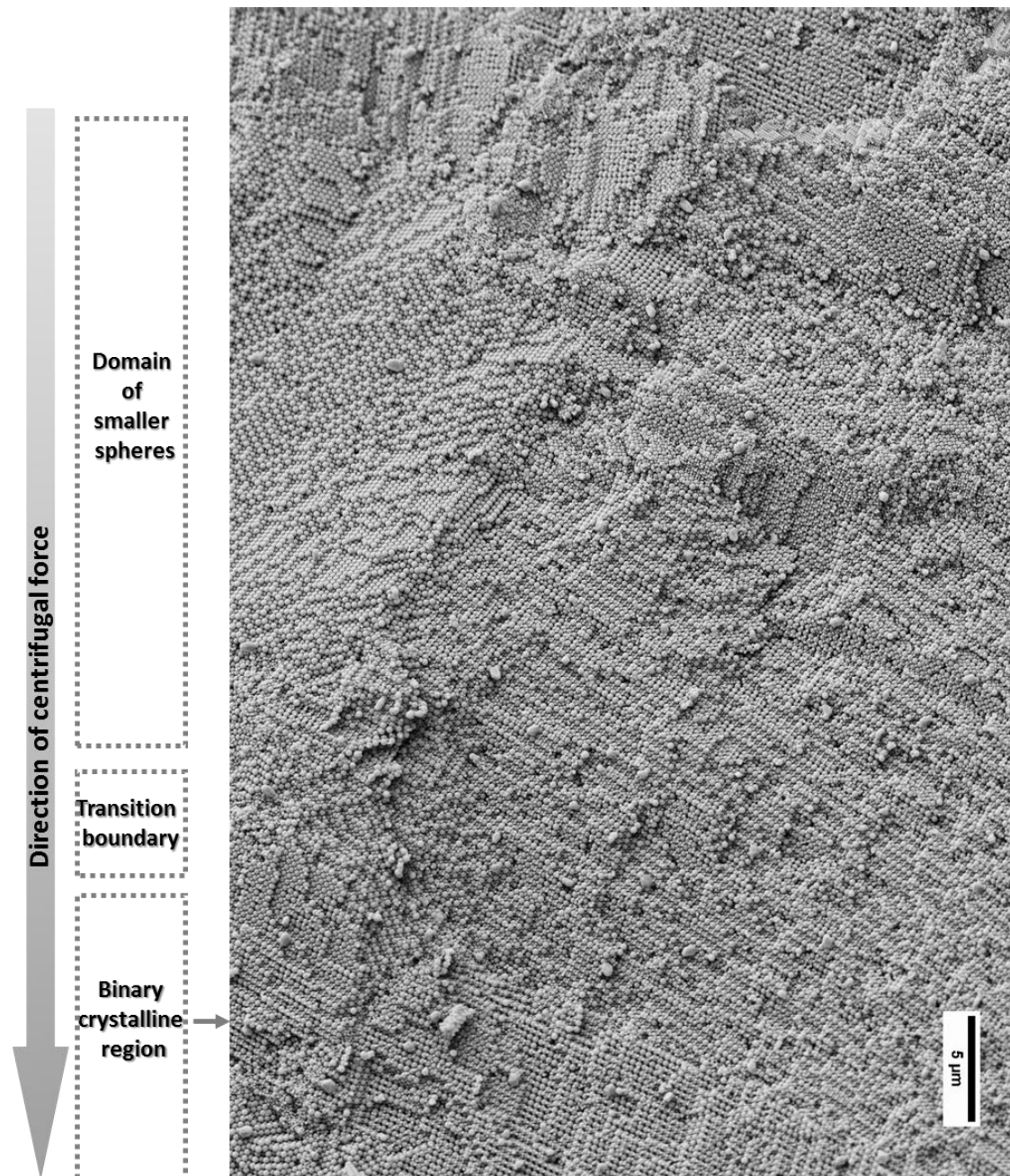


Figure 4.2 - 18. Prevalence of binary crystalline regions.

#### 4.2.4 The mechanism leading to various structures

The ordered binary structures observed in Figure 4.2 - 9 and Figure 4.2 - 12 could be explained by the influence of the centrifugal field induced particle concentration on the packing considerations and stoichiometry. However, Sphalerite and Wurtzite shown in Figure 4.2 - 13

are obviously less dense structures, that were formed despite the presence of the centrifugal force which acted as the force for densification. Furthermore, the low coordination number with local tetrahedral symmetry is very hard to be understood for hard colloidal particles with repulsive, spherical interaction potentials. This phenomenon is the first indication that the mechanism leading to the various structures might be complex.

Further indication for a complex mechanism comes from the inspection of the entire length of the sedimentation body (Figure 4.2 - 6b,c and Figure 4.2 - 19). A closest packed PS2 phase was found at the bottom of the centrifugation tube, which is indeed very unusual. The commonly expected fractionation of a mixture in centrifugal field is shown in Figure 4.2 - 20. Prior applying a centrifugal field, the mixture of two spheres types is homogeneous in the entire centrifuge tube. Although the sedimentation coefficients of PS1 and PS2 are different from each other, smaller spheres PS1 which stay close to the bottom of the vial will be trapped at the bottom part of the vial to form a binary mixture, when centrifugation and sedimentation begins. Therefore, the absence of PS1 in the bottom region is another indication for a complex mechanism.

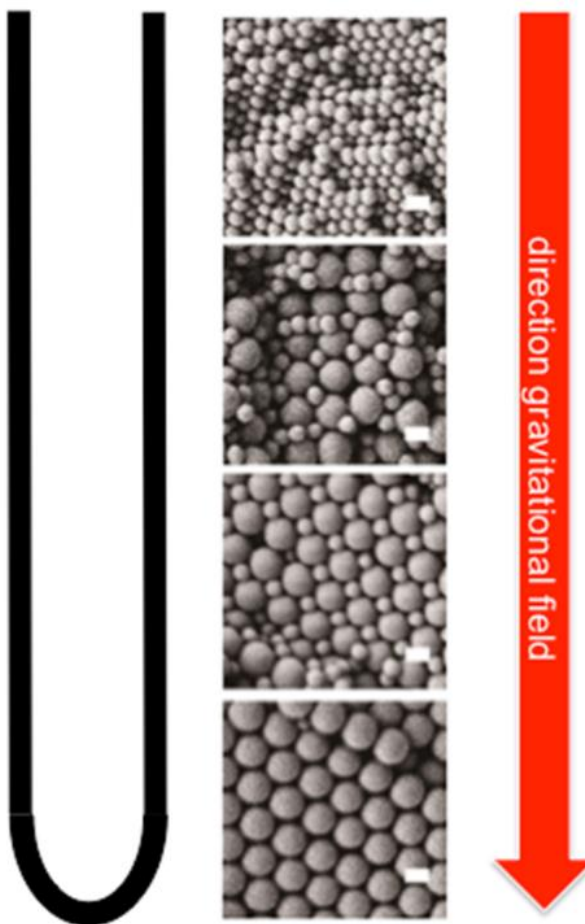


**Figure 4.2 - 19. Investigation of the entire length of the sedimentation body. Scale bars  $\cong$  200 nm.**

In the last part of section 4.1, cross linked polyacrylamide network is introduced to the colloidal dispersion to obtain freestanding photonic glasses. The same concept was also applied here to investigate the complex mechanism. The strategy is as follows: mixing acrylamide monomer with polystyrene colloidal dispersion, running the mixture in the centrifuge, adding initiator to obtain the polyacrylamide network in between of polystyrene spheres and therefore fixing the structure on a macroscopic scale, finally repeating the whole procedure at different centrifugation times. The sedimentation process can be recorded from the beginning till the end if this strategy worked out. Unfortunately, it was not as easy as in section 4.1 to prepare a freestanding sample for further investigation. After adding the initiator, the sample was just

partially fixed and not robust enough to be taken out of the centrifuge tube. This is primary due to the amount of the polyacrylamide in the interstices of the colloidal spheres. Here in this case the volume fraction of the interstices is much lower than that of the unordered packing structure in section 4.1. Besides acrylamide, gelatin which melts to a liquid when heated and solidifies when cooled again, was also tried. But it did not work either due to the low volume fraction of the interstices between the colloidal spheres.

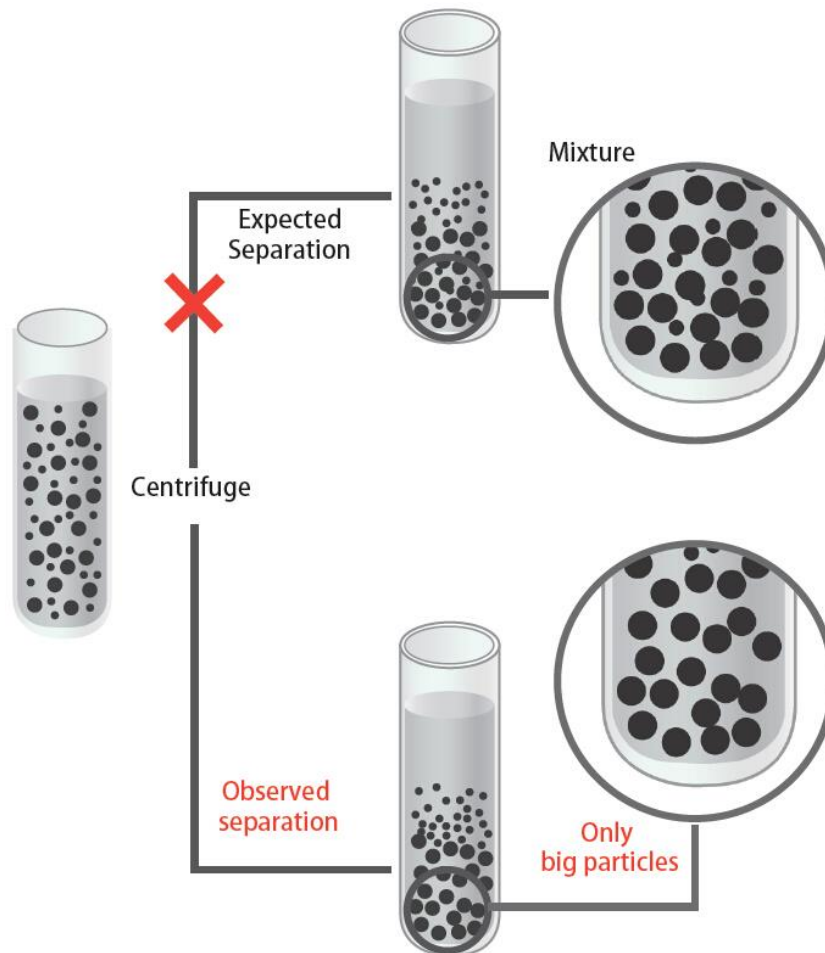


**Figure 4.2 - 20. Schematic representation of the sedimentation process expected vs observed at the bottom of the centrifugation tube.**

The smaller particles PS1 which should have been trapped in the bottom part of the vial can go nowhere else than moving upward. But this upward movement cannot be understood by the standard buoyancy term  $(1 - \bar{v}\rho)$  with  $\bar{v}$  = partial specific volume of the sample (0.949 ml/g for Polystyrene) and  $\rho$  = solvent density, which predicts sedimentation of the polystyrene latexes as their density is higher than that of the solvent (water). Thus, the solvent should not be considered as a one-component system (water) anymore but as a dispersion consisting of host latexes.

In the case of concentrated binary dispersions, the buoyant force exerted on a sedimenting particle can be strongly affected by other components in the solution.<sup>104</sup> The binary colloidal dispersion in the current work can be treated as a host (PS2) dispersion containing guest particles (PS1) (see Figure 4.2 - 21). A depletion layer of water with a density which is lower than that of the surrounding host dispersion makes up the surrounding environment of the guest particle (PS1). Then it is easy to understand that the guest particles would possibly float depending on the thickness of the depletion layer.<sup>104</sup>

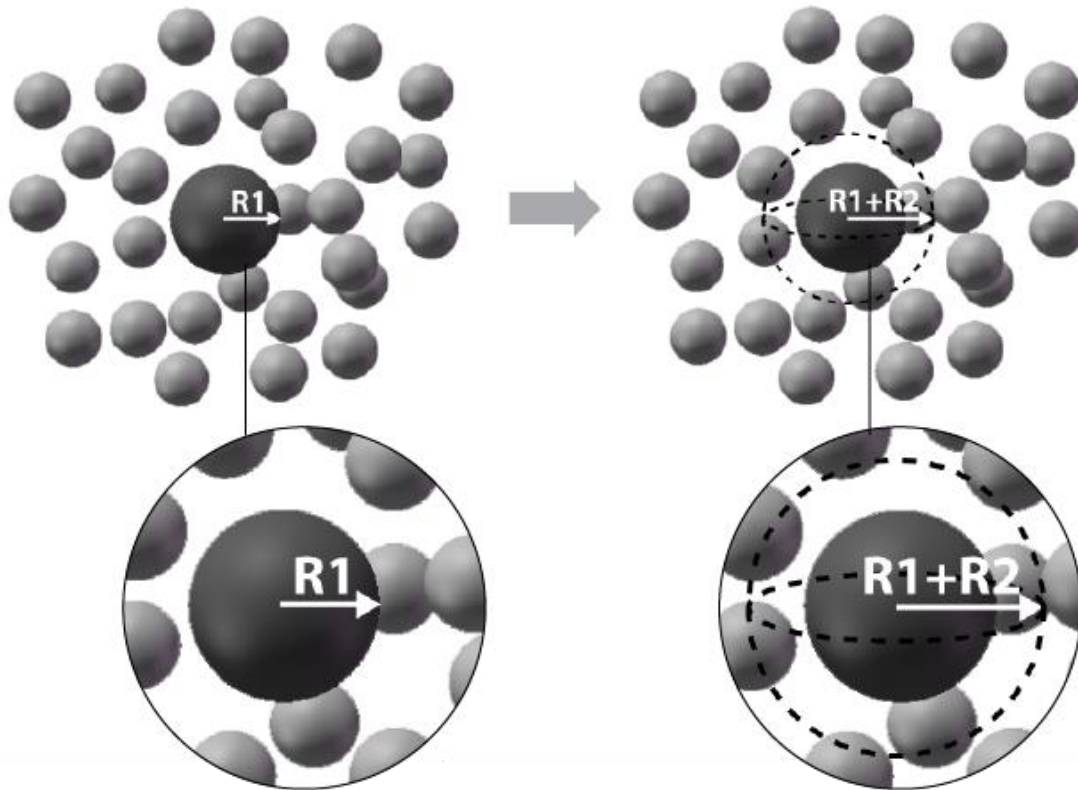


**Figure 4.2 - 21. Schematic illustration of the effect of the insertion of a spherical guest particle of size  $R_1$  into a colloidal dispersion of host particles with size  $R_2$ . The host particles are excluded from a volume which is larger than that of the guest particle volume  $V_1$  by a factor of  $(1 + R_2/R_1)^3$ .**

Instead of using the simple excluded volume model, the buoyancy force can be obtained by using density functional theory (DFT)<sup>110</sup> and the Mansoori-Carnahan-Starling equation of state for hard sphere mixtures which yield Equation 4.2- 2 for the effective density  $\rho^*$  of the host suspension:<sup>104</sup>

$$\frac{\rho^* - \rho_0}{m_2 n_2} = \frac{6 - 2(2 - 3q)(1 - \Phi_2) - 3(1 - q^2)(1 - \Phi_2^2) + (1 - q)^2(2 + q)(1 - \Phi_2)^3}{2(4 - \Phi_2)\Phi_2 + (1 - \Phi_2)^4}$$

**Equation 4.2- 2**

$$m_2' = (\rho_2 - \rho_0)v_{PS2} \quad \text{Equation 4.2- 3}$$

$$n_2 = \frac{N_{PS2}}{V} \quad \text{Equation 4.2- 4}$$

$$q = \frac{d_{PS1}}{d_{PS2}} \quad \text{Equation 4.2- 5}$$

where  $\rho_0 \cong$  density of the pure solvent,  $\rho_2 \cong$  density of PS2 particle,  $m_2 =$  mass of PS2 particle,  $v_{PS2} \cong$  volume of a PS2 particle,  $n_2 =$  concentration of PS2 particles,  $N_{PS2} \cong$  number of PS2,  $V \cong$  total volume of the suspension,  $\Phi_2 \cong$  volume fraction of the PS2 particles with  $\Phi_2 = 1 - \Phi_1$ ,  $d_{PS1}$  and  $d_{PS2}$  are the diameters of PS1, PS2 respectively.

When the host particles (PS2) have a volume fraction exceeding a certain value, the effective density  $\rho^*$  of the solvent becomes equal or even higher than the density of the guest particles (PS1). Under this circumstance, the upward movement of PS1 happens. For the binary colloidal systems under investigation in the current work, the threshold volume concentration for floatation of PS1 is 0.05. In all the binary colloidal systems studied in the current work, before the centrifugation starts, the entire length of the column in the tube has a higher volume concentration than 0.05 which leads to a large effective density  $\rho^*$  of the solvent. The floatation of the guest particles will get pronounced as the difference in particle size increases.<sup>104</sup>

As mentioned at the beginning of this section (Figure 4.2 - 1), software like Sedfit can generate sedimentation profiles, although equilibrium cannot be achieved in the current system. The simulated sedimentation process should be able to be tested and corrected experimentally by the AUC measurements. Thus in principle the simulated data can be used to predict the concentration gradients with any kinds of centrifuge rotor, tube, speed, etc. With the concentration gradients, quantitative calculation of the radially dependent effective density  $\rho^*$  can be extracted by combining Equation 4.2- 2 - Equation 4.2- 5.

Although it should be possible to get the radial concentration gradients of both latexes in the binary mixture via the Analytical Ultracentrifuge, the strong light scattering from the polystyrene nanospheres makes the detection impossible. Up to 60 % sucrose was used to match the PS refractive index as closely as possible. But the scattering problem still could not be resolved.

In addition, the calculation of Péclet number may also help to understand the mechanism. The Péclet number characterizes the strength of convection to the strength of diffusion. When the Péclet number is small, Brownian motion is significant. Conversely, convection dominates. If

there are dissipative mechanisms at work, their magnitude would be parameterized as a Péclet number, and this value should therefore be computed for the two different particle sizes. Unfortunately, the calculation of a Péclet number for each particle size turns out to be not possible due to the radial concentration gradients at high particle concentrations. The reason lies in the concentration dependent diffusion coefficient, which changes locally in the centrifuge tube.

To test the dynamics of the binary systems, a two-step sedimentation experiment was conducted. A centrifugal force of  $F = 1.2 \times 10^4$  g was firstly applied to a binary colloidal dispersion for 20 min. Then the centrifugal force was decreased to  $F = 1.2 \times 10^2$  g, at which the same centrifuge tube was centrifuged for another 5 h. As already shown in Figure 4.2 - 9a, the first step performed under high centrifugal force results in a binary glassy state. However, with the second step, all colloidal particles reorganized and a periodic binary phase was observed. This dynamic process is illustrated in Figure 4.2 - 22.

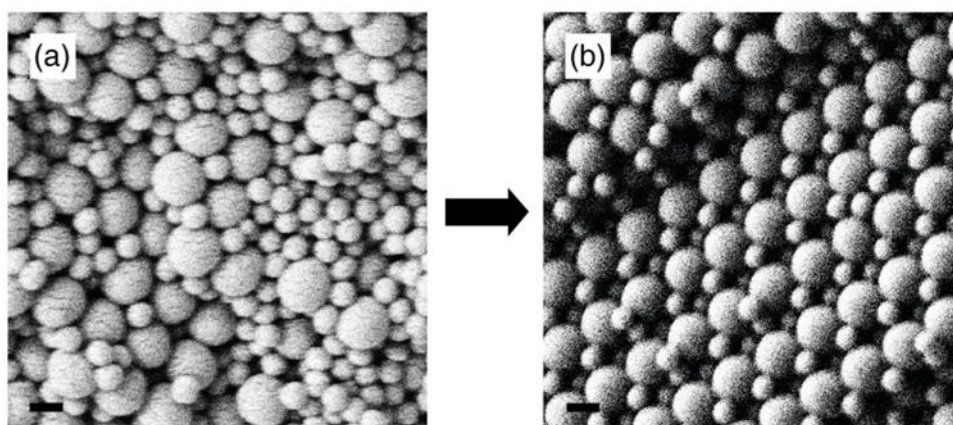


**Figure 4.2 - 22.**<sup>108</sup> SEM micrographs for the two-step sedimentation experiment at  $F = 1.2 \times 10^4$  g for 20 min first (a) followed by  $F = 1.2 \times 10^2$  g for 5h (b). Scalebars  $\cong 200$  nm.

### 4.3 Functional porous carbon monoliths: from multinary colloidal assembly to a defined gradient porosity

The templating strategy has built a very tight link between colloidal assembly and porous materials, which find use in areas like adsorption, separation, catalysis, sensing and lately also in energy-storage applications. The design and functionality of nanoporous materials made from colloidal templates have been intensively studied. Among the enormous work invested in controlling pore sizes and chemical functionalities, the benefits of materials with bimodal pore-size distribution deserve attention.<sup>111-113</sup> A particularly unique class is the so-called functional gradient materials (FGMs),<sup>114</sup> of which the composition or structure changes continuously along one axis (Figure 4.3 - 1).

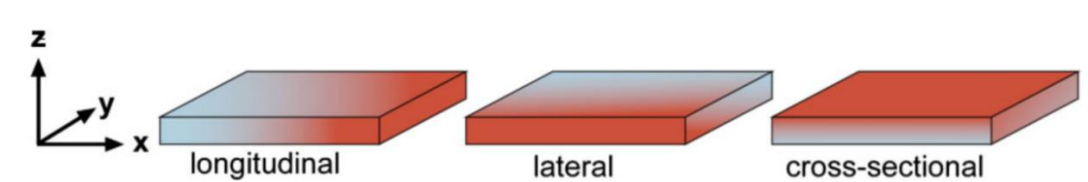


**Figure 4.3 - 1.**<sup>115</sup> Gradient materials that continuously changes its composition or structure along an axis.

Gradient materials distinguish themselves from bilayer materials which possess a sharp interface (Figure 4.3 - 2<sup>115</sup>). For example, regarding the mechanical properties, gradient materials are not susceptible to radial stress when a longitudinal force is applied.

Indeed, gradient materials are not an invention from human beings. Nature is the master in designing and constructing gradient materials. Tendons are very good examples as an effective biological solution. Soft tissue (muscle) is attached to stiff and hard tissue (bone). This gradient in stiffness serves to transfer loads across joints.<sup>116</sup> Another clever

gradient created by nature is the mussel byssus which is used to attach the mussel to rocks.<sup>117</sup> With a continuous change of collagens in different composition, an alteration of E-modulus in a range of 50–500 MPa can be achieved. While the proximal part of the thread (connected to the soft tissue of the mussel) is elastic, the distal part is stiff and ensures a strong attachment to the surface, for example rocks.<sup>115</sup>

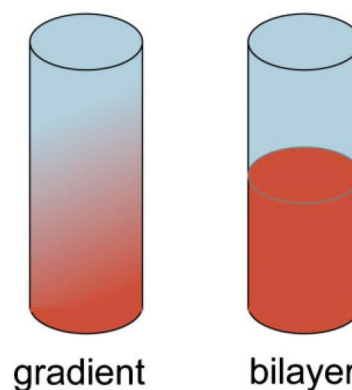


**Figure 4.3 - 2. Schematic comparison of a gradient material and a bilayer material.**

Researchers have been interested in synthesizing gradient materials before realizing that the gradient materials exist in nature. The first motivation to develop gradient materials is from the field of aeronautic research, aiming to get high performance thermal barrier materials. Such thermal barrier materials are made from metal or ceramics. In the context of nanomaterials, there are also some nice pioneer works. Brandon *et al.* showed the benefits of a gradient pore structure in the solid-oxide fuel cell in 2006.<sup>118</sup> A. Schachtschneider *et al.* presented macroporous organosilica aerogels having gradient porosity in 2015.<sup>119</sup> Luo *et al.* described a macroporous hydrogel composed of N-isopropylacrylamide (NIPAM) prepared by hydrothermal synthesis.<sup>120</sup> However, in all the above work the pore sizes are in the micrometer range with broad pore size distribution. It will be highly interesting if gradient porous materials with nanometer scale pores as well as more defined pore size distributions can be achieved.

More than providing outstanding performance in a certain property, e.g. thermal barrier, gradient materials can also be expected to create directional transport of matter, charge carriers or energy. From this point of view, the free standing shape of gradient materials is in great demand, although the research on gradient porous materials is just at the starting phase with a lot of difficulties in front.

The feasibilities of using a centrifugal field to prepare monolithic materials as well as suitable templates for gradient porous materials have been demonstrated in the previous two result parts (section 4.1 and 4.2). Based on the prior knowledge of section 4.1 and 4.2, the goal of this part is to develop a novel approach with broad applicability for the generation of nanoporous, crack-free monoliths with tailor-made gradient porosity. Carbon, which is among the most significant elements on earth is selected as a model, while all the existing achievements in synthesizing gradient porous materials are from non-conducting materials. The obtained materials will be tested for Li-O<sub>2</sub> battery technology, as significantly different performance for the monoliths positioned in the two alternative directions within the battery device has been predicted by theoretical studies.

### 4.3.1 Approaching gradient porous carbon materials via the conventional templating route

To obtain porous materials, the conventional synthesis routes for hard templating involves four general steps,<sup>121</sup> starting with the synthesis of precursor solutions. To obtain porous carbon materials from the templating route, different carbon precursors can be adopted. A reliable approach is the resorcinol-formaldehyde (RF) route.<sup>122</sup> The second step consists of

infiltrating the void spaces in a hard template with the selected precursor solution. A very straightforward idea to approach gradient porous carbon is to infiltrate the RF sol as a carbon source into the monoliths prepared in section 4.2 which contain a nicely defined gradient. After the infiltration has finished, the precursor needs to be transformed into a solid phase material. The final step is the removal of the template. Thermal treatment was performed in an inert gas as an effective way to remove the polymeric template as well as to induce the transformation of RF precursor to carbon (pyrolysis).

Before exploring gradient porous carbon materials using a bimodal mixture of PS spheres as templating entities, the monodisperse system is firstly investigated to prove the general feasibility of the method. Via the conventional infiltration method, inhomogeneous infiltration (Figure 4.3 - 3b) of the RF sol cannot be avoided due to the macroscopic scale (Figure 4.3 - 4a) of the template. What's more, extra RF sol precursor remained at the outer surface of the template which could mostly block the sample. During the thermal treatment, the blocked channel would probably increase the internal pressure of the sample. Therefore, irregularly shaped pieces (Figure 4.3 - 4b), macroscopic and microscopic cracking (Figure 4.3 - 4c,d) resulted.

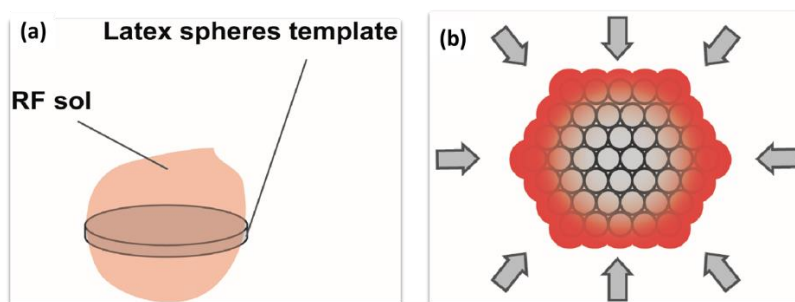


**Figure 4.3 - 3. Schematic illustration of the infiltration method for the preparation of monolithic porous carbon.**

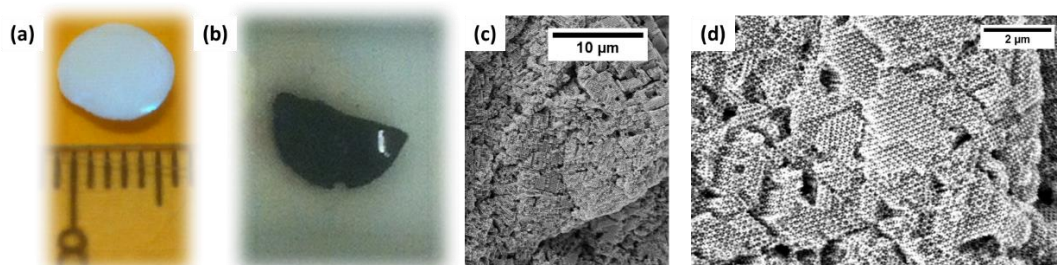


**Figure 4.3 - 4. Preparation of porous carbon materials using a classical infiltration approach. (a) photographic image of the PS template monolith prior to resorcinol-formaldehyde infiltration; (b) photographic image of the porous carbon material after carbonization; (c, d) SEM images of the porous carbon material.**

As the defects already widely spread in the porous carbon prepared from the template consisting of monodisperse PS, it was therefore not surprising to observe even more defects (Figure 4.3 - 5) with the gradient template.

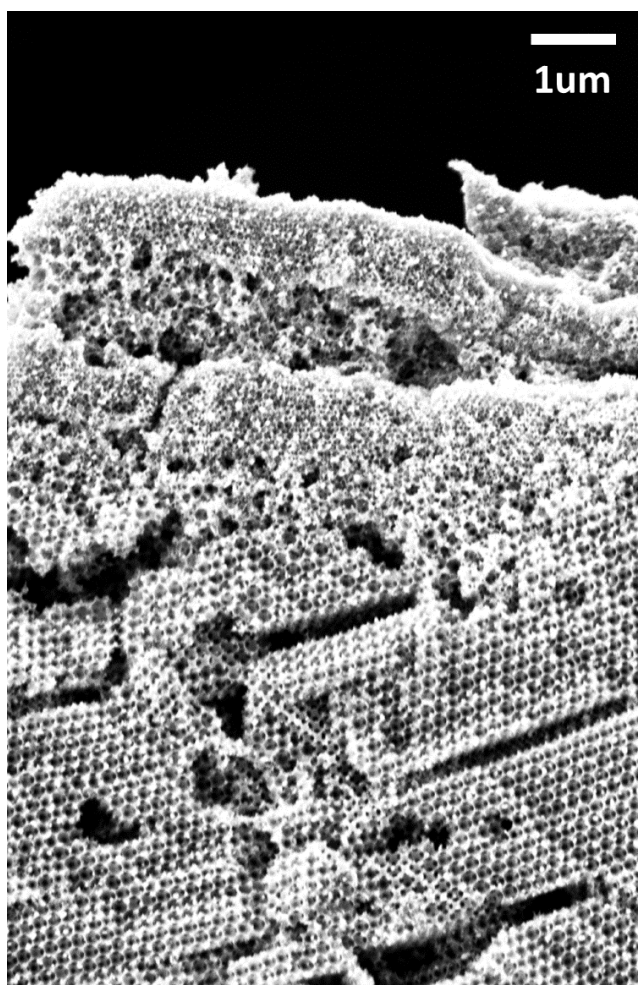


**Figure 4.3 - 5. SEM image which characterizes the gradient zone of a gradient porous carbon material.**

The bottleneck of the conventional synthesis routes for good quality porous carbon monoliths lies in the second step filling the precursor into the PS template. In order to ensure that the precursor uniformly fills the template, the assistance of vacuum suction has been reported to improve the infiltration of the precursor.<sup>123</sup> But the assistance from vacuum was still not sufficient for such a macroscopic template adopted in current work. The conventional synthesis route was abandoned. The infiltration difficulty triggered the idea to get rid of the infiltration step completely, to reach a porous carbon with limited defects which is crucial to preserve the gradient structures.

### 4.3.2 Developing a new synthesis route for crack-free gradient porous carbon materials

#### 4.3.2.1 First modified synthesis route

To assure that the interstices between PS spheres are completely filled with RF precursor which is later transformed to carbon, the first idea to modify the conventional synthesis route is to assemble the PS spheres directly in the RF sol and catalyze the gelation of RF sol when the assembly of PS spheres is finished, like the synthesis route for free-standing photonic glasses described in section 4.1.3.

Figure 4.3 - 6a shows a centrifugal tube with RF/PS composite which can be found at the very bottom of the tube. The upper part with much darker color is pure RF sol which served as the solvent in the centrifugation process. After 3 days' gelation, the whole sample can be taken out of the centrifuge tube easily as the sample experienced shrinkage. The free standing RF/PS composite retained the monolithic shape and showed no defects macroscopically (Figure 4.3 - 6b). After thermal treatment in the inert gas  $N_2$ , the porous structure was characterized with SEM (Figure 4.3 - 6c). The cracks in the sample have been significantly decreased. But besides the uniform porous region, some PS spheres wrapped by carbon can be found.

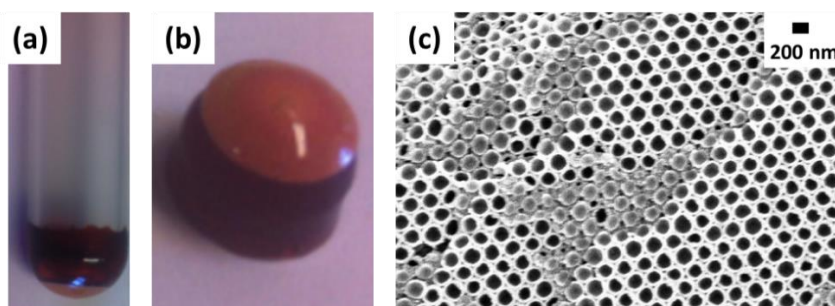


**Figure 4.3 - 6. Samples obtained from the first modified synthesis route. (a) A centrifuge tube (Polyallomer™ 13\*51 mm) with RF/PS composite inside; (b) Free standing RF/PS composite taken out of the centrifuge tube; (c) SEM image of the porous structure.**

Some regions with PS spheres wrapped by carbon might be due to the catalyzed RF gelation step after centrifugation. A few drops of  $Na_2CO_3$  solution were added from the top of the centrifuge tube when the assembly of PS spheres in RF sol finished to catalyze the gelation process of the RF sol. The close-packed structure of PS spheres at the bottom part of the tube might be disturbed. Therefore, excess RF sol precursor stayed around PS spheres and prevented the PS spheres from decomposition during thermal treatment.

#### 4.3.2.2 Second modified synthesis route

To avoid the close-packed PS spheres being destroyed, the next idea was to assemble the PS spheres directly in the RF sol and finish assembly before gelation takes place. This can be realized by mixing PS spheres and RF sol together with the catalyst  $\text{Na}_2\text{CO}_3$  before putting the mixture into the centrifugal field. By tuning the amount of  $\text{Na}_2\text{CO}_3$ , a condition can be found to assure that the assembly of PS spheres finishes firstly. In addition, the density of the RF sol which served as the solvent can be adjusted by controlling the amount of water in the RF sol. When the RF sol has a higher density compared to PS spheres, the PS spheres would float instead of sediment to the top of the centrifugal tube. Therefore, it is also possible to collect the PS/RF composite at the top of the centrifuge tube by creating a floatation of the PS spheres. As a swing-out centrifuge rotor was used here as in section 4.1.3, which assures a horizontal centrifugal force parallel to the centrifuge tube, the floatation of the PS spheres would result in a flat layer at the top of the centrifuge tube. The flat layer shape can provide much convenience for any further property investigation. The general co-assembly process via this second modified synthesis route is illustrated in Figure 4.3 - 7.

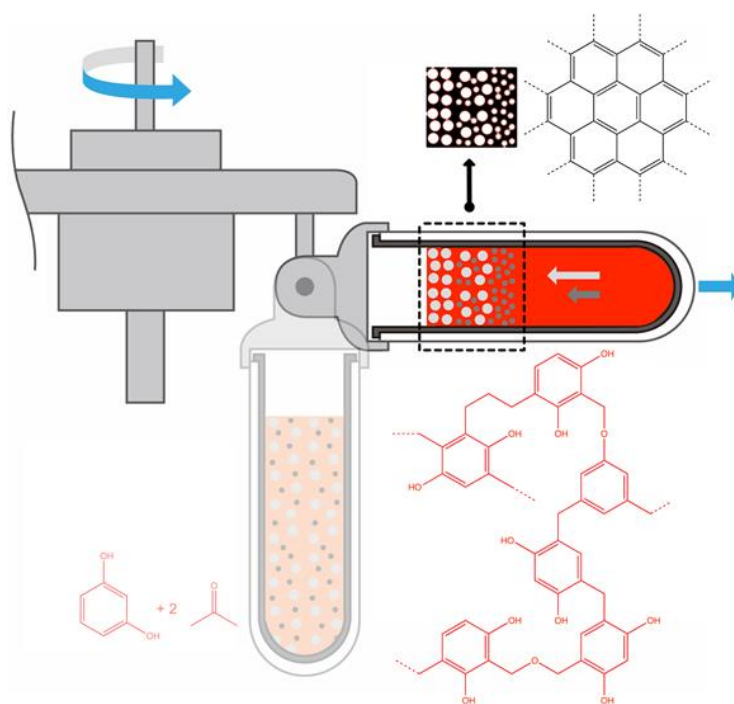


**Figure 4.3 - 7.**<sup>124</sup> Swing out rotor filled with a colloidal solution of PS spheres (eventually of different size) plotted as gray circles and a resorcinol formaldehyde sol (salmon color). The rotation and the direction of the gravitational field is marked by blue arrows. Flotation of the PS spheres (different flotation rates marked by gray arrows) and polycondensation of the RF gel (red) take place simultaneously to each other. Finally, a monolithic RF/PS composite gel can be separated and is converted to porous  $\text{sp}^2$ -hybridized carbon (black) finally with gradient pore-structure.

After a certain amount of centrifugation time, the PS/RF composite became robust enough to be cut from the top of the whole sample body (scheme shown in Figure 4.3 - 8a and sample photo shown in Figure 4.3 - 8b left). The final macroporous carbon was delivered by calcining the PS/RF composite under inert gas to remove the PS latex which worked as the template for the porous structure. The resulting porous carbon monoliths (Figure 4.3 - 8b right) have a diameter larger than 0.5 cm.

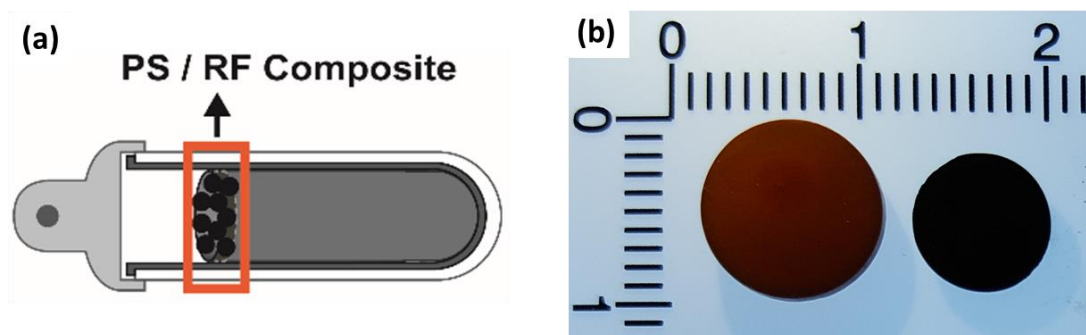


**Figure 4.3 - 8. (a) Scheme of the flat RF/PS composite layer formed at top of the centrifuge tube; (b) photographic image of RF/PS composite (left) and porous carbon (right).**

Compared to the RF/PS composite, the porous carbon monolith has shrunk in size/volume because of the loss of  $H_2O$  and densification caused by progressing C-C bond formation (see Figure 4.3 - 7). Thermogravimetric analysis (TGA) (Figure 4.3 - 9a) shows that the transformation to carbon took place at  $T = 437$  °C. From the Fourier transform infrared spectroscopy (FTIR) (Figure 4.3 - 9b), the presence of water was found in RF/PS samples at wavenumber 3300 and vanished with the porous carbon.

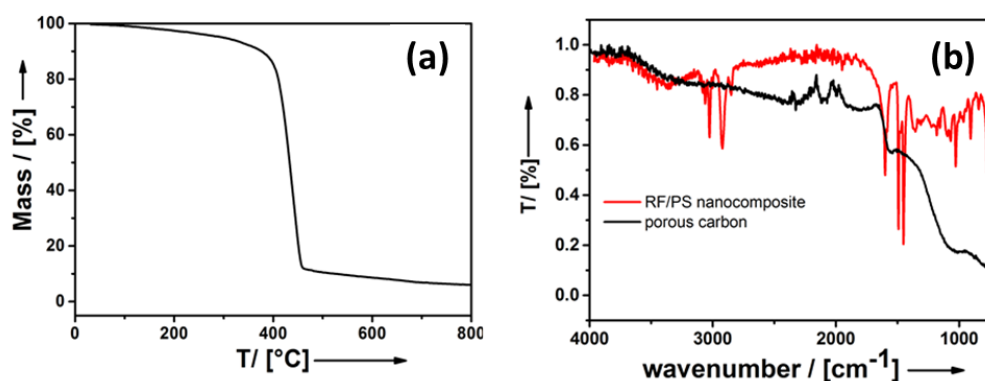


**Figure 4.3 - 9. Conversion from RF/PS composite to carbon. (a) thermogravimetric analysis in  $N_2$  atmosphere; (b) FTIR spectrum of the RF/PS composite and the porous carbon monolith.**

Furthermore, the porous carbon successfully converted from RF/PS composite was characterized by FT-Raman spectroscopy and powder X-ray diffraction (PXRD). The Raman spectrum displays two broad bands at  $1298\text{ cm}^{-1}$  and  $1607\text{ cm}^{-1}$ , which is characteristic for disordered carbon with predominantly  $sp^2$  hybridization.<sup>125 126</sup>

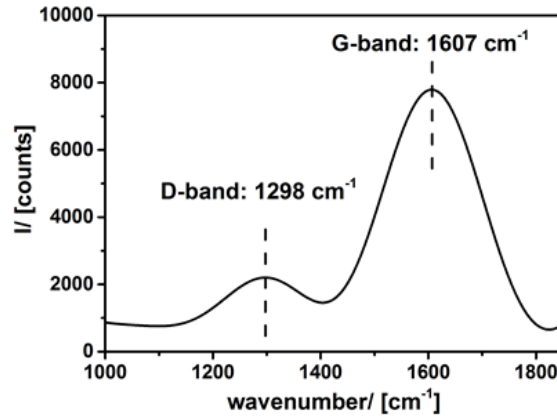


**Figure 4.3 - 10. FT-Raman spectrum of the porous carbon monolith.**

The PXRD pattern further reveals the crystallinity of the carbon materials (Figure 4.3 - 11). Only two diffraction peaks located ( $2\theta = 25^\circ, 44^\circ$ ) were observed. They can be assigned to the (002) and (101) planes of graphite. However, the large width of the signals ( $\Delta 2\theta_{002} = 7.8^\circ$ ; full width at half maximum) processed using Scherrers equation correlate to a domain size in c-direction of less than 2nm. This agrees with a highly disordered, turbostratic carbon.

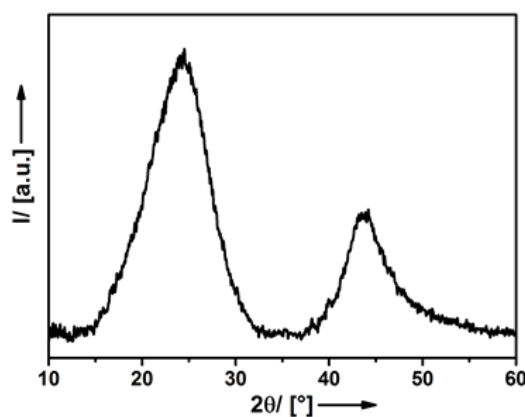


**Figure 4.3 - 11. Powder X-ray diffraction of the porous carbon monolith.**

From the SEM images taken at different magnifications shown in Figure 4.3 - 12, it can be found that the porous carbon monoliths are crack-free on the micro- and nanoscale, mostly due to the co-assembly process in which the RF sol acted as a temporary glue for the PS particles.

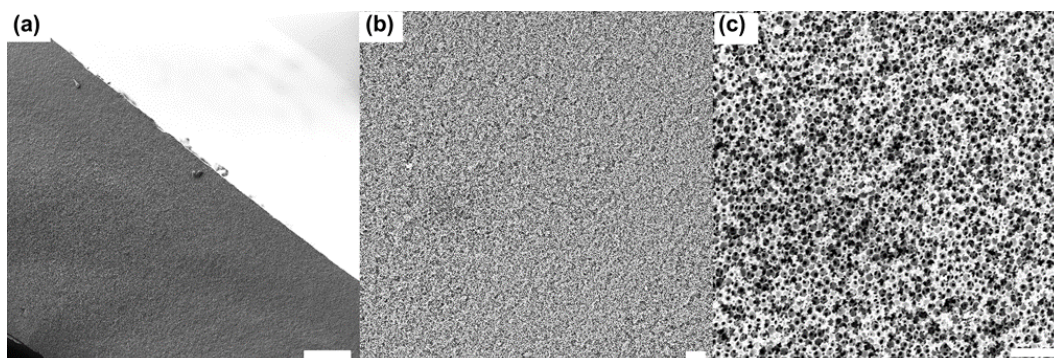


**Figure 4.3 - 12. SEM images taken at different magnifications for one porous carbon material showing the crack-free, homogeneous character of the monoliths; (a) scale bar = 100  $\mu\text{m}$ , (b) scale bar = 2  $\mu\text{m}$ , (c) scale bar = 1  $\mu\text{m}$ .**

From the SEM images taken at different magnifications shown in Figure 4.3 - 12, this second try in modifying the synthesis route is a fundamentally different approach compared to the classical infiltration method described in section 4.3.1. The porous structures show no long-range order. Domains and grain boundaries are missing as well. In the zoom in image of the porous carbon (Figure 4.3 - 13), it can be seen that large pores are interconnected by small pores. The structures obtained from the current route distinguished themselves probably due to the presence of  $\text{Na}_2\text{CO}_3$ . Glassy packing structures can be obtained by adding electrolyte into the colloidal dispersions, as discussed in section 4.1 previously. Here, firstly a glassy state of PS spheres was firstly formed and then replicated as a porous carbon structure.

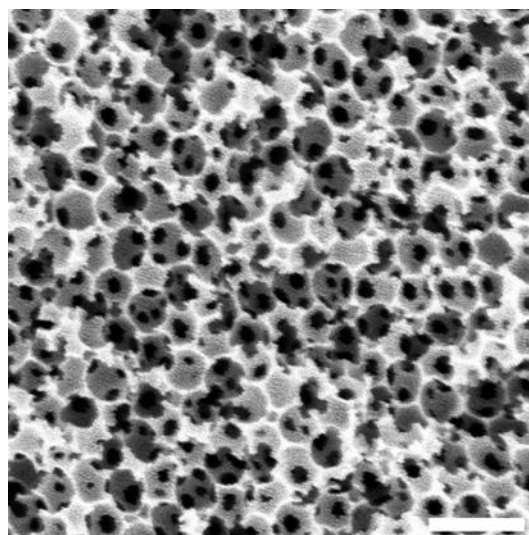


**Figure 4.3 - 13. SEM image indicating the interconnection between the pores. Scale bar = 400 nm.**

The pore size of the carbon monolith can be conveniently tuned by using different sizes of the PS template in the co-assembly process. Figure 4.3 - 14 shows the SEM images of monolithic porous carbon samples synthesized from PS latex spheres with diameter of 110 nm, 250 nm and 500 nm respectively. Based on the estimates from SEM images, an average pore

spacing of 40 nm was obtained in the monolith shown in Figure 4.3 - 14a, 180 nm in Figure 4.3 - 14b, and 420 nm in Figure 4.3 - 14c. This shrinkage in size from PS template to the resulting pores is due to carbonization described above. The resulting pore size depends linearly on  $d_{PS}$  (Figure 4.3 - 15) so that a full control over the porosity of the porous carbon monoliths can be achieved.

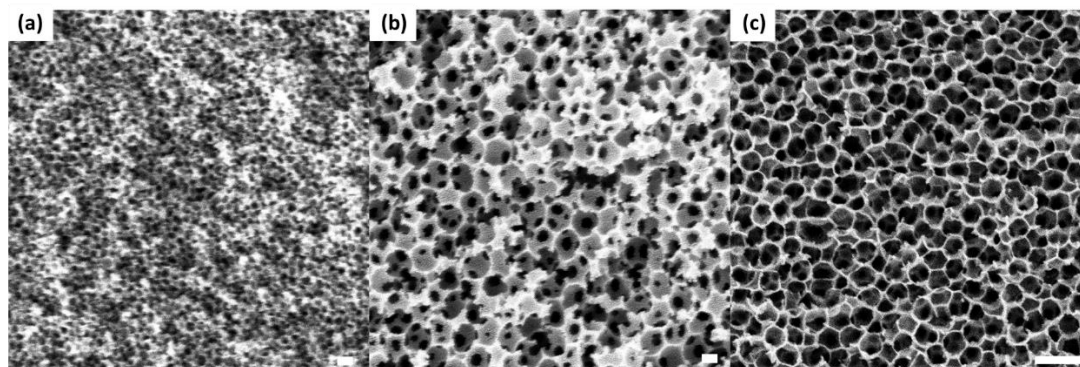


**Figure 4.3 - 14. SEM images of porous carbon monoliths with different pore-size controlled by means of the size of the polystyrene latex particles as templates; (a)  $d_{pore} = 40$  nm, scale bar = 100 nm; (b)  $d_{pore} = 180$  nm, scale bar = 100 nm; (c)  $d_{pore} = 420$  nm, scale bar = 1000 nm.**

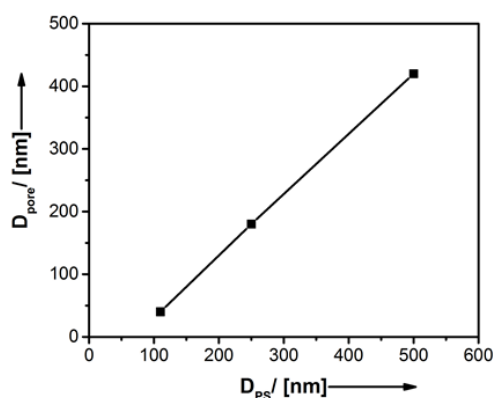


**Figure 4.3 - 15. Correlation of pore-size in porous carbon with PS template size.**

The porous structure has also been characterized by  $N_2$  physisorption. A high accessible pore volume (e.g.  $V_{pore} = 0.87 \text{ cm}^3\text{g}^{-1}$ ) and high accessible specific surface area (e.g.  $A_{spec} = 770 \text{ m}^2\text{g}^{-1}$ ) were found (Figure 4.3 - 16). However, it is not possible to get a pore size distribution from  $N_2$  physisorption as the pore sizes under investigation are too large compared to the size range at which  $N_2$  physisorption can give reliable results. In addition, Hg intrusion porosimetry has also been adopted aiming to obtain the pore size distribution of the porous carbon monoliths. In principle, Hg intrusion porosimetry should be an ideal method to work with the pore sizes present in current work. But the pore sizes we obtained from Hg intrusion porosimetry

deviated a lot to much smaller sizes, compared to the observation from SEM. Two possible reasons might be proposed for this deviation. Firstly, the porous carbon monoliths were compressed a lot during the Hg intrusion due to the high pressure up to 207 MPa, giving a much smaller pore size distribution. When other porous monoliths, e.g. Silica Alumina, were tested, the monolithic samples collapsed after the Hg intrusion because of the high pressure. But our carbon monoliths retained their monolithic shape even after the Hg intrusion. Therefore, a compression of the pores in the carbon monoliths is assumed. Secondly, the amount of the carbon monolith samples is not sufficient enough to avoid the errors in the measurement. Normally the sample should occupy 1/3 of the test tube. This amount is not a problem for most samples in powder but for our case a great difficulty.

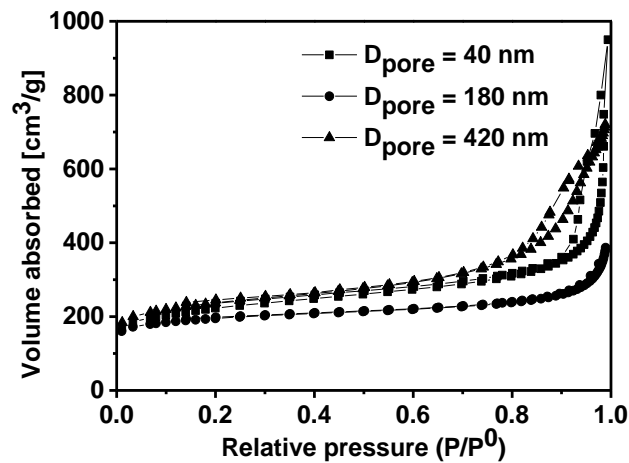


Figure 4.3 - 16. N<sub>2</sub> physisorption isotherms.

It is important to note that only sufficiently high concentrations of resorcinol/formaldehyde in the aqueous dispersion can lead to materials with a dense packing of pores. At too low concentrations, domains of pores created by the PS spheres as templates are separated by larger, irregular voids (Figure 4.3 - 17b,c).

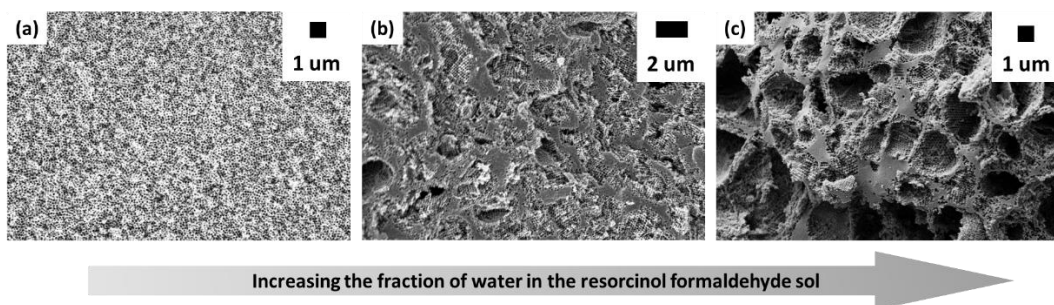
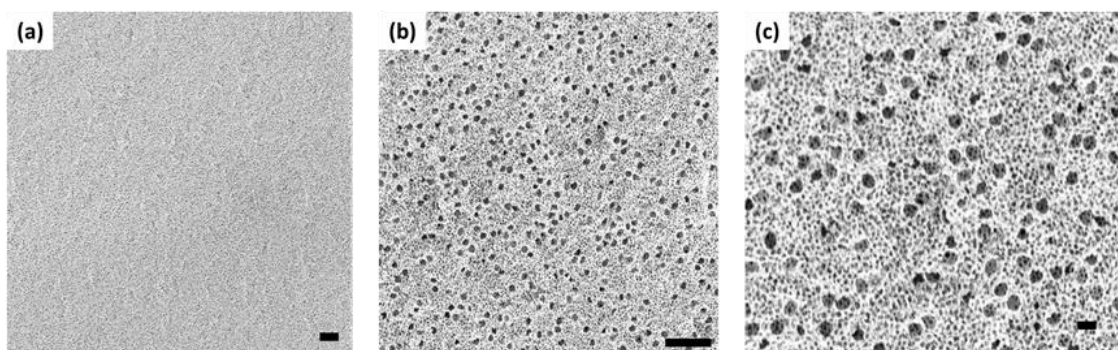


Figure 4.3 - 17. SEM images of a nanoporous carbon material prepared at too low RF concentration (b,c).

By combining the second synthesis route of porous carbon with the gradient control over different separation conditions of binary colloidal systems achieved in previous section 4.2, it should be promising to obtain gradient porous carbon monoliths with limited defects. In section 4.2, a lot of variable parameters which can influence the obtained separation scenarios, including centrifugation force ( $F$ ), centrifugation time ( $t$ ), column length ( $L$ ), total volume fraction of particles ( $\Phi$ ) and number ratio of two particles ( $N = N_{PS1} / N_{PS2}$ ) have been discussed (see section 4.2.2). Through the characterization of analytical ultracentrifugation (AUC), the number of variable parameters can be reduced to two (i.e.  $\Delta r / L$  and particle number ratio  $N$ ). In current work, the RF sol instead of water was used as solvent whose viscosity is changing over time during the centrifugal process. Therefore, the system is much more complex than the one in section 4.2 with water as the solvent. So in this part of work, all the centrifugation conditions ( $\Delta r / L$ ) were fixed. Instead, the number ratio of the particles (see experimental part) was varied in a subtle way to obtain different separations scenarios.

With the binary mixture PS spheres ( $d_{PS} = 110, 250 \text{ nm}$ ) as templates, one scenario that the large pores are randomly scattered in the matrix of the small pores (Figure 4.3 - 18) has been found.



**Figure 4.3 - 18. SEM images at different magnifications for the scenario of a carbon material with bimodal porosity and random mixing of two pore-sizes. (a) scale bar =  $2 \mu\text{m}$ ; (b) scale bar =  $1 \mu\text{m}$ ; (c) scale bar =  $200 \text{ nm}$ .**

The other extreme is given by sharp separation between small and large PS spheres. As a result, a porous carbon material with a distinct boundary between large and small pores was observed and shown in Figure 4.3 - 19.

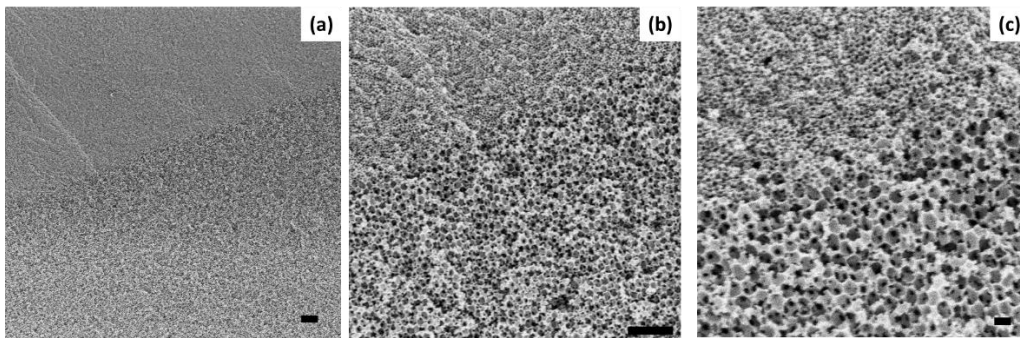


**Figure 4.3 - 19.** SEM images at different magnifications for the pore-system with a sharp separation. (a) scale bar = 2  $\mu\text{m}$ ; (b) scale bar = 1  $\mu\text{m}$ ; (c) scale bar = 200 nm.

Reflecting to the different separation conditions presented in section 4.2, between full mixing and sharp separation, another binary system with gradient pore systems was also achieved (Figure 4.3 - 20).

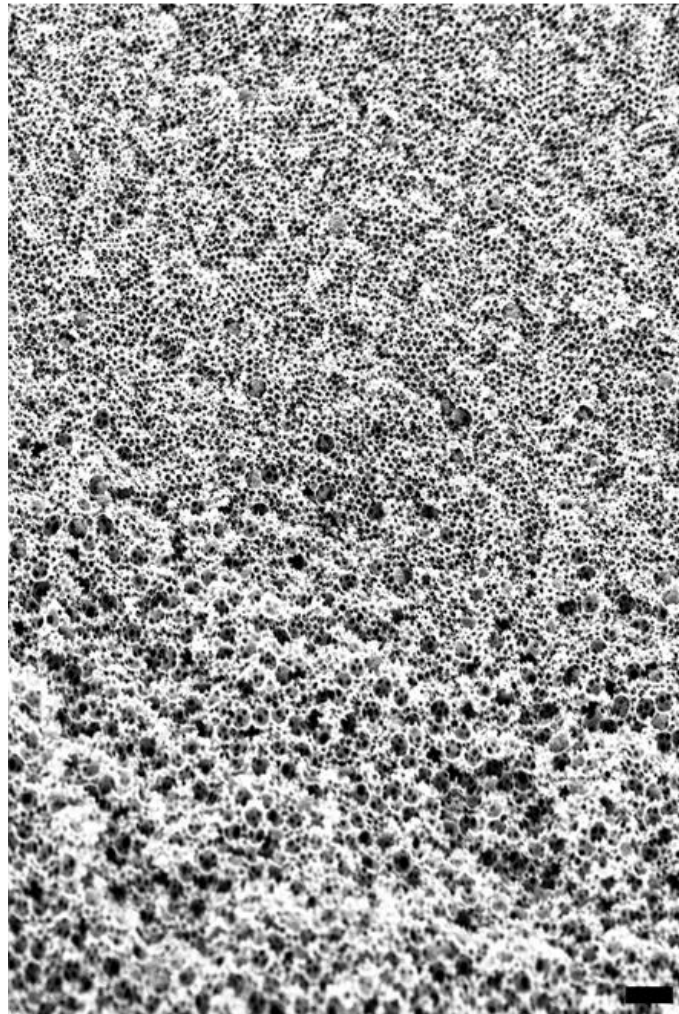


**Figure 4.3 - 20.**<sup>124</sup> SEM image of carbon material with gradient porosity  $d_{\text{pore}} = 180 \rightarrow 420$  nm prepared from a binary mixture of latex particles ( $D_{\text{PS}} = 250, 500$  nm) as templates. Scale bar = 1  $\mu\text{m}$ .

To further expand the gradient, a ternary mixture of template particles ( $d_{PS} = 110, 250, 500$  nm) has been used to create the porous structure (Figure 4.3 - 21). The top one is characterized by a porous matrix only with 40 nm pores. Downwards is followed by a region with some, randomly distributed 180 nm pores. The amount of the 180 nm pores then becomes higher, till eventually 40 nm pores vanish, and at the same time 420 nm large pores show up.

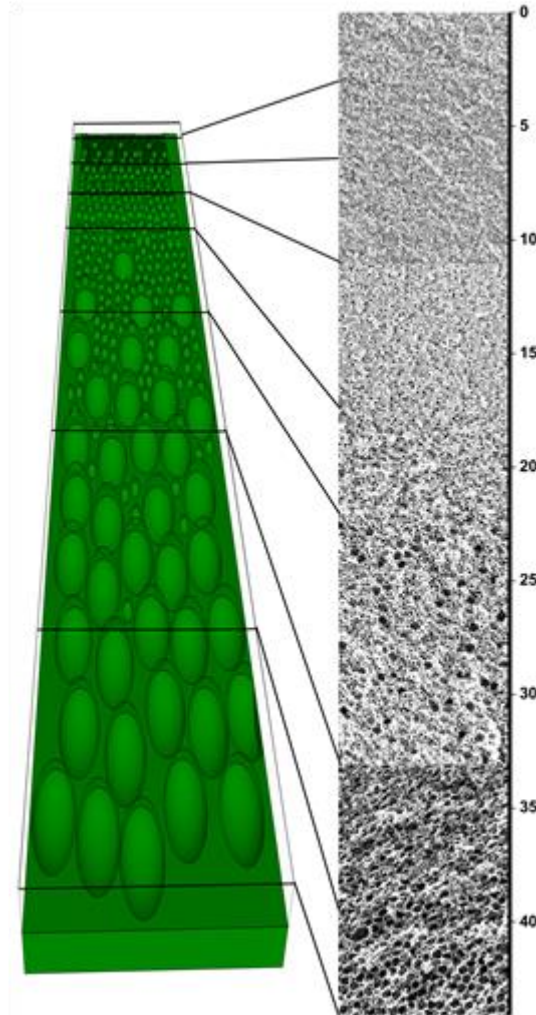


**Figure 4.3 - 21.**<sup>124</sup> 4 x consecutive SEM micrographs of a porous carbon with ternary gradient porosity; scale bar (plotted as a y-axis) units in  $\mu\text{m}$ . And a scheme pointing out the gradient porosity.

#### 4.3.3 The role of the pore size directionality in a battery application

Diffusive and convective transport phenomena are always important subjects in porous media. The porous carbon as a body consisting of a solid matrix allows mass transfer and fluid flow through itself. One of the practical porous-carbon-based systems which concerns the mass transfer characteristics is the Lithium- $\text{O}_2$  ( $\text{Li-O}_2$ ) battery with a much higher theoretical specific energy density than the lithium-ion battery.<sup>127-128</sup> In a  $\text{Li-O}_2$  battery, the chemical and electrical

energy are converted via a reversible reaction of lithium and  $O_2$  ( $2Li + O_2 \leftrightarrow Li_2O_2$ ,  $E^0 = 2.96$  V vs  $Li/Li^+$ ). Li *et al*<sup>129</sup> recently developed a two dimensional model to simulate the mass transfer characteristics in the cathode of the Li- $O_2$  battery. It was found that the capacity of a Li- $O_2$  battery could be increased by adopting a unique designed carbon cathode with a non-uniform porosity distribution and an increasing porosity at the electrolyte /  $O_2$  interface. Olivares-Marín *et al*<sup>130</sup> did a systematical work on the effects on the different macropore sizes of the porous carbon cathode and found out that smaller macropores favor a better charge-discharge reversibility while large macropores contribute to a large capacity. From this work, more advanced dual porosity materials which integrate the advantages of smaller and larger macropore sizes are called for to give a better performance of the Li- $O_2$  battery. It can be concluded that the carbon materials described above with gradient porosity are promising candidates for testing their performance in the Li- $O_2$  battery.

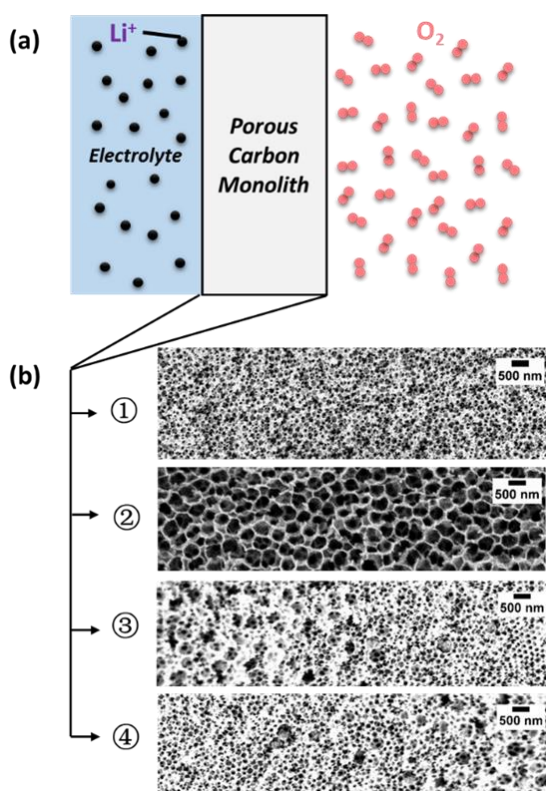


**Figure 4.3 - 22. (a) scheme of a Li- $O_2$  battery cathode part showing the position of the porous carbon monolith in the Li- $O_2$  battery testing setup. (b) SEM image of the four different tested porous carbon samples.**

Four different porous carbon samples were tested as the cathode of Li- $O_2$  cells. Figure 4.3 - 22a is a scheme of a Li- $O_2$  battery cathode part. One side of the porous carbon cathode faces the  $O_2$  environment and the other side faces the separator which is saturated with electrolyte. Figure 4.3 - 22b shows the SEM images of the four different porous structures with the left and right ends of the images corresponding to the electrolyte and  $O_2$  environment respectively. Sample 1 and sample 2 have uniform pore sizes 180 nm and 420 nm. Sample 3 has a gradient porosity and stacked in the Li- $O_2$  cell in a way that the 180 nm pores facing the  $O_2$  environment. Sample 4 has the opposite porosity gradient compared to sample 3.

The discharge curves and cycling performances of Li- $O_2$  cells at the current density of 50 mA/g are shown in Figure 4.3 - 23a and Figure 4.3 - 23b. The uniform porous carbon cathode with 180 nm in pore size (sample 1) showed the lowest specific capacity around 500 mAh/g while the larger 420 nm pores (sample 2) delivered a higher specific capacity. The trend

of an increasing specific capacity with the increasing pore size coincide with some preliminary works.<sup>130-131</sup> When assembling the gradient porous carbon monolith in the Li-O<sub>2</sub> battery in a way that the smaller pores facing the O<sub>2</sub> side (sample 3), larger specific capacity has been achieved compared to the uniform large pore case. The largest discharge capacity was observed by turning the carbon monolith conversely making the smaller pores facing the electrolyte side (sample 4). By increasing the pore size in the cathode, the oxygen transport can be enhanced and thus the discharge capacity can be improved, but meanwhile the specific surface area is reduced which could on the other hand limit the discharge capacity. This explains why the combination of two pore sizes in the cathode could provide overall larger capacity than uniform pores. In addition, it can be clearly seen that the direction of the gradient in the porous carbon cathode has a great impact on the discharge capacity. With the larger pores at the oxygen side (sample 4), the largest capacity can be delivered. The porosity close to the oxygen side is more important as all the consumed oxygen in the cathode is supplied from this side. The cathode with a higher porosity at the oxygen side utilized the pores deep inside in a better way because of the more efficient oxygen transfer from the oxygen environment.

Figure 4.3 - 23b reveals the cycling performance of the porous carbon cathodes. Compared with cathode made of uniform pores, larger capacity can be maintained by cathode with gradient porous structures. Different from the discharge property, the cathode with a lower porosity at the oxygen side (sample 3) had a better cycling performance. The cross section of the four different porous carbon monoliths which were tested as the cathode in Figure 4.3 - 23 were further examined after cycling measurements.

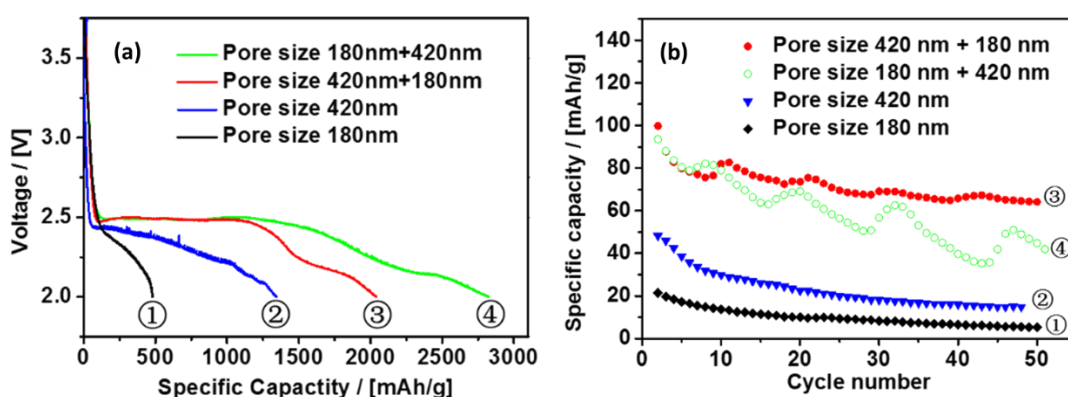


**Figure 4.3 - 23. The discharge curves (a) and cycling performances (b) of Li-O<sub>2</sub> cells at the current density of 50 mA/g. The four samples correspond to the samples in Figure 4.3 - 22.**

In general, after cycling measurements the 180 nm pores remained interconnected but much deposit of the solid product Li<sub>2</sub>O<sub>2</sub> can be found inside the 420 nm pores and mostly block

the pores (Figure 4.3 - 24). This explains the low capacity of sample 1 with 180 nm pores. The latter result shows the  $\text{Li}_2\text{O}_2$  deposit can also be an important factor. When the pore entrances are blocked, mass transport through the electrode is aggravated. The block of pores impedes to reach the maximum capacity.

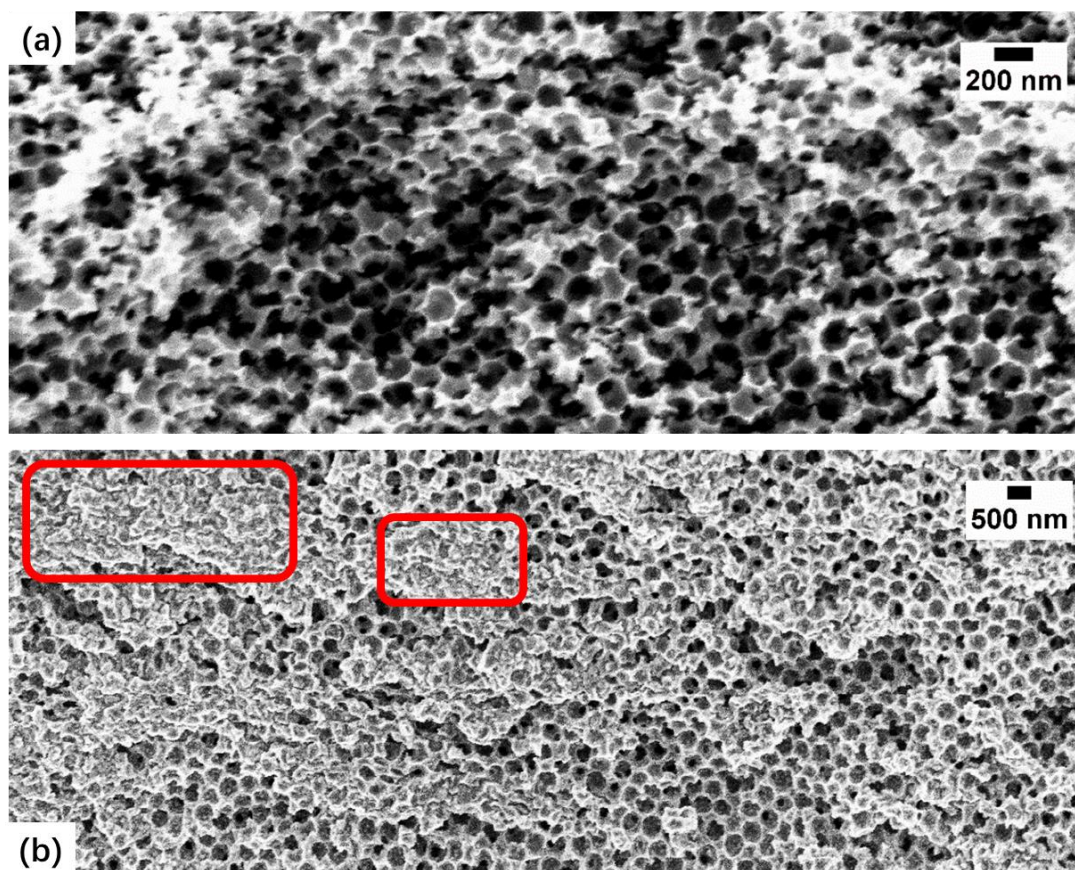


**Figure 4.3 - 24.** After discharge, the 180 nm pores (a) remained interconnected but much deposit of the solid product  $\text{Li}_2\text{O}_2$  can be found in 420 nm pores (b indicated by red squares) in general.

Therefore, a material with two different pores could optimize the performance. One type of pore (180 nm) will be not filled so quickly granting prolonged mass transport, while the other type of pore (420 nm) will contribute to capacity via  $\text{Li}_2\text{O}_2$  deposition. The two ends of sample 3 were examined by SEM and confirmed this assumption (Figure 4.3 - 25).

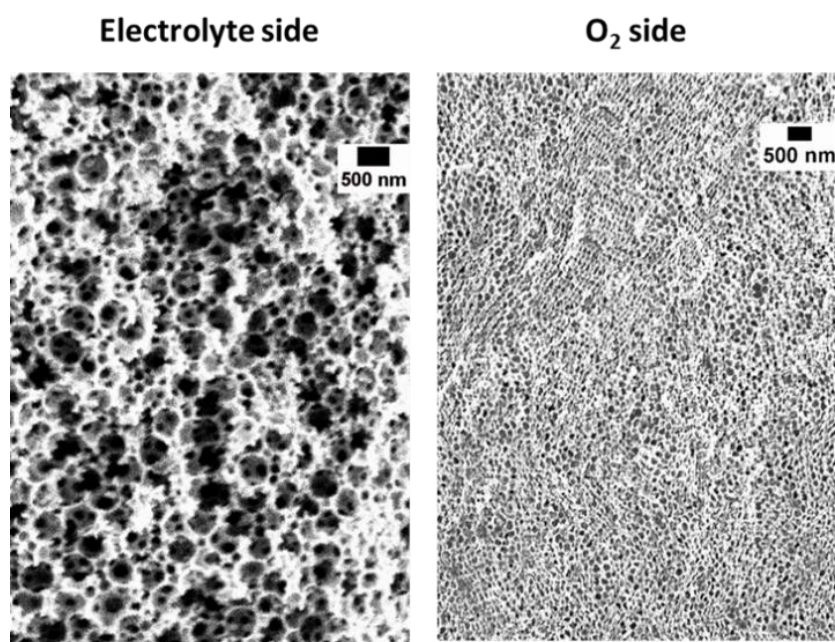


**Figure 4.3 - 25. SEM images of Sample 3 in Figure 4.3 - 22 after cycling measurement.**

However, it is more interesting to test if the capacity depends on how gradient porous carbon is positioned. Clearly sample 4 has an even higher capacity than sample 3 at first discharge. Considering the previous arguments this behavior can be understood by the larger amount of deposited  $\text{Li}_2\text{O}_2$ . When the large pores are facing the oxygen side one can see the pores are filled homogeneously with  $\text{Li}_2\text{O}_2$  indicating that a large fraction of the surface of the porous material has contributed to the electrochemical reaction (see Figure 4.3 - 26). The smaller pores in the gradient zone and those pointing to the electrolyte remain unfilled, and this secures mass transport in the electrode. Compared to reports in the literature,<sup>132</sup> further development is needed to reach maximum capacities.

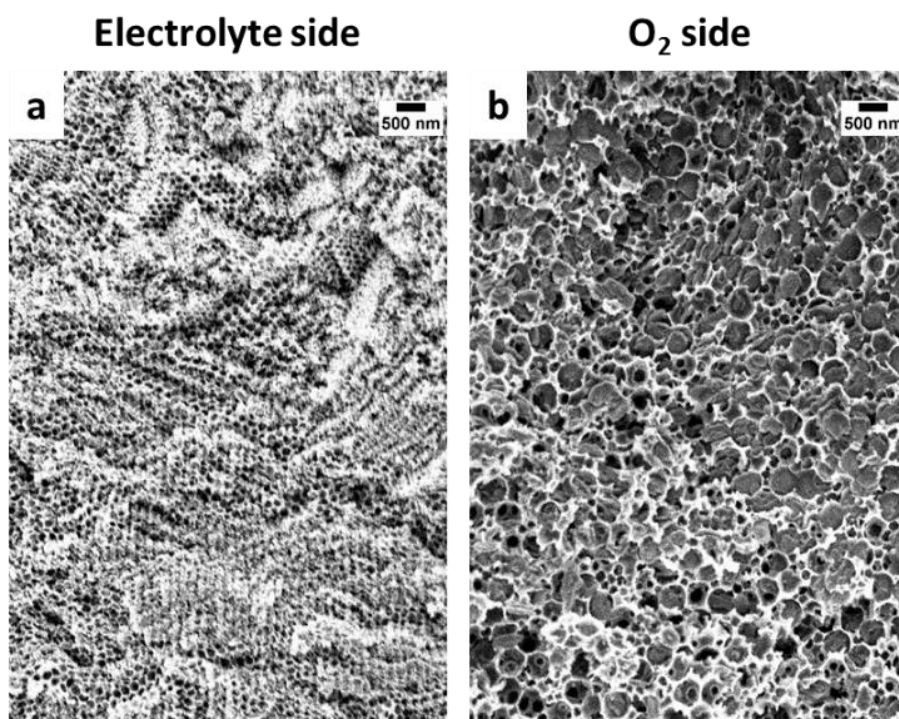


Figure 4.3 - 26. SEM images of Sample 4 in Figure 4.3 - 22 after cycling measurement.

## 5. Summary and outlook / Zusammenfassung und Ausblick

### 5.1 Summary

With the aid of analytical ultracentrifugation, this thesis has demonstrated that the assembly of colloidal systems can be directed by a centrifugal field in a controlled way. By applying centrifugal force to monodisperse, binary and even ternary colloidal systems, different structures and materials with potential application functions emerged.

In chapter 4.1, the influence of adding electrolyte  $\text{CaCl}_2$  to monodisperse charge stabilized polystyrene colloidal systems was firstly investigated via methods like zeta potential measurement and DLVO stability calculations. A satisfactory correlation with the observed colloidal packing could not be obtained from these conventional methods, which always predicted more stability than the reality. Alternatively, dynamic light scattering, analytical ultracentrifugation and asymmetrical flow field flow fractionation were incorporated to characterize the colloidal particle size distribution in the presence of different amounts of  $\text{CaCl}_2$ . From this combined analysis, the colloidal systems' stability and the formation of different particle oligomers were successfully correlated to the corresponding macroscopic colloidal packing structures. The analysis with analytical ultracentrifugation exhibits a defined species which appeared denser than the monomer particles and became pronounced when the concentration of  $\text{CaCl}_2$  increased to a certain threshold. This threshold concentration can be found by dynamic light scattering. Different oligomers of polystyrene colloidal spheres were formed when the amount of  $\text{CaCl}_2$  was above this threshold. To avoid the formation of the oligomers and to realize a random close-packed colloidal packing, the amount of  $\text{CaCl}_2$  should be limited to the threshold. Furthermore, the random colloidal packing was triggered by centrifugal force and very well preserved on a macroscopic scale by trapping the random structure in a polyacrylamide hydrogel. Photon time-of-flight spectroscopy (TOPFS) allowed us to characterize the quality of the samples prepared with different amounts of  $\text{CaCl}_2$  regarding multiple light scattering.

In chapter 4.2, one more component was added to create a binary colloidal system which consists of polystyrene latex spheres with two different sizes. In this part, centrifugal force not only acted as a compaction tool, but fractionated the mixture of polystyrene particles to different structural gradients of the latex composition including different glassy states and also different crystalline structures. With the help of analytical ultracentrifugation as an in-situ

observation technique, a lot of variable parameters which can influence the obtained separation scenarios were reduced to only two parameters. Therefore, the degree of separation of the colloidal particles with different size can be precisely adjusted. Besides the expected thermodynamically most stable structure and glassy states, a large number of different metastable polymorphs varying in stoichiometry were observed side by side in one experiment. Most importantly, very surprising less-dense, low-coordinated structures like Sphalerite occurred, in spite of centrifugation being a process leading to densification. This is an emergent phenomenon resulting from non-equilibrium, dissipative conditions, which are commonly not considered in crystallization theories.

Based on the prior knowledge of chapter 4.1 and 4.2, a robust synthesis route of crack-free porous carbon monoliths with gradient structures was developed from a classical template infiltration route in chapter 4.3. The success lies in the in situ assembly of polystyrene spheres (as templates) and a resorcinol formaldehyde sol (as a carbon precursor) using ultracentrifugation. With this method, the capability of flexibly tuning the porosity was demonstrated by using different templates. The resulting carbon monoliths with gradient porosity were tested as electrodes in the Li-O<sub>2</sub> cell. It was proven that not only the gradient structure influences the performance of the cell, but also the direction of the gradient is of great importance. The cathode which had an increasing porosity toward the oxygen side delivered a larger capacity than the cathode with an opposite gradient due to the more efficient oxygen transfer from the oxygen environment to the electrolyte side of the cathode. But regarding the cycling performance, the cathode which had a decreasing porosity toward the oxygen side was better, owing to the better retention of the surface area by the smaller pores at the oxygen side.

It can be concluded that the approaches presented in this thesis open up a new platform to fundamentally study the colloidal assembly and establish a starting point for the synthesis of gradient materials with potential application functionalities.

-----

In dieser Arbeit wurde mithilfe analytischer Ultrazentrifugation gezeigt, dass die Zusammenlagerung in kolloidalen Systemen durch ein Zentrifugalfeld kontrolliert gesteuert werden kann. Durch Anwenden von Zentrifugalkraft auf monodisperse, binäre und ternäre Kolloidsysteme bildeten sich verschiedene Strukturen und Materialien mit potentiellen Anwendungsmöglichkeiten heraus.

In Kapitel 4.1 wurde zuerst der Einfluss der Hinzugabe von  $\text{CaCl}_2$  auf monodisperse, ladungsstabilisierte Polystyrolkolloide mit Methoden wie Zeta-Potentialmessungen und DLVO-Stabilitätsberechnungen untersucht. Eine zufriedenstellende Vergleichbarkeit mit der tatsächlich beobachteten kollektiven Kugelpackung kann mithilfe dieser konventionellen Methoden nicht erhalten werden, da die vorausgesagte Stabilität sich immer größer als die beobachtete erwies. Als Ersatzmethoden wurden dynamische Lichtstreuung, analytische Ultrazentrifugation und asymmetrischer-Fluss-Feld Fluss-Fraktionierung hinzugezogen, um die Größenverteilung der Kolloide bei Anwesenheit verschiedener  $\text{CaCl}_2$ -Konzentrationen zu charakterisieren. Mit dieser Kombinationsanalyse konnten die Stabilität der Kolloidsysteme und die Bildung verschiedener Oligomere mit den Beobachtungen der jeweiligen makroskopischen Anordnungen der Strukturen in Übereinstimmung gebracht werden. Die Analyse mit analytischer Ultrazentrifugation lässt eine definierte Spezies erkennen, die dichter erschien als die monomeren Partikel und insbesondere deutlich hervortrat, wenn die  $\text{CaCl}_2$ -Konzentration einen bestimmten Grenzwert erreichte. Dieser Grenzwert kann mittels dynamischer Lichtstreuung ermittelt werden. Überschreitet die Menge an  $\text{CaCl}_2$  dieses Limit, bilden sich verschiedene Oligomere aus kugelförmigen Polystyrolkolloiden. Um eine Bildung von Oligomeren zu vermeiden und so eine ungeordnete dichte Packung zu erreichen, sollte die  $\text{CaCl}_2$ -Menge auf diesen Grenzwert beschränkt werden. Weiterhin entstand eine ungeordnete dichte Kugelpackung durch Zentrifugalkraft und blieb auf makroskopischer Ebene sehr gut erhalten, indem die Zufallsstruktur in einem Polyacrylamid-Hydrogel eingefangen wurde. Messungen mittels Photonenflugzeitspektroskopie (TOPFS) ermöglichten es, die Qualität der Proben hinsichtlich Mehrfachlichtstreuung zu untersuchen.

In Kapitel 4.2 wurde eine zusätzliche Komponente hinzugefügt um ein binäres Kolloidsystem herzustellen, das aus Polystyrolkugeln zweier unterschiedlicher Größen bestand. In diesem Teil wurde die Zentrifugalkraft nicht nur als Verdichtungswerkzeug verwendet, sondern fraktionierte die Teilchenmischung auch zu verschiedenen Gradienten hinsichtlich der Konzentrationsverteilung der Komponenten, einschließlich unterschiedlicher glasartiger Zustände und kristalliner Strukturen.

Mithilfe der analytischen Ultrazentrifugation als in-situ Beobachtungstechnik wurden viele variable Parameter, die die erhaltenen Trennungsszenarios beeinflussen können, auf zwei Parameter reduziert. Daher kann der Trennungsgrad der Kolloide unterschiedlicher Größe genau angepasst werden. Neben den erwarteten, thermodynamisch stabilsten Strukturen und glasartigen Zuständen wurden eine große Anzahl verschiedener metastabiler Polymorphe mit variierender Stöchiometrie in einem Experiment nebeneinander beobachtet. Insbesondere

traten Strukturen mit überraschend niedriger Dichte und Ordnung wie Sphalerit auf, obwohl es sich bei der Zentrifugation um einen Prozess handelt, der zu Verdichtung führen sollte. Dieses Phänomen taucht in Folge dissipativer Nichtgleichgewichtsbedingungen auf, die gewöhnlicherweise nicht in Kristallisationstheorien berücksichtigt werden.

Auf dem Wissen aus Kapitel 4.1 und 4.2 aufbauend, wurde in Kapitel 4.3 eine robuste Syntheseroute für rissfreie, poröse Kohlenstoffmonolithe mit Gradientenstruktur aus einer klassischen Templatinfiltrationsroute entwickelt. Hierbei liegt der Erfolg im in-situ Zusammenbau von Polystyrolpartikeln (als Template) und einem Resorcin-Formaldehyd-Sol (als Kohlenstoff-Precursor). Die entstandenen Kohlenstoffmonolithe mit Gradientenporosität wurden als Elektroden einer Li-O<sub>2</sub>-Zelle getestet. Es konnte gezeigt werden, dass nicht nur die Gradientenstruktur, sondern auch die Richtung des Gradienten von großer Bedeutung ist. Die Kathode mit steigender Porosität zur Sauerstoffseite hin ermöglichte aufgrund des effizienteren Sauerstofftransfers eine größere Kapazität als die Kathode mit einem entgegengerichteten Gradienten. Die Kathode mit sinkender Porosität in Richtung Sauerstoffseite wies allerdings eine höhere Zyklenzahl auf. Dies ist dem besseren Erhalt der Kathodenoberfläche aufgrund der kleineren Poren geschuldet.

Zusammengefasst eröffnen die Ansätze dieser Arbeit eine neue Grundlage um die Zusammenlagerung von Kolloiden zu untersuchen und markieren einen Startpunkt für die Herstellung von Gradientenmaterialien mit potentiellen Anwendungsmöglichkeiten.

## 5.2 Outlook

Although the polystyrene particle has a relatively low refractive index, the well-established synthesis route of polystyrene latex particle with various particle sizes should be able to provide a nice experimental basis for the study of light diffusion behavior in random media. In the future work, TiO<sub>2</sub> or ZnO either in the colloidal particle form or as an inverse structure, can be explored as alternative materials for polystyrene to explore the ideal 3D materials for the observation of light localization.

A stimulating question arises from the binary colloidal system in chapter 4.2, i.e. if besides packing factors and preference for coordination geometry also non-equilibrium, systemic features could influence the result of kinetically controlled crystallization process not only at the colloidal but also on the atomic scale. Even for a fixed size ratio of the particles, several polymorphs can form parallel to each other in the initial periods of a crystallization process. Indeed, for CaCO<sub>3</sub>, it was recently found that several nucleation pathways are simultaneously

operative.<sup>133</sup> The analytical power of AUC can be further explored to obtain deeper understanding of the colloidal assembly, for example, by adding different UV-Vis markers to differently sized nanoparticles.

More than the Li-O<sub>2</sub> battery which has been shown in chapter 4.3, the transport of matter, charge carriers or energy in a preferential direction is important for many applications. There are theoretical works showing that a silicon inverse opal exhibits a remarkable increase in the figure of merit for thermoelectric energy conversion.<sup>134</sup> Furthermore, the reduction in lattice thermal conductivity of porous materials has been predicted to be related to pore size distribution.<sup>135</sup> Thus, the gradient porous carbon prepared in chapter 4.3 is a promising candidate to provide experimental insights into the thermal conductivity of nanoporous media.

## 6. Experimental part

### 6.1 Materials and preparation methods

#### 6.1.1 Synthesis of polystyrene spheres via emulsifier free emulsion polymerization<sup>136-137</sup>

Monodisperse, negatively charged polystyrene spheres were synthesized by emulsion polymerization using a jacketed cylindrical reaction vessel, connected to a reflux condenser and a glass stirrer powered by mechanical stirring. The vessel also contained a temperature sensor and an Ar/reagent inlet. The temperature was maintained through the jacket with the use of a circulating temperature bath. Styrene was distilled prior to use. Sodium styrene sulfonate, sodium persulfate, sodium sulfite and sodium hydrogen carbonate were used as received. The resulting dispersion was passed through filter paper and purified by exhaustive dialysis with 15000-MW cut off (MWCO). Dialysis was carried out in 1 L beaker of water which was changed daily until conductivity remains constant. The determination of the solid content of the dispersion is performed by gravimetry.

##### 6.1.1.1 Polystyrene spheres with 110 nm and 150 nm in diameter

168 mL deionized water and 62 mL styrene were added into preheated reaction vessel ( $T=65^{\circ}\text{C}$ ). After the mixture of water and styrene being stirred (330 rpm) for 5min, sodium styrene sulfonate (varied amount) dissolved in 10 mL water was added. And subsequently 0.358 g sodium persulfate dissolved in 10 mL water was added. After 24 h the reaction was stopped. Over the entire period the reaction mixture was flushed with Ar. The resulting dispersion was passed through filter paper and purified by dialysis tubing. The amount of sodium styrene sulfonate for producing 110 nm spheres in diameter is 0.4 g while 0.3 g for 150 nm spheres in diameter.

##### 6.1.1.2 Polystyrene spheres with 250 nm and 300 nm in diameter

75 mL deionized water and 20 mL styrene were added into the preheated reaction vessel ( $T = 80^{\circ}\text{C}$ ). After the mixture of water and styrene being stirred (260 rpm) for 5min, sodium styrene sulfonate (varied amount) dissolved in 5 mL water was added. After 30 min 0.116g sodium hydrogen carbonate dissolved in 5 mL water and 0.088 g sodium sulfite dissolved in 5 mL water were added. At last 0.186 g sodium persulfate dissolved in 10 mL water was added. After 180 min the reaction was stopped. Over the entire period the reaction mixture was flushed with Ar. The resulting dispersion was passed through filter paper and purified by dialysis tubing.

The amount of sodium styrene sulfonate for producing 250 nm spheres in diameter is 0.031 g while 0.020 g for 300 nm sphere in diameter.

#### 6.1.1.3 Polystyrene spheres with diameter above 300 nm

When the desired size of the polystyrene particles is above 300 nm, one step synthesis can hardly provide good monodispersity. For the preparation of polystyrene spheres with a diameter larger than 300 nm, a seed-growth method<sup>138</sup> was adopted. To prepare the polystyrene with diameter of 500 nm, 10 ml dispersion consisting of 10 w.t% 300 nm polystyrene spheres (seed) was firstly mixed with 40 ml water and 5.8 ml styrene. After being stirred (260 rpm) for 5 min, 0.094 g sodium sulfite dissolved in 5 mL water and 0.027 g sodium persulfate dissolved in 5 mL water were added. After 24 h the reaction was stopped. Over the entire period the reaction mixture was flushed with Ar and kept at  $T = 60^{\circ}\text{C}$ . The resulting dispersion was passed through filter paper and purified by dialysis tubing.

#### 6.1.2 Assembly of monodisperse colloidal system in the presence of extra electrolytes

0.18 M  $\text{CaCl}_2$  (>90%, Merck) aqueous solution was prepared and used as stock electrolyte. For zeta potential, dynamic light scattering and analytical ultracentrifugation measurements, diluted polystyrene and  $\text{CaCl}_2$  mixtures were used. DLVO calculation was performed using the Hamaker software package<sup>139</sup>.  $\text{CaCl}_2$  aqueous solution was added to concentrated (10% w.t.) polystyrene dispersions to investigate the aggregation of the particles via scanning electron microscopy. To fabricate a free-standing monolith with glassy colloidal packing, a hydrogel precursor with a composition of acrylamide (>99%, Acros), N, N'-Methylenebisacrylamide (>99%, Sigma Aldrich) and water (MiliQ) was used. Firstly, the hydrogel precursor, polystyrene dispersions and certain amount of  $\text{CaCl}_2$  were mixed in a centrifuge tube and centrifuged with the L-70 ultracentrifuge (Beckman instruments, Inc.) using the Beckman swing out rotor SW 55 Ti. Polyallomer centrifuge tubes (Beckman instruments, Inc.) were used and all centrifuge experiments were run at small centrifugal force  $F = 120\text{ g}$  to avoid the possible quenching by centrifugal force. The centrifugation process was conducted at a temperature of 298 K. After centrifugation, a polystyrene-polyacrylamide composite was obtained in-situ inside the centrifuge tube by adding N, N, N', N'-Tetramethylethane-1,2-diamine (>99%, Sigma Aldrich) and ammonium persulfate (>98%, Sigma Aldrich). For detailed parameters see the tables in Table 6 - 1. The polystyrene-polyacrylamide composite can be cut into the desired shape and dried to obtain the monolith which is suitable for optical measurements.

**Table 6 - 1. Detailed parameters for the preparation of free-standing monolith with glassy colloidal packing.**

	Monolith in Figure 4.1 - 14b	Monolith in Figure 4.1 - 14c
CaCl <sub>2</sub> aqueous solution (0.18 M) / ml	0.02	0.04
Aqueous acrylamide solution (40% w.t. %) / ml	0.18	0.18
Aqueous N, N'-Methylenebisacrylamide solution (2% w.t.%) / ml	0.16	0.16
MilliQ water /ml	0.04	0.02
Polystyrene suspensions (10% w.t.%) / ml	0.4	0.4

After the centrifugation, 0.01 ml N, N, N', N'-Tetramethylethane-1,2-diamine (>99%) and 0.01ml ammonium persulfate aqueous solution (10% w.t.) were added to the centrifuge tube to initiate the polymerization of acrylamide.

### 6.1.3 Assembly of binary colloidal system between chaos and order

Binary colloidal structures of 150 nm (PS1) and 300 nm (PS2) latexes were fabricated with the L-70 ultracentrifuge (Beckman instruments) using the Beckman swing out rotor SW 55 Ti and ultra clear™ (5×41mm) centrifuge tubes to maintain sedimentation as undisturbed as possible. Specific parameters for different cases can be found in Table 6 - 2. After centrifugation, the remaining solvent at the top of the centrifuge tube was removed before the centrifuge tube was placed in a desiccator over silica gel for drying. The resulting structures were examined by cutting the dried samples with a razor blade along the long axis of the sample column, and the direction along the centrifugal force was subsequently investigated via scanning electron microscopy.

**Table 6 - 2. Specific parameters for different binary structures in chapter 4.2**

	Fig. 4.2-5d	Fig. 4.2-5c	Fig. 4.2-5e	Fig. 4.2-5b	Fig. 4.2-8a	Fig. 4.2-8b	Fig. 4.2-11	Fig. 4.2-12	Fig. 4.2-21a	Fig. 4.2-21b
total volume fraction	0.28	0.07	0.16	0.07	0.16	0.16	0.07	0.07	0.16	0.16
Number ratio ( $N_{PS1} / N_{PS2}$ )	3	3	3.3	1.5	3.3	3.3	9	13	3.3	3.3
Column length(mm)	3.4	3.4	3.4	3.4	3.4	3.4	3.4	3.4	3.4	3.4
Centrifugal acceleration	3000g	3000g	3000g	3000g	12000g	120g	3000g	3000g	12000g	12000g/120g
Centrifugal time	53min	16min	18min	14min	18min	18min	17min	17min	20min	20min/5h

#### 6.1.4 Functional porous carbon monoliths: from multinary colloidal assembly to a defined gradient porosity

Resorcinol formaldehyde solution (RF) with a composition of resorcinol (>99%, Sigma Aldrich), formaldehyde (36.5%, Honeywell Riedel-de Haen), sodium carbonate (>99.5%, Sigma Aldrich) and water in a 1 : 3.3 : 0.02 : 10.1 molar ratio was used as the carbon source for the matrix materials. Firstly, by mixing RF solution and PS suspension in the centrifuge tube (detailed parameters see Table 6 - 3), a PS-RF composite was prepared with the L-70 ultracentrifuge (Beckman instruments) using the Beckman swing out rotor SW 55 Ti and Polyallomer (13×51 mm) centrifuge tubes to maintain the centrifugal force parallel to the length of the tube. As the density of PS is smaller than the density of RF, all the PS latex spheres floated to the top of the centrifuge tube forming a packing of the PS spheres with RF filled in the interstices between the PS spheres. The centrifugation was performed at 40 °C, 48608 g and lasted for typically 16 h to assure the RF sol had become a gel before removing the centrifugal force. The PS-RF composite which was located at the top of the sample was then cut from the whole sample body and aged in Duran® laboratory bottles sealed with blue PP screw cap at 85°C for three days followed by drying at 85°C for 1 day in a convection oven. Afterwards, the PS-RF composite was calcined at 900 °C for 2h (heating ramp 5°C min<sup>-1</sup>) in a flow of N<sub>2</sub> to carbonize the RF and at the same time remove the PS spheres. The resulting porous carbon monolith was then slightly polished with 1000-grit sandpaper to remove the possible residue at the surface of the monolith and then treated with ultrasound in MiliQ water.

**Table 6 - 3. Overview of prepared carbon materials and experimental parameters. Latex suspension 1:  $D_{PS} = 110$  nm (9 weight%); latex suspension 2:  $D_{PS} = 250$  nm (10 weight%); latex suspension 3:  $D_{PS} = 500$  nm (5 weight%)**

Sample	Pore-system	Latex suspension 1 / [ml]	Latex suspension 2 / [ml]	Latex suspension 3 / [ml]
Fig. 4.3-14a	mono $d_{pore} = 40$ nm	0.927	-	-
Fig. 4.3-14b	mono $d_{pore} = 180$ nm	-	0.927	-
Fig. 4.3-14c	mono $d_{pore} = 420$ nm	-	-	0.927
Fig. 4.3-18	binary-mix $d_{pore} =$ 180, 420 nm	0.655	0.433	-
Fig. 4.3-19	binary-separated $d_{pore} = 180, 420$ nm	0.633	0.433	-
Fig. 4.3-20	binary-gradient $d_{pore} = 180, 420$ nm	-	0.4	0.527
Fig. 4.3-21	ternary-gradient $d_{pore} = 40, 180, 420$ nm	0.633	0.123	0.123

## 6.2 Characterizations

### ***Dynamic Light Scattering (DLS):***

A Malvern Zetasizer Nano (Malvern Instruments Ltd.) was used to perform dynamic light scattering and zeta potential measurements.

### ***Scanning Electron Microscopy (SEM):***

Scanning electron microscope (SEM) images were acquired from Zeiss 249 CrossBeam 1540XB scanning electron microscope.

### ***Analytical ultracentrifugation (AUC):***

In chapter 4.1, A Beckman Optima XL-I analytical ultracentrifuge was used to measure the sedimentation coefficient of the polystyrene spheres. All the AUC measurements were performed at 298 K with 6 mm thick Ti cells. Interference optics were used.

In chapter 4.2, A Beckman Optima XL-A analytical ultracentrifuge and a UV/Vis multi-wavelength analytical ultracentrifuge<sup>140</sup> developed as an open source instrument<sup>141</sup> were used to measure the sedimentation coefficient of polystyrene spheres. All the AUC measurements were performed at 298 K with 12 mm thick Ti cells.

The data obtained from AUC measurements were evaluated with the public domain software Sedfit (version 14.6e). The  $g^*(s)$  analysis has been used in the to calculate the sedimentation coefficient distribution.

### ***Flow Field-Flow Fractionation (AF4):***

AF4 measurements were conducted with a Wyatt Eclipse Dualtec control unit operating an Agilent Infintiy 1260 pump. A Wyatt "short Channel" (SC) ( $L = 174$  mm,  $b_o = 24$  mm,  $b_L = 4$  mm) equipped with a Nadir Regenerated Cellulose membrane (5 kDa cut-off) was used. A 0.1 % (w/v) solution of SDS and Millipore water was used as eluent. For all measurements a crossflow of  $V_c = 1.5$  ml/min was applied. The effective channel height was determined by a reference measurement of a 200 nm PS spherical standard (Duke Scientific Corporation.). Samples were detected by a chain of a light scattering (Wyatt Dawn Heleos 8+), UV/Vis (Agilent Infinity 1100 DAD-SL) and refractive index (Agilent Infinity 1260) detector. Data evaluation was performed using an inhouse processing software for AF4 data. The signal of the light scattering detector at an  $27^\circ$  angle detector at was chosen to determine the hydrodynamic radii of the single fractions.

***Time of flight measurement:***

Time of flight measurement was conducted in the same way as described elsewhere<sup>85</sup>. A laser fs-pulse is shot on the free standing samples. The multiple scattered photons are collected in transmission with a time-resolved photomultiplier.

***Raman spectroscopy:***

The Raman spectra were performed with a LabRAM HR800 spectrometer (HORIBA Jobin Yvon) with the 532 nm laser line of a frequency doubled Nd:YAG laser. An Olympus MplanN 100× objective lens (NA = 0.90) was used. The spectra were collected in backscattering geometry with a spectral resolution better than 0.3 cm<sup>-1</sup>. The spectrally dispersed Raman signal was detected using a Peltier-cooled CCD camera. The laser power on the sample was tuned to 1 mW.

***Infrared spectroscopy (IR):***

FT-IR spectra were recorded by using a Perkin Elmer Spectrum 100 spectrometer with ATR unit.

***Powder X-ray Diffraction (PXRD):***

Powder X-ray diffraction (PXRD) patterns were acquired using a Bruker D8 Advance.

***Thermogravimetric Analysis (TGA):***

TGA was performed on a Netzsch STA F3 Jupiter setup.

***N<sub>2</sub>-physisorptions:***

N<sub>2</sub>-physisorptions measurements were conducted on a Micromeritics Tristar.

***Electrochemical characterization:***

The galvanostatic discharge measurements were performed with a Swagelok test cell (purchased from X2 Labwares Pte Ltd), in which a monolithic porous carbon, a lithium foil (Goodfellow Inc.) and a glass-fiber (Whatman GF/C) were used as cathode, anode and separator respectively. The electrolyte was prepared by dissolving 1 M LiPF<sub>6</sub> in a mixture of diethyl carbonate and ethylene carbonate (1:1 vol. /vol.). The entire battery was constructed in an argon atmosphere glove box (MBraun 10 compact) with water and oxygen contents below 0.5 ppm. All tests were carried out on Neware battery test system (CT-4008) at room temperature in oxygen atmosphere.

## 7. Abbreviation

### Chemicals

PS	polystyrene
CaCl <sub>2</sub>	calcium chloride
Ca <sup>2+</sup>	calcium ion
NaCl	sodium chloride
CsCl	Cesium chloride
AlB <sub>2</sub>	aluminum boride
Li-O <sub>2</sub>	lithium-oxygen
Li <sub>2</sub> O <sub>2</sub>	lithium peroxide
O <sub>2</sub>	oxygen
RF	resorcinol-formaldehyde
Na <sub>2</sub> CO <sub>3</sub>	sodium carbonate
C-C	carbon-carbon
N <sub>2</sub>	nitrogen
TiO <sub>2</sub>	titanium dioxide
ZnO	zinc oxide

### Equipment and methods

AUC	analytical ultracentrifugation
UV/Vis	ultraviolet-visible
PXRD	powder X-ray diffraction
DLS	dynamic light scattering
SEM	scanning electron microscopy

AF4	flow field-flow fractionation
IR	infrared spectroscopy
TGA	thermogravimetric analysis
DLVO	Derjaguin-Landau-Verwey-Overbeek theory

### Miscellaneous

T	temperature
nm	nanometer
um	micrometer
3D	three dimension
rpm	rotation per minute
s	sedimentation coefficient
D	diffusion coefficient
3DOM	three dimensional ordered macroporous materials
d <sub>H</sub>	hydrodynamic diameter
V	voltage
fcc	face centered cubic
mM	milimolar
g/ml	gram per milliliter
fs	femtosecond
mAh/g	milliampere hour per gram
w.t.	weight percentage

## 8. References

1. Ralston, G. B., *Introduction to analytical ultracentrifugation*. Beckman Instruments: 1993.
2. Einstein, A., *Investigations on the Theory of the Brownian Movement*. Translation by AD Cowper of papers published 1905–1908. R. Furth, editor. Dover Publications, New York: 1926.
3. Perrin, J., *Atoms*, Constable. London: 1923.
4. Terentjev, E. M.; Weitz, D. A., *The Oxford Handbook of Soft Condensed Matter*. Oxford University Press, USA: 2015.
5. Gast, A. P.; Russel, W. B., Simple ordering in complex fluids. *Physics Today* **1998**, *51*, 24-31.
6. Auer, S.; Frenkel, D., Prediction of absolute crystal-nucleation rate in hard-sphere colloids. *Nature* **2001**, *409* (6823), 1020-1023.
7. Yethiraj, A.; van Blaaderen, A., A colloidal model system with an interaction tunable from hard sphere to soft and dipolar. *Nature* **2003**, *421* (6922), 513-517.
8. Gasser, U.; Weeks, E. R.; Schofield, A.; Pusey, P.; Weitz, D., Real-space imaging of nucleation and growth in colloidal crystallization. *Science* **2001**, *292* (5515), 258-262.
9. Li, F.; Josephson, D. P.; Stein, A., Colloidal assembly: The road from particles to colloidal molecules and crystals. *Angewandte Chemie International Edition* **2011**, *50* (2), 360-388.
10. Gottardo, S.; Sapienza, R.; Garcia, P. D.; Blanco, A.; Wiersma, D. S.; López, C., Resonance-driven random lasing. *Nature Photonics* **2008**, *2* (7), 429-432.
11. Sapienza, R.; Garcia, P.; Bertolotti, J.; Martin, M.; Blanco, A.; Vina, L.; López, C.; Wiersma, D., Observation of resonant behavior in the energy velocity of diffused light. *Physical review letters* **2007**, *99* (23), 233902.
12. Polarz, S.; Smarsly, B., Nanoporous materials. *Journal of nanoscience and nanotechnology* **2002**, *2* (6), 581-612.
13. Stein, A.; Wilson, B. E.; Rudisill, S. G., Design and functionality of colloidal-crystal-templated materials—chemical applications of inverse opals. *Chemical Society Reviews* **2013**.

14. Park, J.; Joo, J.; Kwon, S. G.; Jang, Y.; Hyeon, T., Synthesis of monodisperse spherical nanocrystals. *Angewandte Chemie International Edition* **2007**, *46* (25), 4630-4660.
15. Vayssieres, L., Growth of arrayed nanorods and nanowires of ZnO from aqueous solutions. *Advanced Materials* **2003**, *15* (5), 464-466.
16. Wiley, B. J.; Chen, Y.; McLellan, J. M.; Xiong, Y.; Li, Z.-Y.; Ginger, D.; Xia, Y., Synthesis and optical properties of silver nanobars and nanorice. *Nano letters* **2007**, *7* (4), 1032-1036.
17. Klajn, R.; Pinchuk, A. O.; Schatz, G. C.; Grzybowski, B. A., Synthesis of Heterodimeric Sphere–Prism Nanostructures via Metastable Gold Supraspheres. *Angewandte Chemie International Edition* **2007**, *46* (44), 8363-8367.
18. Lauhon, L. J.; Gudixsen, M. S.; Wang, D.; Lieber, C. M., Epitaxial core–shell and core–multishell nanowire heterostructures. *Nature* **2002**, *420* (6911), 57-61.
19. Gref, R.; Minamitake, Y.; Peracchia, M. T.; Trubetskov, V.; Torchilin, V.; Langer, R., Biodegradable long-circulating polymeric nanospheres. *Science* **1994**, *263* (5153), 1600-1603.
20. Sun, S.; Zeng, H.; Robinson, D. B.; Raoux, S.; Rice, P. M.; Wang, S. X.; Li, G., Monodisperse MFe<sub>2</sub>O<sub>4</sub> (M= Fe, Co, Mn) nanoparticles. *Journal of the American Chemical Society* **2004**, *126* (1), 273-279.
21. Bruchez, M.; Moronne, M.; Gin, P.; Weiss, S.; Alivisatos, A. P., Semiconductor nanocrystals as fluorescent biological labels. *science* **1998**, *281* (5385), 2013-2016.
22. Sun, Y.; Xia, Y., Shape-controlled synthesis of gold and silver nanoparticles. *Science* **2002**, *298* (5601), 2176-2179.
23. Dong, A.; Ye, X.; Chen, J.; Murray, C. B., Two-dimensional binary and ternary nanocrystal superlattices: the case of monolayers and bilayers. *Nano letters* **2011**, *11* (4), 1804-1809.
24. Kagan, C.; Murray, C.; Bawendi, M., Long-range resonance transfer of electronic excitations in close-packed CdSe quantum-dot solids. *Physical Review B* **1996**, *54* (12), 8633.
25. Eldridge, M.; Madden, P.; Frenkel, D., Entropy-driven formation of a superlattice in a hard-sphere binary mixture. *Nature* **1993**, *365* (6441), 35-37.
26. Cottin, X.; Monson, P., Substitutionally ordered solid solutions of hard spheres. *The Journal of chemical physics* **1995**, *102* (8), 3354-3360.

27. TRIZAC, B. E.; MADDEN, M. E.; PA, Stability of the AB crystal for asymmetric binary hard sphere mixtures. *Molecular Physics* **1997**, *90* (4), 675-678.
28. Shevchenko, E. V.; Talapin, D. V.; Murray, C. B.; O'Brien, S., Structural characterization of self-assembled multifunctional binary nanoparticle superlattices. *Journal of the American Chemical Society* **2006**, *128* (11), 3620-3637.
29. Bishop, K. J.; Wilmer, C. E.; Soh, S.; Grzybowski, B. A., Nanoscale forces and their uses in self-assembly. *small* **2009**, *5* (14), 1600-1630.
30. Grzybowski, B. A.; Wilmer, C. E.; Kim, J.; Browne, K. P.; Bishop, K. J., Self-assembly: from crystals to cells. *Soft Matter* **2009**, *5* (6), 1110-1128.
31. Morkved, T.; Lu, M.; Urbas, A.; Ehrichs, E., Local control of microdomain orientation in diblock copolymer thin films with electric fields. *Science* **1996**, *273* (5277), 931.
32. Sahoo, Y.; Cheon, M.; Wang, S.; Luo, H.; Furlani, E.; Prasad, P., Field-directed self-assembly of magnetic nanoparticles. *The Journal of Physical Chemistry B* **2004**, *108* (11), 3380-3383.
33. Karabudak, E.; Brookes, E.; Lesnyak, V.; Gaponik, N.; Eychmüller, A.; Walter, J.; Segets, D.; Peukert, W.; Wohlleben, W.; Demeler, B., Simultaneous Identification of Spectral Properties and Sizes of Multiple Particles in Solution with Subnanometer Resolution. *Angewandte Chemie International Edition* **2016**, *55* (39), 11770-11774.
34. Machtle, W., High-resolution, submicron particle size distribution analysis using gravitational-sweep sedimentation. *Biophysical Journal* **1999**, *76* (2), 1080-1091.
35. Muller, H. G., AUTOMATED-DETERMINATION OF PARTICLE-SIZE DISTRIBUTIONS OF DISPERSIONS BY ANALYTICAL ULTRACENTRIFUGATION. *Colloid and Polymer Science* **1989**, *267* (12), 1113-1116.
36. Colfen, H., Analytical ultracentrifugation of gels. *Colloid and Polymer Science* **1995**, *273* (12), 1101-1137.
37. Page, M. G.; Zemb, T.; Dubois, M.; Coelfen, H., Osmotic pressure and phase boundary determination of multiphase systems by analytical ultracentrifugation. *Chemphyschem* **2008**, *9* (6), 882-890.
38. Graham, T., Liquid diffusion applied to analysis. *Philosophical Transactions of the Royal Society of London* **1861**, *151*, 183-224.

39. Derjaguin, B.; Landau, L., Theory of the stability of strongly charged lyophobic sols and of the adhesion of strongly charged particles in solutions of electrolytes. *Acta physicochim. URSS* **1941**, *14* (6), 633-662.
40. Israelachvili, J. N., Chapter 14 - Electrostatic Forces between Surfaces in Liquids. In *Intermolecular and Surface Forces (Third Edition)*, Academic Press: San Diego, 2011; pp 291-340.
41. Israelachvili, J. N.; McGuiggan, P. M., Forces between surfaces in liquids. *Science* **1988**, *241* (4867), 795-800.
42. Batchelor, G.; Green, J.-T., The hydrodynamic interaction of two small freely-moving spheres in a linear flow field. *Journal of Fluid Mechanics* **1972**, *56* (02), 375-400.
43. Bishop, K. J.; Grzybowski, B. A., "Nanoions": Fundamental Properties and Analytical Applications of Charged Nanoparticles. *ChemPhysChem* **2007**, *8* (15), 2171-2176.
44. Grier, D. G., When like charges attract: interactions and dynamics in charge-stabilized colloidal suspensions. *Journal of Physics: Condensed Matter* **2000**, *12* (8A), A85.
45. Bishop, K. J. M.; Wilmer, C. E.; Soh, S.; Grzybowski, B. A., Nanoscale Forces and Their Uses in Self-Assembly. *Small* **2009**, *5* (14), 1600-1630.
46. Guldbrand, L.; Jönsson, B.; Wennerström, H.; Linse, P., Electrical double layer forces. A Monte Carlo study. *The Journal of chemical physics* **1984**, *80* (5), 2221-2228.
47. Levin, Y., Electrostatic correlations: from plasma to biology. *Reports on progress in physics* **2002**, *65* (11), 1577.
48. Kihira, H.; Ryde, N.; Matijevic, E., Kinetics of heterocoagulation. Part.2-The effect of the discreteness of surface charge. *Journal of the Chemical Society, Faraday Transactions* **1992**, *88* (16), 2379-2386.
49. Tohver, V., *Phase behavior, structure, and properties of colloidal microsphere-nanoparticle mixtures*. 2001.
50. Hiemenz, P. C.; Rajagopalan, R., *Principles of Colloid and Surface Chemistry, revised and expanded*. CRC press: 1997; Vol. 14.
51. Bell, G.; Levine, S.; McCartney, L., Approximate methods of determining the double-layer free energy of interaction between two charged colloidal spheres. *Journal of Colloid and Interface Science* **1970**, *33* (3), 335-359.

52. Pusey, P.; Van Megen, W., Phase behaviour of concentrated suspensions of nearly hard colloidal spheres. *Nature* **1986**, *320* (6060), 340-342.
53. Chen, M.; Cölfen, H.; Polarz, S., The Effect of centrifugal force on the assembly and crystallization of binary colloidal systems: towards structural gradients. *Zeitschrift für Naturforschung B* **2013**, *68* (2), 103-110.
54. Karabudak, E.; Brookes, E.; Lesnyak, V.; Gaponik, N.; Eychmüller, A.; Walter, J.; Segets, D.; Peukert, W.; Wohlleben, W.; Demeler, B.; Cölfen, H., Simultaneous Identification of Spectral Properties and Sizes of Multiple Particles in Solution with Subnanometer Resolution. *Angewandte Chemie International Edition* **2016**, n/a-n/a.
55. Schachman, H. K., *Ultracentrifugation in biochemistry*. Elsevier: 2013.
56. Hongwei, Y.; Lin, Z.; Bo, L.; Qiang, Y., Fabrication of polystyrene porous films with gradient pore structures. *High Power Laser and Particle Beams* **2010**, *12*, 026.
57. Liu, J.; Shire, S. J., Analytical ultracentrifugation in the pharmaceutical industry. *Journal of Pharmaceutical Sciences* **1999**, *88* (12), 1237-1241.
58. Svedberg, T.; Nichols, J. B., Determination of size and distribution of size of particle by centrifugal methods. *Journal of the American Chemical Society* **1923**, *45*, 2910-2917.
59. Ralston, G. B.; Beckman Instruments, I., *Introduction to Analytical Ultracentrifugation*. Beckman: 1993.
60. Batchelor, G., Sedimentation in a dilute dispersion of spheres. *Journal of fluid mechanics* **1972**, *52* (02), 245-268.
61. Buscall, R.; Goodwin, J.; Ottewill, R.; Tadros, T. F., The settling of particles through Newtonian and non-Newtonian media. *Journal of Colloid and Interface Science* **1982**, *85* (1), 78-86.
62. Mittal, V.; Lechner, M. D., Sedimentation studies of single and bi-component polystyrene solutions in analytical ultracentrifugation by comparison of two analysis methods: effect of polymer concentration. *Polym. Bull.* **2011**, *67* (5), 831-841.
63. Rubinov, S. I., *Introduction to Mathematical Biology*. Dover Publ.: 1975.
64. Van Holde, K.; Weischet, W. O., Boundary analysis of sedimentation - velocity experiments with monodisperse and paucidisperse solutes. *Biopolymers* **1978**, *17* (6), 1387-1403.

65. Planken, K. L.; Cölfen, H., Analytical ultracentrifugation of colloids. *Nanoscale* **2010**, *2* (10), 1849-1869.
66. Scott, D. J.; Schuck, P., A brief introduction to the analytical ultracentrifugation of proteins for beginners. *Analytical ultracentrifugation: technique and methods. The Royal Society of Chemistry, Cambridge. doi* **2005**, *10* (9781847552617), 1015-1019.
67. Zabukovec Logar, N.; Kaucic, V., Nanoporous materials: from catalysis and hydrogen storage to wastewater treatment. *Acta chimica slovenica* **2006**, *53* (2), 117-135.
68. Knox, J. H.; Kaur, B.; Millward, G., Structure and performance of porous graphitic carbon in liquid chromatography. *Journal of Chromatography A* **1986**, *352*, 3-25.
69. Reimer, L., *Image Formation in Low-Voltage Scanning Electron Microscopy*. Society of Photo Optical: 1993.
70. Lyman, C. E., *Scanning Electron Microscopy, X-Ray Microanalysis, and Analytical Electron Microscopy: A Laboratory Workbook*. Plenum Press: 1990.
71. von Freymann, G.; Kitaev, V.; Lotsch, B. V.; Ozin, G. A., Bottom-up assembly of photonic crystals. *Chemical Society Reviews* **2013**, *42* (7), 2528-2554.
72. Galisteo-López, J. F.; Ibisate, M.; Sapienza, R.; Froufe-Pérez, L. S.; Blanco, Á.; López, C., Self-assembled photonic structures. *Advanced Materials* **2011**, *23* (1), 30-69.
73. García, P. D.; Sapienza, R.; López, C., Photonic glasses: a step beyond white paint. *Advanced materials* **2010**, *22* (1), 12-19.
74. Garcia, P.; Sapienza, R.; Bertolotti, J.; Martin, M.; Blanco, A.; Altube, A.; Vina, L.; Wiersma, D.; López, C., Resonant light transport through Mie modes in photonic glasses. *Physical Review A* **2008**, *78* (2), 023823.
75. García, P. D.; Sapienza, R.; Blanco, Á.; López, C., Photonic Glass: A Novel Random Material for Light. *Advanced Materials* **2007**, *19* (18), 2597-2602.
76. Xu, S.; Sun, Z., Progress in coagulation rate measurements of colloidal dispersions. *Soft Matter* **2011**, *7* (24), 11298-11308.
77. Salopek, B.; Krasić, D.; Filipović, S., *Measurement and application of zeta-potential*. Rudarsko-geološko-naftni fakultet: 1992.

78. Ostolska, I.; Wiśniewska, M., Application of the zeta potential measurements to explanation of colloidal Cr<sub>2</sub>O<sub>3</sub> stability mechanism in the presence of the ionic polyamino acids. *Colloid and polymer science* **2014**, *292* (10), 2453-2464.
79. Liu, J.; Andya, J. D.; Shire, S. J., A critical review of analytical ultracentrifugation and field flow fractionation methods for measuring protein aggregation. *The AAPS journal* **2006**, *8* (3), E580-E589.
80. Lebowitz, J.; Lewis, M. S.; Schuck, P., Modern analytical ultracentrifugation in protein science: a tutorial review. *Protein Science* **2002**, *11* (9), 2067-2079.
81. Lechner, M. D.; Börger, L., *Analytical ultracentrifugation VII*. Springer Science & Business Media: 2004; Vol. 127.
82. S.E. Harding, A. J. R., *Dynamic Properties of Biomolecular Assemblies*. ROYAL SOCIETY OF CHEMISTRY, 1988.
83. von Freymann, G.; Kitaev, V.; Lotsch, B. V.; Ozin, G. A., Bottom-up assembly of photonic crystals. *Chemical Society Reviews* **2013**.
84. Weitz, D. A., Packing in the spheres. *Science* **2004**, *303* (5660), 968-969.
85. Sperling, T.; Schertel, L.; Ackermann, M.; Aubry, G. J.; Aegerter, C. M.; Maret, G., Can 3D light localization be reached in 'white paint'? *New Journal of Physics* **2016**, *18* (1), 013039.
86. Kitaev, V.; Ozin, G. A., Self-Assembled Surface Patterns of Binary Colloidal Crystals. *Advanced Materials* **2003**, *15* (1), 75-78.
87. Bartlett, P.; Campbell, A. I., Three-dimensional binary superlattices of oppositely charged colloids. *Physical review letters* 2005, *95* (12), 128302.
88. Velikov, K. P.; Christova, C. G.; Dullens, R. P.; van Blaaderen, A., Layer-by-layer growth of binary colloidal crystals. *Science* **2002**, *296* (5565), 106-109.
89. Gu, Z. Z.; Uetsuka, H.; Takahashi, K.; Nakajima, R.; Onishi, H.; Fujishima, A.; Sato, O., Structural color and the lotus effect. *Angewandte Chemie International Edition* **2003**, *42* (8), 894-897.
90. Burkert, K.; Neumann, T.; Wang, J.; Jonas, U.; Knoll, W.; Oettleben, H., Automated preparation method for colloidal crystal arrays of monodisperse and binary colloid mixtures by contact printing with a pintool plotter. *Langmuir* **2007**, *23* (6), 3478-3484.

- 
91. Kovalenko, M. V.; Scheele, M.; Talapin, D. V., Colloidal Nanocrystals with Molecular Metal Chalcogenide Surface Ligands. *Science* **2009**, *324* (5933), 1417-1420.
92. Kiely, C. J.; Fink, J.; Brust, M.; Bethell, D.; Schiffrin, D. J., Spontaneous ordering of bimodal ensembles of nanoscopic gold clusters. *Nature* **1998**, *396* (6710), 444-446.
93. Shevchenko, E. V.; Talapin, D. V.; Kotov, N. A.; O'Brien, S.; Murray, C. B., Structural diversity in binary nanoparticle superlattices. *Nature* **2006**, *439* (7072), 55-59.
94. Both, J. A.; Hong, D. C., Variational approach to hard sphere segregation under gravity. *Physical review letters* **2002**, *88* (12), 124301.
95. Hong, D. C.; Quinn, P. V.; Luding, S., Reverse Brazil nut problem: competition between percolation and condensation. *Physical Review Letters* **2001**, *86* (15), 3423.
96. Shinbrot, T.; Muzzio, F. J., Reverse buoyancy in shaken granular beds. *Physical Review Letters* **1998**, *81* (20), 4365.
97. Breu, A.; Ensner, H.-M.; Kruelle, C. A.; Rehberg, I., Reversing the Brazil-nut effect: competition between percolation and condensation. *Physical review letters* **2003**, *90* (1), 014302.
98. Schröter, M.; Ulrich, S.; Kreft, J.; Swift, J. B.; Swinney, H. L., Mechanisms in the size segregation of a binary granular mixture. *Physical Review E* **2006**, *74* (1), 011307.
99. Williams, J. C., The segregation of particulate materials. A review. *Powder technology* **1976**, *15* (2), 245-251.
100. Rosato, A.; Strandburg, K. J.; Prinz, F.; Swendsen, R. H., Why the Brazil nuts are on top: Size segregation of particulate matter by shaking. *Physical Review Letters* **1987**, *58* (10), 1038.
101. Esztermann, A.; Lowen, H., Colloidal Brazil-nut effect in sediments of binary charged suspensions. *Europhysics Letters* **2004**, *68* (1), 120-126.
102. Lechner, M. D.; Cölfen, H.; Mittal, V.; Völkel, A.; Wohlleben, W., Sedimentation measurements with the analytical ultracentrifuge with absorption optics: influence of Mie scattering and absorption of the particles. *Colloid and Polymer Science* **2011**, *289* (10), 1145-1155.
103. Schuck, P., Size-distribution analysis of macromolecules by sedimentation velocity ultracentrifugation and Lamm equation modeling. *Biophys. J.* **2000**, *78* (3), 1606-1619.

104. Piazza, R.; Buzzaccaro, S.; Secchi, E.; Parola, A., On the general concept of buoyancy in sedimentation and ultracentrifugation. *Phys. Biol.* **2013**, *10* (4), 16.
105. Sentjabrskaja, T.; Babaliari, E.; Hendricks, J.; Laurati, M.; Petekidis, G.; Egelhaaf, S. U., Yielding of binary colloidal glasses. *Soft Matter* **2013**, *9* (17), 4524-4533.
106. Voigtmann, T., Multiple glasses in asymmetric binary hard spheres. *Epl* **2011**, *96* (3), 6.
107. Chen, M.; Cölfen, H.; Polarz, S., The Effect of Centrifugal Force on the Assembly and Crystallization of Binary Colloidal Systems: Towards Structural Gradients. *Z.Naturforsch.(B)* **2013**, *68* (2), 103-110.
108. Chen, M.; Cölfen, H.; Polarz, S., Centrifugal Field-Induced Colloidal Assembly: From Chaos to Order. *ACS nano* **2015**, *9* (7), 6944-6950.
109. de las Heras, D.; Schmidt, M., The phase stacking diagram of colloidal mixtures under gravity. *Soft Matter* **2013**, *9* (36), 8636-8641.
110. Hansen, J. P.; I.R., M., *Theory of simple liquids*. 3rd edition ed.; Elsevier: Amsterdam, 2006.
111. Maji, T. K.; Matsuda, R.; Kitagawa, S., A flexible interpenetrating coordination framework with a bimodal porous functionality. *Nat. Mater.* **2007**, *6* (2), 142-148.
112. Antonietti, M.; Berton, B.; Göltner, C.; Hentze, H. P., Synthesis of mesoporous silica with large pores and bimodal pore size distribution by templating of polymer lattices. *Adv. Mater.* **1998**, *10* (2), 154-159.
113. Lu, A. H.; Schmidt, W.; Spliethoff, B.; Schüth, F., Synthesis of ordered mesoporous carbon with bimodal pore system and high pore volume. *Adv. Mater.* **2003**, *15* (19), 1602-1606.
114. Rabin, B. H.; Shiota, I., FUNCTIONALLY GRADIENT MATERIALS. *MRS Bull.* **1995**, *20* (1), 14-15.
115. Claussen, K. U.; Scheibel, T.; Schmidt, H. W.; Giesa, R., Polymer gradient materials: Can nature teach us new tricks? *Macromolecular Materials and Engineering* **2012**, *297* (10), 938-957.
116. Seidi, A.; Ramalingam, M.; Elloumi-Hannachi, I.; Ostrovidov, S.; Khademhosseini, A., Gradient biomaterials for soft-to-hard interface tissue engineering. *Acta biomaterialia* **2011**, *7* (4), 1441-1451.

117. Waite, J. H., The formation of mussel byssus: anatomy of a natural manufacturing process. In *Structure, cellular synthesis and assembly of biopolymers*, Springer: 1992; pp 27-54.
118. Brandon, N. P.; Brett, D. J., Engineering porous materials for fuel cell applications. *Philos. Trans. R. Soc. A-Math. Phys. Eng. Sci.* **2006**, *364* (1838), 147-159.
119. Schachtschneider, A.; Wessig, M.; Spitzbarth, M.; Donner, A.; Fischer, C.; Drescher, M.; Polarz, S., Directional Materials Nanoporous Organosilica Monoliths with Multiple Gradients Prepared Using Click Chemistry. *Angew. Chem.-Int. Edit.* **2015**, *54* (36), 10465-10469.
120. Luo, R.; Wu, J.; Dinh, N. D.; Chen, C. H., Gradient Porous Elastic Hydrogels with Shape-Memory Property and Anisotropic Responses for Programmable Locomotion. *Adv. Funct. Mater.* **2015**, *25* (47), 7272-7279.
121. Lee, K. T.; Lytle, J. C.; Ergang, N. S.; Oh, S. M.; Stein, A., Synthesis and Rate Performance of Monolithic Macroporous Carbon Electrodes for Lithium-Ion Secondary Batteries. *Advanced Functional Materials* **2005**, *15* (4), 547-556.
122. Moreno-Castilla, C.; Maldonado-Hodar, F. J., Carbon aerogels for catalysis applications: An overview. *Carbon* **2005**, *43* (3), 455-465.
123. Su, B.-L.; Sanchez, C.; Yang, X.-Y., *Hierarchically structured porous materials: from nanoscience to catalysis, separation, optics, energy, and life science*. John Wiley & Sons: 2012.
124. Chen, M.; Hagedorn, K.; Cölfen, H.; Polarz, S., Functional Gradient Inverse Opal Carbon Monoliths with Directional and Multinary Porosity. *Advanced Materials* 2017, *29* (2), DOI: 10.1002/adma.201603356.
125. Pimenta, M. A.; Dresselhaus, G.; Dresselhaus, M. S.; Cancado, L. G.; Jorio, A.; Saito, R., Studying disorder in graphite-based systems by Raman spectroscopy. *Phys. Chem. Chem. Phys.* **2007**, *9* (11), 1276-1290.
126. SekharáRout, C., Changes in the electronic structure and properties of graphene induced by molecular charge-transfer. *Chem. Comm.* **2008**, (41), 5155-5157.
127. Peng, Z.; Freunberger, S. A.; Chen, Y.; Bruce, P. G., A Reversible and Higher-Rate Li-O<sub>2</sub> Battery. *Science* **2012**, *337* (6094), 563-566.
128. Jian, Z.; Liu, P.; Li, F.; He, P.; Guo, X.; Chen, M.; Zhou, H., Core-Shell-Structured CNT@RuO<sub>2</sub> Composite as a High-Performance Cathode Catalyst for Rechargeable Li-O<sub>2</sub> Batteries. *Angewandte Chemie International Edition* **2014**, *53* (2), 442-446.

129. Li, X.; Faghri, A., Optimization of the Cathode Structure of Lithium-Air Batteries Based on a Two-Dimensional, Transient, Non-Isothermal Model. *Journal of The Electrochemical Society* **2012**, *159* (10), A1747-A1754.
130. Olivares-Marín, M.; Palomino, P.; Amarilla, J. M.; Enciso, E.; Tonti, D., Effects of architecture on the electrochemistry of binder-free inverse opal carbons as Li-air cathodes in an ionic liquid-based electrolyte. *Journal of Materials Chemistry A* **2013**, *1* (45), 14270-14279.
131. Ding, N.; Chien, S. W.; Hor, T. A.; Lum, R.; Zong, Y.; Liu, Z., Influence of carbon pore size on the discharge capacity of Li-O<sub>2</sub> batteries. *Journal of Materials Chemistry A* **2014**, *2* (31), 12433-12441.
132. Sun, B.; Chen, S. Q.; Liu, H.; Wang, G. X., Mesoporous Carbon Nanocube Architecture for High-Performance Lithium-Oxygen Batteries. *Adv. Funct. Mater.* **2015**, *25* (28), 4436-4444.
133. Nielsen, M. H.; Aloni, S.; De Yoreo, J. J., In situ TEM imaging of CaCO<sub>3</sub> nucleation reveals coexistence of direct and indirect pathways. *Science* **2014**, *345* (6201), 1158-1162.
134. Ma, J.; Sinha, S., Thermoelectric properties of highly doped n-type polysilicon inverse opals. *Journal of Applied Physics* **2012**, *112* (7), 073719-073719-9.
135. Tarkhanyan, R. H.; Niarchos, D. G., Reduction of thermal conductivity in porous “gray” materials. *APL Materials* **2014**, *2* (7), -.
136. Chung-li, Y.; goodwin, J. W.; Ottewill, R. H., Studies on the preparation and characterisation of monodisperse polystyrene latices. In *Kolloidchemie heute II*, Kohlschütter, H.; Müller, F. H.; Weiss, A., Eds. Steinkopff: 1976; Vol. 60, pp 163-175.
137. Reese, C. E.; Guerrero, C. D.; Weissman, J. M.; Lee, K.; Asher, S. A., Synthesis of highly charged, monodisperse polystyrene colloidal particles for the fabrication of photonic crystals. *J Colloid Interf Sci* **2000**, *232* (1), 76-80.
138. Chung-Li, Y.; Ottewill, R., Studies on the preparation and characterisation of monodisperse polystyrene latices. In *Kolloidchemie heute II*, Springer: 1976; pp 163-175.
139. Aschauer, U.; Burgos-Montes, O.; Moreno, R.; Bowen, P., Hamaker 2: a toolkit for the calculation of particle interactions and suspension stability and its application to mullite synthesis by colloidal methods. *Journal of Dispersion Science and Technology* **2011**, *32* (4), 470-479.

140. Strauss, H. M.; Karabudak, E.; Bhattacharyya, S.; Kretzschmar, A.; Wohlleben, W.; Colfen, H., Performance of a fast fiber based UV/Vis multiwavelength detector for the analytical ultracentrifuge. *Colloid Polym. Sci.* **2008**, *286* (2), 121-128.
141. Cölfen, H.; Laue, T. M.; Wohlleben, W.; Schilling, K.; Karabudak, E.; Langhorst, B. W.; Brookes, E.; Dubbs, B.; Zollars, D.; Rocco, M., The open AUC project. *European Biophysics Journal* **2010**, *39* (3), 347-359.